Spring 2017

Petrography and Geochemistry of Oligocene Rhyolitic Volcanic Rocks, Western Mogollon-Datil Volcanic Field, New Mexico

Emily Elizabeth Salings

PETROGRAPHY AND GEOCHEMISTRY OF OLIGOCENE RHYOLITIC VOLCANIC ROCKS, WESTERN MOGOLLON-DATIL VOLCANIC FIELD, NEW MEXICO

A Masters Thesis

Presented to

The Graduate College of

Missouri State University

In Partial Fulfillment

Of the Requirements for the Degree

Master of Natural and Applied Sciences

By

Emily Elizabeth Salings

May 2017

PETROGRAPHY AND GEOCHEMISTRY OF OLIGOCENE RHYOLITIC VOLCANIC ROCKS, WESTERN MOGOLLON-DATIL VOLCANIC FIELD, NEW MEXICO

Geography, Geology, and Planning

Missouri State University, May 2017

Master of Natural and Applied Sciences

Emily Salings

ABSTRACT

The Mogollon-Datil volcanic field (MDVF), located in southern New Mexico, is the remnant of extreme and punctuated volcanism over ~12 m.y. of activity. The Bursum caldera is the youngest of three nested calderas in the Mogollon Mountains in the western MDVF. Here I present data from a high-silica, large volume tuff associated with the Bursum caldera, the Bloodgood Canyon Tuff (BCT). Extensive mapping by previous workers have provided a limited whole rock geochemical dataset and descriptions of the unit, but a detailed study had not been conducted. I present new whole-rock major- and trace-element analyses, Sr, Nd, and Pb isotope ratios, mineral chemistry, and petrographic textures to suggest an evolution model for the BCT. I suggest a model of assimilation and fractional crystallization of a dacite composition magma followed by the remobilization of a crystal mush by the upwelling of mafic magma at the peak of ignimbrite flare-up in southern New Mexico. Thermal disequilibrium induced by an intrusion of high-temperature mafic magma initiated the eruption of the BCT, and remobilization of this mush mixed with rhyolitic composition magma lenses within the mush that interacted locally with the amphibolitic-composition crust. Further destabilization of the magma chamber initiated a trapdoor style collapse of the Bursum caldera and erupted most of the remaining eruptible magma.

KEYWORDS: ignimbrite, cumulate, continental arc, arc magmatism, magma evolution

This abstract is approved as to form and content

_____

Gary Michelfelder, PhD
Chairperson, Advisory Committee
Missouri State University

PETROGRAPHY AND GEOCHEMISTRY OF OLIGOCENE RHYOLITIC VOLCANIC ROCKS, WESTERN MOGOLLON-DATIL VOLCANIC FIELD, NEW MEXICO

By

Emily Elizabeth Salings

A Masters Thesis
Submitted to the Graduate College
Of Missouri State University
In Partial Fulfillment of the Requirements
For the Degree of Master of Natural and Applied Science

May 2017

Approved:

_____
Gary Michelfelder, PhD

_____
Richard Biagioni, PhD

_____
Melida Gutierrez, PhD

_____
Julie Masterson, PhD: Dean, Graduate College

ACKNOWLEDGEMENTS

I would like to thank Frank Ramos (New Mexico State University) and Kenny Horkley (University of Iowa) for use of their respective laboratories and Washington State University for major- and trace-element analyses, and John Hogan and Owen Neil for discussions on crystal size distributions. Dr. Ben Ellis and an anonymous reviewer are gratefully acknowledged for their reviews on Manuscript 1. I also thank Missouri State University graduate students Shannon Rentz and Max Hoffman and undergraduates Eric Sikes, Brandie Oehring, Ashley Gerik, and Chris Lewis for their assistance in the field and in the lab. Most importantly, I would like to thank my advisor, Gary Michelfelder, for many discussions on magmatism and geochemistry and my committee members for their input and time. Funding for this project was provided by Missouri State University and the Geological Society of America.

TABLE OF CONTENTS

LIST OF TABLES

Manuscript 1

Manuscript 2

LIST OF FIGURES

OVERVIEW

Introduction

Identifying the processes involved in ancient volcanic systems and understanding the mechanisms that allow large amounts of magma to accumulate in the crust is paramount in understanding modern continental volcanic arcs with ignimbrite-forming eruptions (De Silva et al., 2006; Kern et al., 2016). Eruption of ignimbrites requires accumulation of eruptible magma at a rate that is fast enough to outpace crystallization (Lipman, 2007). Whether the eruptible magma comes from short-lived accumulation that empty the chamber or from portions of mobilized mush bodies is still debated (Glazner et al., 2004; De Silva et al., 2006; Lipman, 2007). There is evidence for immobile crystal mushes that are unable to erupt due to their high crystallinity creating a rigid crystal skeleton, but interstitial liquid can form lenses of rhyolitic, crystal-poor magma that can be erupted if the crystal mush is compacted or the crystals settle (Bachmann and Bergantz, 2008). Remobilization of this mush can occur when subjected to heat from intruding magma melting the crystal skeleton and allowing convection to occur (Bachmann and Bergantz, 2008; Gelman et al., 2014). Mushes can also extract multiple batches of magma driven by tectonic processes such as rifting, creating isolated patches of eruptible magma that do not mix and are triggered by depressurization instead of new magma input (Bégué et al., 2014). This variety of behaviors that magma chambers can exhibit present a problem for unraveling the history of volcanic systems, because there is no one-size-fits-all model. Minerals hold the key to piecing together individual magma histories, through diffusion modeling, residence times, geochemistry, petrography, and

other methods to track the evolution of individual magma batches (Ginibre et al., 2007; Cooper, 2017). When there is no pluton to relate to, testing these ideas can become difficult (Bachmann and Bergantz, 2008).

This study aims to explore the relationship between crystal mushes and large-volume volcanism by studying the evolution of a large-volume ignimbrite called the Bloodgood Canyon Tuff (BCT) from the Mogollon-Datil volcanic field (MDVF) in southwestern New Mexico. There are three questions important to understanding the MDVF by focusing on magma chamber evolution during the emplacement of the BCT. First, are the BCT, and two other ignimbrites believed to be associated with the BCT: the Apache Spring Tuff and the Fanney Rhyolite, petrologically related to each other (did they come from the same source)? Second, what magmatic processes were operating in the plumbing system prior to eruption of the BCT? Third, how do these units reflect the ignimbrite flare up within the MDVF?

This study will test the hypothesis that all three of the units were erupted from the Bursum caldera and sourced from a deeper regional magma reservoir. Mantle magma from the ignimbrite flare-up assimilated with the chamber and underwent mixing and assimilation and fractional crystallization. These units represent the peak of the ignimbrite flare-up as it may have remobilized this crystal-mush plutonic body and added heat to the system needed for melting and crystallization processes to occur.

Here I present two journal article manuscripts on the history and evolution of the Bloodgood Canyon Tuff and its relationship to other ignimbrites in the area. The first article, *Magma Evolution in the Bursum Ignimbrite Complex, western Mogollon-Datil Volcanic Field, New Mexico: Evidence for Zoning of a Rhyolite Magma by*

Remobilization of a Crystal Mush, focuses on introducing the BCT with a detailed description of the stratigraphy, geochemistry, and petrologic modeling to determine what processes created the BCT. Two other units believed to be sourced from the same caldera are also described and compared with the BCT. In this article I conclude that the BCT was formed from assimilation of magma from the Davis Canyon Tuff with an amphibolite-composition wallrock and the remobilization of a large crystal mush made up of alkali feldspar and quartz. This article lays the foundation necessary to understand the more detailed evaluation of the BCT in the second article.

The second article, *Evolution of the Bloodgood Canyon Tuff, western Mogollon-Datil volcanic field, New Mexico: Evidence from mineral chemistry and CSD analysis*, uses mineral chemistry and petrography to develop a more detailed evolution history for the BCT. Mineral chemistry is essential for an accurate and detailed evolution history because minerals can record changes in the magma chamber over time (Ginibre et al., 2007), whereas whole-rock data only records the status of the magma chamber at the time of eruption and lithic fragments or xenocrysts can skew the data. This article adjusts the model for the evolution of the BCT: an accumulation of melt that crystallizes quartz and sanidine is fed by a deeper, lower-crust cumulate of pyroxene, plagioclase, and hornblende. Resorption textures in quartz and alkali feldspar reveal that immediately prior to eruption a thermal disequilibrium event began Ostwald ripening and eruption occurred before the magma chamber could re-equilibrate. Alteration and pressure data for hornblendes found in the BCT reveals that they are actually xenocrystic in nature, supporting the petrologic model developed in the first article that the Davis Canyon Tuff magma assimilated with a wallrock containing amphibole.

Background Geology

The Mogollon-Datil volcanic field (MDVF), located in southern New Mexico (Fig. 1), is the remnant of extreme and punctuated volcanism over ~12 m.y. of activity with a total active period between ~45 and 24 Ma. The MDVF is a manifestation of the volcanic arc situated 500 km from the trench of the Farallon plate and North American plate (Davis and Hawkesworth, 1993; 1994). At least 28 caldera-forming eruptions produced large, regional ash-flow units from 36-24 Ma with smaller eruptions occurring before and after (Elston, 1984; McIntosh et al., 1992; McMillan et al., 2000), covering an area of ~40,000 km^2 and erupted over 12,000 km^3 of high-K, calc-alkaline, basalt through rhyolite, large-volume ignimbrites and small-volume lava flows and domes (Fig. 1; Elston et al., 1970; Davis and Hawkesworth, 1994). Many of these centers such as Bursum, Socorro, and Mt. Withinton are nested and multicyclic, as they have been the site of repeated eruptions, with the most recent being responsible for the current surface expression and structure (Chapin et al., 2004).

The Bursum Ignimbrite Complex is a series of ignimbrites erupted from a group of nested calderas in the western Mogollon-Datil volcanic field (MDVF). The ignimbrites range from calc-alkaline dacites to high-silica rhyolites. The oldest ignimbrite in the Bursum Ignimbrite Complex is the Cooney Formation (34-32 Ma; McIntosh et al., 1990), a series of tuffs sourced from the Mogollon caldera with interbedded volcaniclastic sediments (Rentz et al., 2016). Andesitic intrusions can also be found in the Cooney Formation. The Shelley Peak and Davis Canyon tuffs (~29.0 Ma; McIntosh et al., 1990), sourced from the Gila Cliff Dwellings caldera, are both found stratigraphically below the Bloodgood Canyon Tuff, but are chemically and petrographically distinct. The Shelley

Peak Tuff is slightly older than the Davis Canyon Tuff but is distinct because of the presence of clinopyroxene (Ratté 1981).

The Bloodgood Canyon Tuff (BCT; 28 Ma; McIntosh et al., 1990) is sourced from the largest and youngest of the nested calderas, the Bursum caldera. The largest volume ignimbrite in the area by far (~1300 km^3), the BCT is a high-silica rhyolite with compositional zoning. The base of the BCT is characterized by the enrichment of lithics and pumice fragments and lack of crystals. The middle of the BCT is characterized by large pumice veins and a high crystallinity. The top of the BCT is also crystal-rich, but is depleted in pumice fragments compared to the rest of the section. This study selected three representative samples from the stratigraphic section to analyze: 180-SP-2 as the base of the section, 12RE5b as the middle of the section, and 12RE5a as the top of the section.

The Apache Spring Tuff (27.9 Ma; McIntosh et al., 1990) is also thought to be sourced from the Bursum caldera (Ratté et al., 1984), but whole-rock geochemistry suggests it may not be related to the BCT. The Apache Spring Tuff is an intracaldera fill of the Bursum caldera and is mostly exposed as a breccia on the edges of the caldera. The final unit of the Bursum Ignimbrite Complex is the Fanney Rhyolite, a series of intrusions, lava flows, and small-volume tuffs that makes up the resurgent dome of the Bursum caldera (Ratté et al., 1984). The Fanney Rhyolite is geochemically very distinct from the BCT, but mineral phases and location suggest the two units are sourced from the same caldera.

There are two other ignimbrites in the region that can be mistaken for the BCT due to their similar crystallinity, chemical composition, and mineral phases: the tuff of

Triangle C Ranch and the Fall Canyon Tuff (Ratté, 1981; Ratté et al., 1984; McIntosh et al., 1990; McIntosh et al., 1992; Ratté et al., 1994). The Fall Canyon Tuff (29.4 Ma; Ratté, 1981; McIntosh et al., 1990), found on the margin of the Bursum caldera, is petrographically similar to the BCT, but is interlaid with sandstone and contains more sodic plagioclase and clinopyroxene than the BCT (Ratté, 1981). The tuff of Triangle C Ranch (28.0 Ma; McIntosh et al., 1992) is a high-silica tuff believed to be erupted from the Bursum caldera, but is only mapped north of the Bursum caldera (Ratté et al., 1994). Based on paleomagnetic data, the tuff of Triangle C Ranch erupted at least 5000 years after the BCT (McIntosh et al., 1992). It is petrographically indistinguishable from the BCT, but locally separated from the BCT by a volcaniclastic sandstone (McIntosh et al., 1990; Ratté et al., 1994).

Methods

Selective sampling and stratigraphic measurements of the BCT in the field were done to ensure an accurate portrayal of the stratigraphic variation in the BCT and volume estimates. Unaltered samples were collected from all three units to ensure accurate geochemical analyses. Major- and trace-elements were measured on five BCT samples, two Fanney Rhyolite samples, and one AST sample using X-Ray Fluorescence (XRF) and Inductively-Coupled Plasma Mass Spectrometry (ICP-MS) at Washington State University using the methods of Johnson et al. (1999) and Jarvis (1988), respectively. Three BCT samples were selected to measure Sr, Nd, and Pb radiogenic isotope ratios based on stratigraphic position. Analysis of Sr, Nd, and Pb was performed using a ThermoFinnegan Neptune MC-ICP-MS at New Mexico State University. Approximately

250 mg of whole rock powder used in major- and trace analyses was dissolved in HNO_3, HF, HCl, and HBr and separated by column chemistry, following procedures outlined in Ramos (1992). Measured $^{87}Sr/^{86}Sr$ and $^{143}Nd/^{144}Nd$ ratios were normalized to $^{86}Sr/^{88}Sr=0.1194$ and $^{146}Nd/^{144}Nd=0.7219$, respectively (Újvári et al., 2012). Pb samples were analyzed using nine Faraday collectors and an ion counter by MC-ICP-MS and were compared to the standard NBS 981 ($^{208}Pb/^{204}Pb \approx 36.662 \pm 0.002$, $^{207}Pb/^{204}Pb \approx 15.462 \pm 0.001$, $^{206}Pb/^{204}Pb \approx 16.928 \pm 0.001$) to monitor precision of the analyses. Analyses were within analytical error of known standard values and no corrections were made.

Electron microprobe (EMPA) data for K-feldspar and hornblende grains from three different samples of the BCT and plagioclase grains for one sample of the Cooney Formation were obtained using a JEOL JXA-8230 at the University of Iowa. Phenocrysts and groundmass phases were analyzed in carbon coated standard (30 μm) polished thin sections. Back-Scatter Electron (BSE) images were acquired using a beam set at 15 kV and 20 nA. Spot analyses (5 μm) of ~25 feldspar grains per BCT sample and line transects of 8 K-feldspars in the BCT were collected and 12 albite grains in the Cooney Formation were analyzed; Si, Al, Na, K, Ca, Fe, Ti, Pb, Ba, and Sr were analyzed and normalized to the Astimex Orthoclase standard for Feldspar grains. Cores and/or rims were analyzed for most Feldspars, but grains with perthite textures were analyzed for composition differences between perthite sections with either spot analyses or line transects. Spot analyses (5 μm) of 3-6 hornblende grains per sample were analyzed for Si, Al, Mg, K, Na, Ca, K, Cr, Mn, and Ti and normalized to the UI #1 K-Hornblende and UI #1 A-Hornblende standards. Major elements were run for 15 seconds and trace elements

were run for 30 seconds, and detection limits were ~50 ppm. Energy-Dispersive X-Ray Spectroscopy (EDS) maps of Si, Al, K, Na, Ca, Fe, Mg, Ti, Ba, Cr, Dy, F, Mn, Ni, P, Pb, S, Th, V, Y, Zr, and Cl were collected for whole thin sections of each sample.

Crystal size distributions were determined using Si EDS maps for all three BCT samples, K EDS maps for two samples, and a Na EDS map for one BCT sample analyzed by EMPA. Si EDS maps represented quartz and K or Na maps represented alkali feldspars. A Na EDS map was used for sample 12RE5b CSD analyses because the high K content in welded pumices in the sample made it difficult to digitally separate pumice from phenocrysts. ImageJ v6.0 was used to convert EDS maps into binary images and to outline phenocrysts and remove quartz and sanidine grains embedded in the thin section glass. Resolution issues with grains <0.25 μm made it difficult to analyze, so these grains were excluded from final measurements, and hence CSD results are unable to measure syn-ascent crystallization (Witter et al., 2016). Particles were analyzed in ImageJ v6.0, exported into a CSD file using the CSDCorrections plugin, and run through the CSDCorrections v1.53 program (Higgins, 2000). The CSDCorrections program was used to account for the intersection probability effect and made partial corrections for the cut section effect when using 2D surfaces (Higgins, 2000). The fabric for all CSD calculations was assumed to be massive due to lack of flow banding or foliation, and vesicles were 0% due to the welded nature of the samples. The "Roundness of grains" factor was set to 0.2 (where 1=ellipsoid and 0=block) based on visual inspection for both quartz and alkali feldspar in all samples due to the high population of euhedral grains that are partially resorbed. Size bins that had correction factors >1 were thrown out, usually at the ≤0.158 mm size bin, and bins with less than 5 grains were not included in the final

CSD curves. CSDSlice (Morgan and Jerram, 2006) was used to obtain accurate 3D dimensions of crystal shapes in each sample for alkali feldspars and quartz to input into the CSDCorrections program. Alkali feldspars were tabular in shape (samples 180-SP-2 1:1.25:1.6; 12RE5b 1:1:1.3; 12RE5a 1:1:2.6), while quartz represented rectangular prisms (samples 180-SP-2 1:1:1.5; 12RE5b 1:1.15:1.3; 12RE5a 1:1.5:2.7). All quartz and alkali feldspar crystals were analyzed along the Ellipse Major axis.

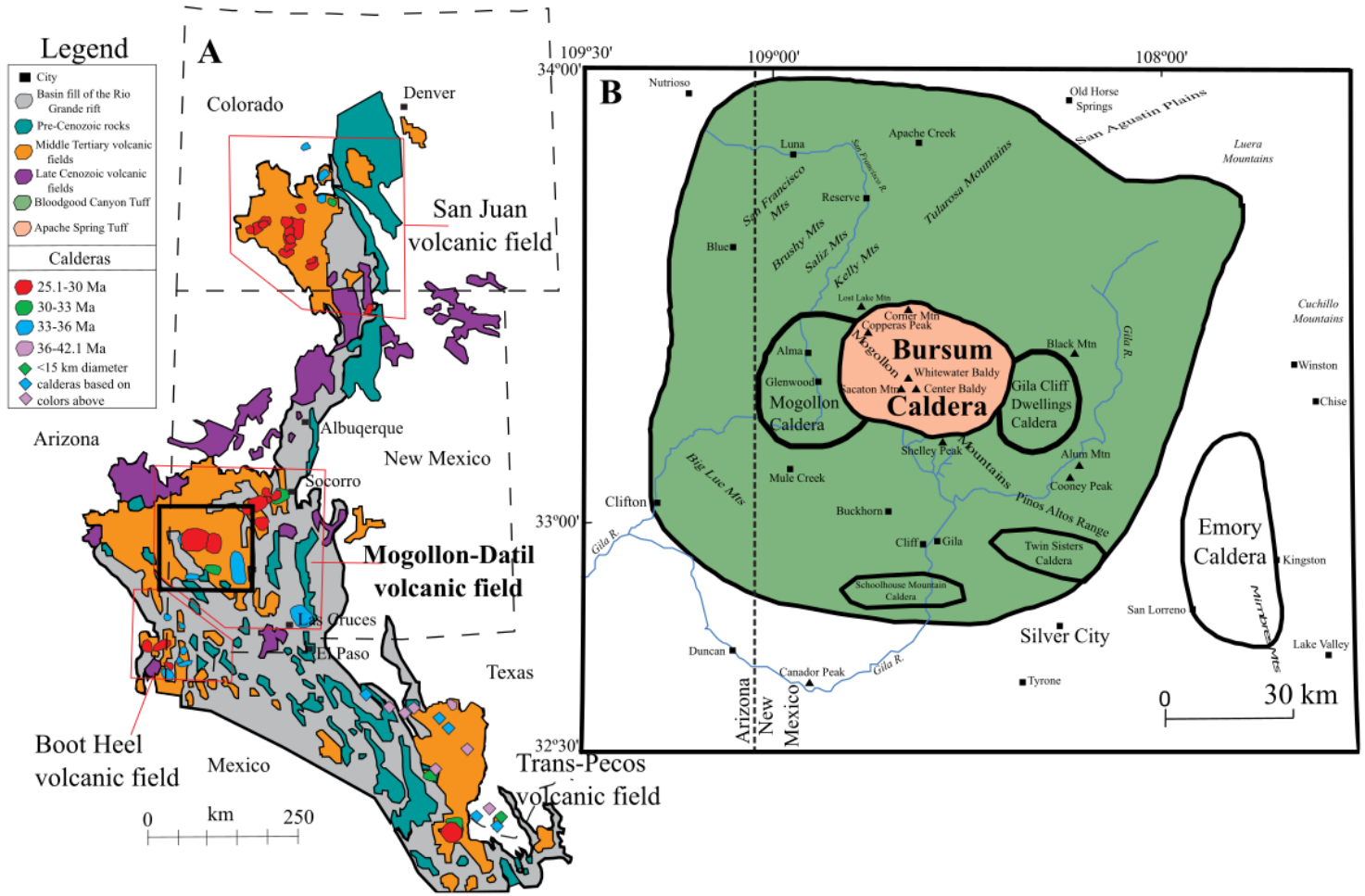

Figure 1. Regional map of (A) the Mogollon-Datil volcanic field and Rio Grande rift volcanic area and (B) the Bursum caldera complex with extent of the Bloodgood Canyon Tuff, modified from Ratté et al. (1984).

MAGMA EVOLUTION IN THE BURSUM IGNIMBRITE COMPLEX, WESTERN MOGOLLON-DATIL VOLCANIC FIELD, NEW MEXICO: EVIDENCE FOR ZONING OF A RHYOLITE MAGMA BY REMOBILIZATION OF A CRYSTAL MUSH

1. Introduction

Identifying the processes involved in ancient volcanic systems and understanding the mechanisms that allow large amounts of magma to accumulate in the crust is paramount in understanding modern continental volcanic arcs with ignimbrite-forming eruptions (De Silva et al., 2006; Kern et al., 2016). Eruption of ignimbrites requires accumulation of eruptible magma at a rate that is fast enough to outpace crystallization (Lipman, 2007). Whether the eruptible magma comes from short-lived accumulation that empty the chamber or from portions of mobilized mush bodies is still debated (Glazner et al., 2004; De Silva et al., 2006; Lipman, 2007). There is evidence for immobile crystal mushes that are unable to erupt due to their high crystallinity creating a rigid crystal skeleton, but interstitial liquid can form lenses of rhyolitic, crystal-poor magma that can be erupted if the crystal mush is compacted or the crystals settle (Bachmann and Bergantz, 2004; Bachmann and Bergantz, 2008). Remobilization of this mush can occur when subjected to heat from intruding magma melting the crystal skeleton and allowing convection to occur (Bachmann and Bergantz, 2008; Gelman et al., 2014). When there is no pluton to relate to, testing these ideas can become difficult.

The Mogollon-Datil volcanic field (MDVF), located in southern New Mexico (Fig. 1), is the remnant of extreme and punctuated volcanism over ~12 m.y. of activity with a total active period between ~45 and 24 Ma. The MDVF is a manifestation of the volcanic arc situated 500 km from the trench of the Farallon plate and North American

plate (Davis and Hawkesworth, 1993; 1994). At least 28 caldera-forming eruptions produced large, regional ash-flow tuff units from 36-24 Ma with smaller eruptions occurring before and after (Elston, 1984; McIntosh et al., 1992; McMillan et al., 2000), covering an area of ~40,000 km^2 and erupted over 12,000 km^3 of high-K, calc-alkaline, basalt through rhyolite, large-volume ignimbrites and small-volume lava flows and domes (Fig. 1; Elston et al., 1970; Davis and Hawkesworth, 1994). Many of these centers such as Bursum, Socorro, and Mt. Withinton are nested and multicyclic, as they have been the site of repeated eruptions, with the most recent eruption being responsible for the current appearance and structure (Chapin et al., 2004).

Subduction related magmatism has persisted on the western margin of North America since the Cretaceous (Chapin et al., 2004; Seagar, 2004). An influx of mantle derived melts has therefore permeated the crust since that time. During the Paleocene through the early Eocene (64-48 Ma) a flat slab was established in southern New Mexico producing a period of limited magmatic activity (McMillan, 2004). This mechanism produced tectonic erosion, hydration and mechanical instability of the upper crust and likely triggered delamination and shortening prior to extension of the Rio Grande Rift and Basin and Range (McMillan, 2004; Mack, 2004; Seagar, 2004). In this time shortening thickened the crust and likely elevated the geotherm in southwest New Mexico leading to a thermally primed crust. Volcanism in the MDVF began at ~45 Ma, when the flat slab subduction of the Farallon plate "rolled back" underneath the North American plate, allowing an influx of mantle material to up well into the mantle wedge (McMillan et al., 2000). The volcanic and intrusive rocks emplaced during this time were intermediate to mafic composition volcanic rocks of the Rubio Peak Formation

(McMillan et al., 2000; Chapin et al., 2004). These volcanic rocks represent a fundamentally different style of magmatism than material erupted later during the Oligocene (Davis and Hawkesworth, 1994; McMillan et al., 2000; McMillan, 2004). Convecting mantle magma produced by flux melting of the subducted slab ponded at the base of the crust and provided heat to the overlying crust, allowing melting of the crust, driving magmatic processes such as assimilation and fractional crystallization and mixing, and the development of the ignimbrite flare-up between 36-24 Ma (DePaolo, 1981a; Chapin et al., 2004; Bachmann and Bergantz, 2008).

The influx of magma from slab roll back coincided with the abrupt initiation of large-volume ignimbrite eruptions in the southern MDVF at 36 Ma and in the northern MDVF at ~32 Ma. The transition was so abrupt the sub-MDVF crust in the south must have be subject to an increased flux of heat leading to regional crustal melting (Chapin et al., 2004, McMillan, 2004; Michelfelder et al., 2013; Zimmerer and McIntosh, 2013). Two other ignimbrite flare-ups initiated from the roll back: the Sierra Madre in Texas and Mexico and the Rocky Mountain volcanic field in Colorado suggesting this melting was larger scale than just southern New Mexico (Chapin et al., 2004; Lipman and Bachmann, 2015). In the MDVF, 9000 km^3 of rhyolite ignimbrite was erupted, with the largest amount of magma erupted during the peak of the ignimbrite flare-up from 28.9-27.4 Ma (McIntosh et al., 1992; Chapin et al., 2004). During the peak, >6000 km^3 of rhyolite magma erupted as part of eleven regional ignimbrites (Chapin et al., 2004). During the ignimbrite flare-up, extension from the Rio Grande rift, Basin and Range, and Transition Zone was beginning, and this extension allowed for faster dike propagation and less

hybridization, allowing for bimodal volcanism and large laccoliths at shallow crustal depths (Chapin et al., 2004; Michelfelder et al., 2012).

This paper focuses on a single ignimbrite erupted from the Mogollon caldera cluster during the peak of the ignimbrite flare-up and the most recent eruptions of the nested caldera system, the Bloodgood Canyon Tuff (BCT; 28.0 Ma), and include two units believed to be associated with the BCT, the Apache Spring Tuff (AST; 27.9 Ma) and the Fanney Rhyolite (26.4-24.4 Ma; Bikerman et al., 1992).

I present stratigraphic and whole-rock major and trace element data and a first-order petrologic model of the BCT and other ignimbrites erupted from the Mogollon caldera cluster. Petrographic and geochemical data are interpreted in stratigraphic succession of the BCT in an effort to constrain plumbing system processes and assess geochemical variations. Finally, using whole-rock major- and trace-element data, I present the relationship of the BCT to other regional ignimbrites of similar age in the western MDVF.

2. The Bursum Ignimbrite Complex

2.1. Geology. The Bloodgood Canyon Tuff (BCT) and two units believed to be associated with it, the Apache Spring Tuff (AST) and Fanney Rhyolite, were erupted from the youngest of three nested calderas: the Bursum caldera, a 40 km-wide resurgent caldera (Fig. 1; Elston, 2008; Ratté et al., 1984). The estimated volume of erupted products from the Bursum caldera is ~1200 km^3, but as much as 2500 km^3 of magma may have erupted prior to resurgence (Ratté et al., 1984).

At least five other ignimbrites erupted in the area since 36 Ma and formed calderas that the Bursum caldera overprints. The Mogollon caldera, which makes up the western wall of the Bursum caldera is the oldest caldera in the Mogollon Mountains (32 Ma; Ratté et al., 1984) and is associated with the Cooney Formation. Most of this ~15 km diameter caldera is buried by younger volcanic and sedimentary rocks (Ratté et al., 1984). On the eastern side of the Bursum caldera is the Gila Cliff Dwellings caldera, a 30 Ma caldera that collapsed during the eruptions of the Davis Canyon Tuff and Shelley Peak Tuff makes up the eastern wall of the Bursum caldera (Ratté et al., 1984). The Gila Cliff Dwellings caldera is filled in by the BCT and is overprinted by the Bursum caldera (Ratté et al., 1984). Best exposed portions of these calderas suggest they are volcano-tectonic depressions (VTD) as opposed to the traditional "Valles" type calderas in that they are complex collapse structures influenced by the regional tectonics. Where exposed, all three caldera margins show a major structural margin only on one side in the form of an arcuate fault zone (Elston et al., 1970; Ratté et al., 1984; Elston, 1984; 2008). After the eruption of the Bursum caldera, Basin and Range and Rio Grande rifting extended the nearby area and formed horst and grabens (Chapin et al., 2004).

2.2. Stratigraphy. 2.2.1. Older Tuffs in the Western Mogollon-Datil Volcanic Field. The Cooney Tuff (34 Ma) is the primary erupted unit from the Mogollon caldera, and is composed of three Members: the Whitewater Creek Member, the Cooney Canyon Member, and the South Fork Member (Ratté et al., 1984). In this paper, these units as a whole will be referred to as the Cooney Formation. The eruption that formed the Whitewater Creek Member (31.8 ± 2.8 Ma; Ratté, 1981) initiated the collapse of the Mogollon caldera. The resulting high-silica rhyolite was a simple cooling unit with 5%

phenocrysts of sanidine, with minor sodic plagioclase, quartz, biotite, Fe-Ti oxide, and zircon, and ~10% lithics of rhyolite and andesite (Ratté, 1981). The Cooney Canyon Member (32 ± 1.2 Ma; Bikerman, 1972) is composed of a series of tuffs as the Mogollon caldera continued to subside (Ratté et al., 1984). Thin rhyolitic to dacitic ash flow tuffs are separated by thin volcaniclastic sandstone beds (Ratté, 1981). The Cooney Canyon Member is more crystal-rich than the Whitewater Creek Member at 50% phenocrysts of plagioclase, biotite, Fe-Ti oxides, and some augite. Volcaniclastic sandstone 150 m thick overlies the Cooney Canyon Member (Ratté, 1981; Ratté et al., 1984). Basaltic dikes cut into the Cooney Formation, but they are the only basaltic rocks seen that erupted during the ignimbrite flare-up.

The Davis Canyon Tuff and the Shelley Peak Tuff are two possible units responsible for the Gila Cliff Dwellings caldera collapse, though this relationship is poorly constrained (Ratté et al., 1984). The Davis Canyon Tuff (29.01 Ma) is a 200-400 km^3, compositionally zoned, high-silica rhyolite outflow sheet (Ratté et al., 1984; McIntosh et al., 1990). Within the tuff are abundant white, gray, or reddish-brown pumice clasts with coarse and stringy textures (Ratté et al., 1984). Sanidine, quartz, and biotite phenocrysts exist, but they are small and sparse within the Davis Canyon Tuff (Ratté et al., 1984; 1994; McIntosh et al., 1990). The Shelley Peak Tuff (28.59 ± 0.11 Ma; McIntosh et al., 1990) is a 100-200 km^3, rhyolitic to rhyodacitic outflow sheet (Ratté et al., 1984). Abundant white pumice clasts are observed in this unit, but it is distinguished from the Davis Canyon Tuff by the red matrix and abundant phenocrysts of plagioclase, biotite, and light green clinopyroxene (Ratté et al., 1984).

2.2.2. Bursum Caldera Ignimbrites. The Bloodgood Canyon Tuff (BCT; 28.0 Ma; McIntosh et al., 1990) is a compositionally zoned high-silica rhyolite, ash-flow tuff, composed of a single cooling unit at least 600 m thick and spanning over an area of 15,000 km^2 (Ratté, 1981; Ratté et al., 1984). BCT rocks are crystal-rich, containing 10-30% phenocrysts of sanidine and quartz, sodic plagioclase, and <1% sphene, Fe-Ti oxide, biotite, oxyhornblende, zircon, and apatite (Ratté, 1981). The BCT unconformably overlies the Shelley Peak Tuff and Davis Canyon Tuff close to the caldera, but farther away from the Bursum caldera there are ash-fall beds overlying other local volcanic rocks.

The Apache Spring Tuff (AST; 27.9 Ma; McIntosh et al., 1990) is a >1000 m thick, compositionally zoned rhyolitic to quartz latitic ash-flow and intracaldera fill tuff (~1200 km^3) with no base exposed (Ratté, 1981; Ratté et al., 1984; Elston, 2008). Coarse debris avalanches and mudflows from the caldera walls deposited megabreccia, mesobreccia, and fluvial conglomerates separating the AST ash-fall deposits (Ratté et al., 1984; Ratté et al., 1979). The AST contains 15-55% phenocrysts of sanidine, quartz, and oligoclase, with minor Fe-Ti oxide, sphene, biotite, zircon, and apatite (Ratté, 1981). The AST is only found in outcrop near the walls of the Bursum caldera due to erosion and the Fanney Rhyolite resurgent dome that covers most of the Bursum caldera.

The Fanney Rhyolite is a series of crystal-poor flow-banded rhyolite lava flows and pyroclastic flow deposits that erupted along the ring-fractures and comprise the resurgent domes of the Bursum caldera (Ratté, 1981). Bikerman et al. (1992) reported K-Ar dates of 24.4 Ma and 26.0 Ma for two samples of Fanney Rhyolite. The Fanney Rhyolite is composed of sparse feldspar and quartz phenocrysts and has a white to light-

gray, aphanitic (or glassy to vitrophyric at chilled margins) matrix (Ratté, 1981). The Deadwood Gulch Member of the Fanney Rhyolite is a 200 m pumiceous tuff breccia and partially welded, crystal-poor ash-flow tuff produced by pyroclastic eruptions of the Fanney Rhyolite. At the base of the Deadwood Gulch is a 1 m thick bed of reworked pyroclastic material and Fanney Rhyolite intrusions (Ratté, 1981). Both of these units are extremely altered and the Fanney Rhyolite is extensively mineralized with copper, lead, gold, and silver deposits (McLemore, 1994).

3. Methods

Selective sampling of 31 whole rock samples from the BCT, AST, Fanney Rhyolite, Davis Canyon Tuff, and Shelley Peak Tuff and stratigraphic measurements of the BCT in the field were done to ensure an accurate portrayal of the stratigraphic variation in the BCT and volume estimates. Unaltered samples were collected from all three units to ensure accurate geochemical analyses. Bulk rock major- and trace-elements were measured on five BCT samples, two Fanney Rhyolite samples, one AST sample, two Shelley Peak samples, and one Davis Canyon Tuff sample using X-Ray Fluorescence (XRF) and Inductively-Coupled Plasma Mass Spectrometry (ICP-MS) at Washington State University using the methods of Johnson et al. (1999) and Jarvis (1988), respectively.

Three BCT samples were selected to measure Sr, Nd, and Pb radiogenic isotope ratios based on stratigraphic position. Analysis of Sr, Nd, and Pb was performed using a ThermoFinnegan Neptune MC-ICP-MS at New Mexico State University. Approximately 250 mg of whole rock powder used in major- and trace analyses was dissolved in HNO_3,

HF, HCl, and HBr and separated by column chemistry, following procedures outlined in Ramos (1992). Measured $^{87}Sr/^{86}Sr$ and $^{143}Nd/^{144}Nd$ ratios were normalized to $^{86}Sr/^{88}Sr=0.1194$ and $^{146}Nd/^{144}Nd=0.7219$, respectively (Újvári et al., 2012). Pb samples were analyzed using nine Faraday collectors and an ion counter by MC-ICP-MS and were compared to the standard NBS 981 ($^{208}Pb/^{204}Pb \approx 36.662 \pm 0.002$, $^{207}Pb/^{204}Pb \approx 15.462 \pm 0.001$, $^{206}Pb/^{204}Pb \approx 16.928 \pm 0.001$) to monitor precision of the analyses. Analyses were within analytical error of known standard values and no corrections were made.

4. Results

4.1. Revision to Erupted Volume of the Bloodgood Canyon Tuff. Stratigraphic sections were measured at BCT outcrops chosen based on their accessibility and location in the extent map of Ratté (1984). Many outcrops were exposed without a top boundary due to erosion, so thickness measurements are considered conservative. Little stratigraphic data is available for the eastern extent of the BCT due to the lack of updated geologic maps and inaccessibility in the Gila Cliff Dwellings National Monument. Thickness varied between 10 m to 400 m. An extent map (Fig. 2) based on these measurements was constructed which identifies a farther extent from the caldera than previously reported by Ratté et al. (1984). I suggest a new total volume of the BCT at 1300 $km^3 \pm 100$ km^3. I assume error in this volume as the area may have been subject to some regional extension, erosion, and secondary thickening.

4.2 Revision to Ignimbrite Stratigraphy of the Bloodgood Canyon Tuff. A suite of petrologic data provides evidence about the character of major eruptions in the Mogollon caldera cluster and specifically, the Bloodgood Canyon tuff.

(1) Stratigraphic sections lack plinian-fall deposit at the base of the unit and lack the coarse grained expression of a typical deposit (Rosi et al., 1999). These features attest to the lack of initial plinian-fall stage that is typical for eruptions of ignimbrites.

(2) The pumice-poor, fine grained and highly indurated nature of ignimbrites typical of dense pyroclastic flows (Ratté et al., 1984; Elston, 2008).

(3) Increased crystallinity during eruption progression and a change in mineralogy.

(4) Petrological evidence from BCT samples for a change in volatile contents requires a complex evolution of pre-eruptive degassing and an external trigger for eruption (discussed in later sections).

(5) Estimated volumes of the intracaldera ignimbrites dominate outflow volumes, implying early collapse (Ratté et al., 1984; Elston, 2008).

These observations can be reconciled in a model where the BCT was emplaced during an eruption(s) of very high mass eruption rate that led to column collapse at the onset of eruption (De Silva et al., 2006) The BCT consists of widespread deposits around the Bursum caldera (Fig. 1). It is characterized by its purple-white-pink matrix and large (1-2 mm), abundant, quartz and feldspar grains. The matrix can be non-welded and pink to welded and purple/white.

The base of the BCT is defined by the unconformable contact with the Shelley Peak Tuff outside of the Bursum caldera. The base is unwelded, relatively crystal-poor (12% crystallinity), contains pumice fragments (11%), with some ~1 cm fragments of the Shelley Peak Tuff, and has a pink matrix (Alma Unit; Fig. 3). Visible mineral phases include quartz, feldspar, biotite, Fe-Ti oxides, and hornblende. Above this is the Bottom

Reserve Unit, found in both the outcrop in contact with the Shelley Peak Tuff and an outcrop outside of Reserve (Fig. 3). These outcrops define the middle of the BCT, and are welded, crystal rich (22% crystallinity), contains large welded pumices (1 in-10 in, Fig. 4a), and has a light purple matrix (Bottom Reserve Unit; Fig. 3). Visible mineral phases include quartz, feldspar, biotite, and Fe-Ti oxides.

The top of the BCT is welded, moderately crystalline to crystal-rich (17 to 44% crystallinity) with some pumice (Top Reserve Unit; Fig. 3). Visible mineral phases include quartz, feldspar, Fe-Ti oxide, and biotite. The 180-SP-3 and 12-RE-1 and -2 sections are associated with the Top Reserve Unit because of their similarities in petrography. Crystallinity and degree of welding are the only things that vary within these units. 180-SP-3 is a non-welded tuff with a pink matrix and high crystallinity (45%) while 12-RE-1 and -2 are welded with a purple matrix and vary between 20-32% crystallinity (the higher crystallinity being downsection). Visible mineral phases include quartz, feldspar, Fe-Ti oxide, and biotite. On the western wall of Bursum caldera are the MO-03 and MO-02 outcrops, associated with the Top Reserve Unit. Both samples are partially welded and contain ~1% pumices, but the MO-02 sample has a purple matrix and is crystal-rich (39% crystallinity), while the MO-03 sample has a pink matrix and is more crystal-rich (45% crystallinity). Visible mineral phases include quartz, feldspar, Fe-Ti oxide, and biotite.

On the eastern side of the Bursum caldera are the Bottom and Top Elk Ridge units (Fig. 3). The Bottom Elk Ridge unit is welded, crystal-poor (14% crystallinity), contains thin (2 mm thick) pumice veins, and has a white matrix. The Top Elk Ridge unit is

unwelded, crystal-poor (10% crystallinity), contains spherulites, and has a white matrix. Visible mineral phases include quartz and feldspar.

The AST is not found in direct contact with the BCT and $^{39}Ar/^{40}Ar$ ages of the BCT and AST are within error of each other (McIntosh et al., 1992) but the AST is assumed to be younger than the BCT because it is only found as intracaldera fill (Ratté et al., 1984). It contains many lithic fragments of the BCT that are ~1 cm long (>4 modal %), welded pumices ~1.5 cm long (~3 modal %), and is crystal-rich (28% crystallinity). Visible mineral phases include quartz, feldspar, Fe-Ti oxide, and biotite.

The Fanney Rhyolite and Deadwood Gulch Member are also not found in direct contact with the BCT or the AST. The Fanney Rhyolite resurgent dome is a flow-banded rhyolite with quartz glomerocrysts and a purple-pink matrix. Inclusions of andesite are found in samples near the western rim of the Bursum caldera where the Fanney Rhyolite and Deadwood Gulch Member are both present. The Deadwood Gulch Member is a non-welded, crystal-poor (4% crystallinity), vesicular tuff that contains mostly lithics and has a pink matrix. Visible mineral phases include quartz and feldspar.

4.3. Petrography. Thin sections from the BCT reveal mainly populations of sieved and euhedral alkali feldspar grains (Or_2-Or_{42}) and quartz, but there are petrographic differences within the stratigraphic section (Fig. 3). The base of the BCT's mineral phases include alkali feldspar, quartz, biotite, hornblende, and Fe-Ti oxides. Alkali feldspar grains average compositions are Or_{51} and are mostly euhedral with no major zoning. Accessory phases include titanite and apatite, with some zircon trapped in feldspar grains.

The Bottom Reserve Unit's mineral phases include alkali feldspar, quartz, biotite, hornblende, and Fe-Ti oxides. Alkali feldspar grains contain more perthite textures and a wider range of compositions than other sections of the BCT (Or_{14}-Or_{53}; Fig. 4c). Accessory phases include titanite and zircon.

The Top Reserve Unit's mineral phases include alkali feldspar, quartz, biotite, hornblende, and Fe-Ti oxides. Alkali feldspar grains have fewer perthite textures than the Bottom Reserve Unit and average compositions are Or_{46} (Fig. 4d). Zircon is the main accessory phase in this section of the BCT. The Bottom/Top Elk Ridge Units' mineral phases include alkali feldspar, quartz, and biotite.

Mineral phases in the AST include alkali feldspar, quartz, biotite, and Fe-Ti oxides. Quartz grains in the AST are as large as the quartz grains in the middle and top section of the BCT. Just like in the BCT, the feldspars are not zoned and there is only some twinning present. There is trace zircon and altered amphibole.

The Fanney Rhyolite has the same mineral phases as the BCT. The lava flow located within the Bursum caldera has glomerocrysts of quartz and unzoned feldspar with flow banding around it and altered biotite and titanite. Some bands within the flow have been devitrified to quartz. Phenocryst quartz and feldspar grains are the same size as quartz and feldspar grains in the top and middle section of the BCT. Mineral phases present in the Deadwood Gulch Member are alkali feldspar, quartz, and Fe-Ti oxides.

4.4. Whole-Rock Geochemistry. Major element geochemistry of whole-rock samples are presented in Table 1 and illustrated in Figures 5 and 6. All whole-rock samples are classified as rhyolites, according to the total alkali vs silica diagram (Le Maitre et al., 2002) with the exception of one BCT sample (trachydacite) and two Fanney

Rhyolite samples (dacite) collected outside of this study (Fig. 5). SiO_2 ranges from 68.3 to 80.1 wt % SiO_2 in the BCT and 69.4 to 77.3 wt % in the Fanney Rhyolite (Fig. 5). The AST and one sample of the BCT have silica contents >80 wt %. Al_2O_3 (10.6-16.36 wt %), Na_2O (1.83 to 3.83 wt %) and K_2O (4.82 to 6.80 wt %) have no significant variation relative to SiO_2 wt % in the BCT. MgO (0.091 to 1.6 wt %), FeO (0.79 to 2.51 wt %), TiO_2 (0.12 to 0.52 wt %), and CaO (0.09 to 1.27 wt %) generally decrease with increasing SiO_2 wt % in the BCT. The AST trends with the BCT in all major elements. Na_2O and K_2O wt % of the Fanney Rhyolite is off trend from the BCT but MgO, FeO, TiO_2, and CaO generally trend with the BCT.

Whole-rock trace element concentrations are presented in Table 2 and illustrated in Figure 7. All units have strong Sr, P, Ti, and Eu depletion. Trace elements do not vary much with increasing SiO_2, but variations within the BCT do occur in Zr, Nd, and Y (Fig. 7). Bivariate trace element plots are shown in Figure 8. La/Yb ratios are <15 in the BCT, AST, and Fanney Rhyolite (<8, 13.6, and <9, respectively), reflecting the HREE depletion relative to LREE, and generally decrease with increasing Yb (Fig. 8). Sr/Y ratios are below 2.6 for the Fanney Rhyolite and BCT and generally decrease with increasing Y, but the AST Sr/Y ratios are significantly different (12.9; Fig. 8). The BCT and Fanney Rhyolite have much lower Eu/Eu* ratios than the AST (<0.24 vs. 0.53) and only slightly increase with increasing Sm/Yb ratios in the BCT. Sm/Yb ratios are <2 for all units. Rb/Sr ratios decrease with increasing Sr concentrations and Sm/Yb ratios are <2 in all units. Dy/Dy* ratios compared to $(Dy/Yb)_N$ are shown in Figure 9. Samples from the base of the BCT, Fanney Rhyolite, and AST all have Dy/Dy* <0.6 while the middle and top of the BCT have Dy/Dy* ratios that range from 0.7-0.9.

Rare Earth Elements (REE) normalized to chondrite (Wasson, 1985) are shown in Figure 10. The BCT, AST, and Fanney Rhyolite are depleted in HREE relative to LREE. The Fanney Rhyolite has lower overall REE concentrations than the BCT and the AST has the lowest HREE concentrations (Fig. 10). The Fanney Rhyolite has a significantly lower depletion in HREE than the BCT or AST, steeply dropping from relatively enriched LREE to depleted Eu, while the BCT has the highest concentrations of HREEs, but concentrations range within the unit. The BCT has a relatively steady slope of HREEs, and does not drop in concentration for LREEs or HREEs as steeply as the Fanney Rhyolite does.

4.5. Radiogenic isotopes. Isotope ratios collected from this study are presented in Table 3 and Sr and Nd ratios are illustrated in Figure 11 combined with Sr and Nd ratios published by Bikerman (1989). $^{87}Sr/^{86}Sr$ ratios range from 0.71321-0.727142 and $^{143}Nd/^{144}Nd$ ratios range from 0.51222-0.512288 in the BCT (Bikerman, 1989). Initial Sr and Nd isotope ratios were calculated for an age of 28.0 Ma. $^{87}Sr/^{86}Sr_i$ range from 0.708222 to 0.711396 and $^{143}Nd/^{144}Nd_i$ range from 0.512253 to 0.512256. $^{206}Pb/^{204}Pb$ ratios range from 18.740-18.769, $^{207}Pb/^{204}Pb$ ranges from 15.581-15.591, and $^{208}Pb/^{204}Pb$ ranges from 38.868-38.911. Radiogenic isotopes collected from this study are plotted in Figure 12 in order of their stratigraphic height. The top of the BCT is more radiogenic than the base of the section (e.g. $^{87}Sr/^{86}Sr$= 0.725120 vs. 0.718746; $^{87}Sr/^{86}Sr_i$=0.71321 vs. 0.711396) with off-trend anomalies in the middle of the section ($^{87}Sr/^{86}Sr$=0.727142).

5. Discussion

5.1. Physical Aspects for Styles of Zonation in the Bloodgood Canyon Tuff.

Strong evidence for the presence of crystal mushes is found in many large ignimbrites (e.g. Campanian Ignimbrite; Forni et al., 2016; Carpenter Ridge Tuff; Bachmann et al., 2014; Okataina Volcanic Complex; Graeter et al., 2015). Crystal mushes are magma bodies defined by a crystallinity ≥45% that are incapable of erupting or convecting without reducing the crystallinity (Bachmann, 2004).Crystals form a rigid skeleton and compact, allowing lower density, interstitial liquid to form an eruptible lens of rhyolite-composition, crystal-poor liquid near the top of the magma body (Bachmann, 2004; Bachmann and Bergantz, 2008). The lens can also form when crystallinity is at <50% if crystals are allowed to settle (Bachmann, 2004). This lens can be erupted as clusters of small-volume rhyolitic lava flows (e.g. the Taylor Creek Rhyolite; Duffield and Dalrymple, 1990) or as crystal-poor, pyroclastic precursors to more crystal-rich, mafic pyroclastic material (Bachmann, 2004).

Crystal mush can be remobilized if subjected to additional heat from intruding magma (Bachmann and Bergantz, 2006). Intruding magma can provide heat to the overlying mush and partially remelt and unlock the crystal skeleton without thoroughly mixing with the crystal mush (Bachmann and Bergantz, 2006; 2008). Remobilization can occur fairly quickly, depending on the input rate and size of the mush (e.g. Pinatubo, a few hundred meters thick, was remobilized in half a year; Huber et al., 2012). Numerical modeling by Bergantz et al. (2015) has shown that, over time, the intruding magma can thoroughly mix with the mush to produce a new melt, stimulate self-mixing, and produce complex zoning in crystals, and is evidenced by a Franklin sill on Victoria Island, Canada

(Hayes et al., 2014). However, the BCT displays no such complex zoning, so eruption must have occurred before the intruding magma thoroughly mixed with the crystal mush, but after it stimulated self-mixing. Early withdrawal of magma, represented by the base of the BCT, is quite evolved and for most elements show ranges of concentrations that are limited compared to the whole sequence but are nonetheless significant (Figs. 5-7). Because of that I do not consider mixing followed by fractional crystallization to be a viable model to explain variation within the BCT. In the trace element and radiogenic isotopic data presented by Bikerman et al. (1989; 1992) and in this study, the scatter of trace element concentrations at base of the stratigraphic section is nearly as great as the ignimbrite as a whole. This is in contrast to the feldspar chemistry and contents, from which I infer that magmas tapped from various parts of the reservoir were ejected simultaneously during extraction from a mush.

This process can even lead to eruption if the rate of volume increase and over pressurization overcome the strength of the surrounding wallrock (Bachmann and Bergantz, 2008). Therefore, in cold crust, it would be difficult for large amounts of magma to accumulate because of dike or sill propagation (Jellinek and DePaolo, 2003). In the case of the BCT, the crust was warmed by the initiation of the ignimbrite flare-up and extension from the Basin and Range, Transition Zone, and the Rio Grande rift, allowing for large magma accumulation (Chapin et al., 2004).

5.2. Evolution of the Bursum Caldera System and Origin of Compositional Variation. Zoned ignimbrites with a basal zone of crystal-poor, high-silica rhyolite and an upper zone of crystal-rich, rhyolite to dacite have been suggested to be the result of eruption from large zoned magma chambers, rapidly emptied from the top down (Lipman, 1967; Smith, 1979; Wolff et al., 1990; Chamberlain, 2015). Compositional variation within

ignimbrites is not uncommon. Many large-volume ignimbrites exhibit compositional normal zoning (e.g. the Bishop Tuff; Hildreth and Wilson, 2007) or reverse zoning (e.g. the Bandalier Tuff; Wolff et al., 2011) due to magma chamber stratification or some heterogeneity due to different magma packages (e.g. the Ora ignimbrite; Willcock et al., 2015). Most compositionally zoned ignimbrite sheets exhibit a progressive upward increase in crystal content, general decrease in bulk SiO_2 content, and trace element ratios that become less evolved (Chamberlin, 2015). Intruding magma of different composition is often the cause of compositional variation within the magma chamber (Willcock et al., 2015). Processes contributing to compositional variation could include: (1) varied degrees of mixing, assimilation, crustal melting or recharge filtering; (2) spatially inhomogenous crystal-melt-vapor fractionation within a zoned magma reservoir; (3) incremental assembly of a laterally or vertically compositionally zoned magma chamber; (4) meter-scale melt-crystal segregation and or crystal mush development by convective sorting during magma flow towards the conduit (Hildreth and Wilson, 2007). These processes are in contrast to large volume crystal rich ignimbrites that are relatively homogeneous and lack vertically zoned outflow sheets (Lipman, 2000; Bachmann and Bergantz, 2008; Lipman and Bachmann, 2015).

Large-volume, densely welded ignimbrite sheets, such as the Bloodgood Canyon Tuff, must be erupted in a few days to weeks. The Bloodgood Canyon Tuff represents a single cooling unit that was formed from the eruption of a highly evolved magma from a single integrated magma reservoir prior to eruption. The stratigraphy of the BCT suggests that the crystallinity of the tuff exhibits a progressive nearly linear upward increase in phenocryst content (10-45 vol.%) and in particular an increase in sanidine phenocrysts.

As a result, I suggest that prior to eruption, the cooler outer margin of a large magma body consisted of a rigid mush of interlocking crystals (>50 vol.%) and interstitial melt whereas the inner core of the body consisted of a more mobile crystal mush (<45 vol.%; Bachmann and Bergantz, 2008). Evidence is compelling that the BCT represents magma that has been stored in a unitary zoned chamber, that was mostly differentiated, lowest in temperature, richest in volatiles, and poorest in phenocryst at the roof, where withdrawal began. These observations suggest that the magma chamber was tapped from the top down, and emptied from the center outward collapsing the roof of the chamber early in the eruption cycle disrupting the rigid mush and allowing the eruption to be sustained to form the upper zones of the ignimbrite sheet with higher crystal contents. Major element concentrations in samples from the BCT are similar with the exception of SiO_2, but trace elements vary within the unit depending on stratigraphic position. Depletion in Sr and Ba in the whole section is consistent with feldspar fractionation. The basal zone of the unit contains the lowest Sm/Yb and Dy/Dy* trace element ratios and lowest Sr and Nd isotopic ratios. While these ratios are still highly evolved, I suggest a magmatic source that is amphibole or clinopyroxene stable at the onset of eruption (Davidson et al., 2013). This is supported by the presence of amphibole in in the basal zone. Amphibole was likely fractionated early but as mush mobilization continued lowering the Sm/Yb ratio, amphibole may have become unstable (Kay et al., 2010). Dehydrogenation textures around amphibole suggest water contents and chamber pressure changed rapidly altering the phenocrysts to Fe-Ti oxides.

Fractionation of titanite observed in the basal and middle zones of the BCT is likely responsible for the depletion in the middle REE relative to LREE. This has been

shown to be effective method of depletion of MREEs in cumulate-derived large-volume ignimbrites (Wolff et al., 2015; Fig. 10) and suggests that the relatively high HREE contents and elevated Y concentrations reflects evolution of the BCT from a trachyandesitic to andesitic composition arc magma (Michelfelder et al., 2013). The middle of the BCT has the highest concentrations of HREEs, but Dy/Dy* and Eu/Eu* ratios are between the base and top of the BCT. In general, the middle of the BCT is more radiogenic than the rest of the section, though $^{143}Nd/^{144}Nd$ ratios are between the base and the top of the section (Fig. 12). I suggest that this reflects the greatest influence of source material prior to extensive melt rejuvenation. Many studies have shown that melt rejuvenation and caldera forming eruptions are driven by recharge of a more primitive magma (Lipman, 2007; Hildreth and Wilson, 2007; Bachmann and Bergantz, 2008). I suggest that this magma began the process of convection and remobilization rapidly and effectively changed the composition of the magma in the middle zone of the ignimbrite sheet.

The top zone of the stratigraphic section contains Sm/Yb ratios (Fig. 8) and Dy/Dy* ratios (Fig. 9) that are higher than in the basal zone of the section. These ratios suggest a source that is compositionally different than the base and potentially garnet-stable or sediment-melt derived. However, this is contradictory to Sr/Y ratios (Fig. 8) that are too low to indicate garnet presence, suggesting that these rocks are derived from a source that had signatures of sediment melt. This is the only zone of the section where this signature is observed and this is distinct in comparison to the Apache Spring tuff or the Fanney Rhyolite, which are associated as later eruptions from the same chamber (Bikerman et al., 1992). I suggest that the geochemical variations observed in the BCT

are strongly controlled by the crystallinity of the rock induced by crystal/melt separation and accumulation in the reservoir. I conclude that neither fractional crystallization nor mixing induced by recharge alone can account for the variation observed. I suggest that "parental" andesite magmas intruded the base of the chamber but could not progress through the mush and were filtered to dacite or rhyolite in composition. This magma triggered instability of low temperature mineral phases, such as K-rich feldspar and quartz and other accessory phases, and the formation of high silica rhyolite melts locally enriched in HREEs and depleted in Sr, and Ba from which sanidine and quartz could be re-crystallized (Forni et al., 2016). This melting eventually reduced the crystallinity of the crystal mush making it rheologically eruptible (Huber et al., 2012).

5.4. Proposed Model. 5.4.1. Source Constraints and Implications for the Source of the Bursum Caldera Magmas. Previous studies that have included the Bloodgood Canyon Tuff have mostly focused on regional interpretations and as a result the endmember magma compositions have not been defined (Bikerman, 1994). In the search for the parent magma of the BCT in this study I focus on the Cooney Formation, Shelley Peak and Davis Canyon tuffs, contaminating and mixing with basaltic dikes found intruding the caldera and surrounding area, and crustal compositions. Since fractional crystallization is the proposed dominant process in the evolution of BCT magma I have performed fractional crystallization and assimilation fractional crystallization models using compatible and incompatible elements in the system (Table 4). Mass balanced models (AFC and mixing) fail to create any part of the BCT due to the ignimbrites highly involved composition. AFC models require over 70% assimilation to create the most evolved compositions and typically fail to create trends that require more FeO and Sr

than are available to the end members. Moreover, the models seem to be unrealistic segregation rates preventing separation of crystal-poor magma early in the stratigraphy. The Burro Mountain Granite (the likely basement composition in the area; Amato et al., 2011) modeled with these components also did not yield good mass-balanced results. The compositional changes within the stratigraphic section of the BCT makes it difficult to find a model that created the whole section of the BCT. Keeping this in mind, separate models for different sections of the BCT were created.

Trace-element patterns and accessory phase differences between the bottom and top of the section suggest that the top of the section was sourced in a more evolved melt that was more crystal-rich and contained signatures from Precambrian island arcs (Dy/Dy* ratios >0.8; higher SiO_2, and more radiogenic) while the bottom of the section was sourced in a crystal-poor, less evolved melt that contained signatures of amphibole/clinopyroxene fractionation (Dy/Dy* ratios <0.6; lower SiO_2, less radiogenic). Therefore, I conclude that neither FC nor AFC models are suitable for describing the full behavior of the BCT.

5.4.2. Evolution Model. Mass balanced AFC models of the Davis Canyon Tuff (Rentz et al., 2016) contaminated by amphibolite compositions from the Burro Mountains (Amato et al., 2011) successfully model the basal zone of of the BCT (180-SP-2; Fig. 13a). Specific compositions and parameters are presented in Table 4. Crustal melting of an amphibolite-composition crust contaminating the residual magma after the eruption of the Davis Canyon Tuff composition provides similar Dy/Dy* ratios, which vary between a source that is fractionating amphibole towards sediment melts/garnet stable sources (Fig. 10). The amphibolite-composition endmember has been observed in the

Precambrian basement that is in the area and is an ocean island arc composition from the collision of the Matazaal terrane with the North American plate (Amato et al., 2011). The assimilation of this composition amphibolite with less than 20% assimilation explains the low Dy/Dy* signatures of the basal zone of the BCT and acts as the silicic end member for further processes (Fig. 10).

Mass balanced least-square mixing modeling of the top zone (MO-02 and MO-03) and the basal zone (180-SP-2) of the BCT successfully model the middle zone of the BCT (12RE-1 and 12RE-2; Fig. 13b). Specific compositions and parameters are presented in Table 4. This model suggests intra-chamber self-mixing with little to no outside influence. This model fits with the idea of remobilization of a mush by recharge filtering or by mafic recharge (Bachman et al., 2002, 2015). The top zone of the BCT represents the crystal immobile mush, requiring convection that would have resumed once the crystal skeleton became unlocked when intruding magma from the ignimbrite flare-up provided heat to the crystal mush. Evidence for this more-evolved mush comes from the higher Dy/Dy* ratios in the top of the BCT, which suggest a higher amount crustal contamination than the rest of the section, of a magma with similar $^{87}Sr/^{86}Sr$ ratios to the basal zone. The middle zone of the section contains ratios that are more radiogenic than the rest of the BCT providing further evidence that this zone is the result of preferential melting of low temperature phases early in the remobilization history. It is unclear if there is crustal melting happening in the middle of the chamber to cause this anomaly.

An evolution diagram for the BCT is shown in Fig. 14. The model in Fig. 14 assumes (1) that if the immobile crystal mush was located in Precambrian basement, the

surrounding basement was of gneiss composition, with amphibolite-composition lens was at the top of the magma chamber. This is assumed for this area based on the mapping for Precambrian basement presented in Amato et al. (2011) in the Burro Mountains to south and the requirement in mass-balanced modeling of the interaction amphibolite and Davis Canyon Tuff that does not form the rest of the BCT; and (2) that phenocrysts >1 mm were sourced from the immobile crystal mush because the time between the eruption of the Davis Canyon Tuff and the Bloodgood Canyon Tuff is only ~1 m.y., an unlikely time period to allow crystals to grow so large.

Modeling suggests that the magma that sourced the Davis Canyon Tuff is one of the endmembers of the BCT. Similarity in major- and trace-elements suggest these units were sourced and erupted from the same regional magma chamber. After the eruption of the Davis Canyon Tuff and Shelley Peak Tuff, the remaining magma of Davis-Canyon-Tuff-composition assimilated with an amphibolite-composition rock. This might have been the end of the evolutionary track, but the ignimbrite flare-up added a new phase. Upwelling mafic magma provided heat to an immobile crystal mush forming prior to the collapse of the Gila Cliff Dwellings caldera. This heat released some of the crystals from the rigid skeleton and allowed them to be carried in the convection current within the magma chamber (Bachman and Bergantz, 2008).

5.5. Relationships to Regional Units. It is unclear whether the AST is related to the BCT primarily because only one sample collected was considered unaltered. Based on stratigraphic position, major-element trends (Figs. 5 & 6), and petrographic textures, it is likely that the AST is sourced from the same chamber as the BCT, and continued erupting the crystal-rich bottom of the chamber. However, Eu/Eu* ratios in the AST are

much higher than the BCT and Fanney Rhyolite, suggesting feldspar fractionation was not occurring in the source of the AST or this feldspar was incorporated into the unit during eruption. Based on the higher Sr/Y ratios (Fig. 8), garnet may have been stable, but Dy/Dy* (Fig. 9) ratios are lower than those from the bottom of the BCT, and too low to suggest garnet stability. These ratios suggest that the AST was sourced in a similar magmatic environment as the basal zone of the BCT, but with more crustal contamination and without feldspar fractionation. However, it is possible that lithic fragments, which occur throughout the AST in high volume, skewed major- and trace-element compositions. More sampling is required to determine the source of the AST.

The Fanney Rhyolite is likely related to the BCT based on major- and trace-elements (Figs. 5-10). The Fanney Rhyolite formed 2 m.y. after the eruption of the BCT, when the ignimbrite flare-up began to wane, and the remobilized crystal mush became rigid. The lack of crystals in the Fanney Rhyolite suggests it was an evolved lens of magma was squeezed out of the remaining immobile mush (Bachmann and Bergantz, 2008). Dy/Dy* ratios (Fig. 9) for the Fanney Rhyolite are close to the ratios for the basal zone of the BCT, suggesting that after eruption of the BCT, the magma began to fractionate amphibole/clinopyroxene. No petrologic model has formed the Fanney Rhyolite (Fig. 13a), and the samples from Bikerman et al. (1992) do not trend with samples collected in this study (Fig. 5; Fig. 6), further complicating efforts to model the Fanney Rhyolite. Further study is required to determine the full relationship of the Fanney Rhyolite to the BCT.

6. Conclusions

Whole-rock major- and trace-element, radiogenic isotope ratios, and petrologic modeling methods provide evidence that the Bloodgood Canyon Tuff was erupted from remobilization of rhyolite composition crystal mush. The following conclusions can be made about the magmas erupted from the Bursum Caldera.

1. The pumice-poor nature of the BCT suggests that the eruption was dense and collapse of the caldera occurred early in the eruption driving the continuation of the eruption and driving pyroclastic flows over plinian-fall deposits.

2. Compositional zoning within the ignimbrite suggest three compositional zones representing eruption from a stratigraphically zoned magma chamber. The stratigraphy of the BCT suggests that the crystallinity of the tuff exhibits a progressive nearly linear upward increase in phenocryst content (10-45 vol.%) and in particular an increase in sanidine phenocrysts. This suggests that prior to eruption, the cooler outer margin of a large magma body consisted of a rigid mush of interlocking crystals (>50 vol.%) and interstitial melt whereas the inner core of the body consisted of a more mobile crystal mush (<45 vol.%). Eruption started from center of the magma body driving evacuation from the center outward and from the top down.

3. Trace-elements (REEs, Dy/Dy*, Eu/Eu*) and radiogenic isotope ratios (Sr, Nd, and Pb) suggest a highly differentiated and contaminated source that was amphibole or clinopyroxene stable at the top of the chamber (Dy/Dy*=0.57) and had more crustal contamination at the bottom of the chamber (εNd= -6.7).

4. Petrologic modeling shows that the base of the BCT was formed from the crustal melting of amphibolitic-composition crust after the eruption of the Davis Canyon, but the middle of the section was formed from intra-chamber self-mixing between melt lens and crystal mush. The crystal mush was remobilized when incoming mafic material ponded and filtered below the crystal mush and provided heat to the overlying chamber. Once the crystal skeleton was released, it allowed the chamber to begin convecting again and mixed with the rhyolitic lens of the top of the chamber. Once the BCT erupted and collapsed the Bursum caldera, the AST erupted and evacuated another section of the chamber.

5. After 2 million years, the ignimbrite flare-up was waning, and the crystal mush had begun to lock up again (>50% crystallinity), forming another crystal-poor rhyolite lens that erupted as the Fanney Rhyolite. However, the relationship between the BCT, AST, and Fanney Rhyolite is still unclear, and further sampling is needed to establish a statistically viable correlation.

References

Amato, J., Heizler, M., Boullion, A., Sanderas, A.E., Toro, J., McLemore, V.T., and Andronicos, C.L., 2011, Syntectonic 1.46 Ga magmatism and rapid cooling of a gneiss dome in the southern Mazatzal Province: Burro Mountains, New Mexico: Geological Society of America Bulletin, v. 123, p. 1720-1744, doi: 10.1130/B30337.1.

Bachmann, O., and Bergantz, G., 2004, On the origin of crystal-poor rhyolites: extracted from batholithic crystal mushes: Journal of Petrology, v. 45, no. 8, p. 1565-1582, doi: 10.1093/petrology/egh019.

Bachmann, O., and Bergantz, G., 2006, Gas percolation in upper-crustal silicic crystal mushes as a mechanism for upward heat advection and rejuvenation of near-solidus magma bodies: Journal of Volcanology and Geothermal Research, v. 149, no. 1, p. 85-102.

Bachmann, O. and Bergantz, G., 2008, The magma reservoirs that feed supereruptions: Elements, v. 4, p. 17-21, doi: 10.2113/GSELEMENTS.4.1.17.

Bachmann, O., Deering, C.D., Lipman, P.W., and Plummer, C., 2014, Building zoned ignimbrites by recycling silicic cumulates: insight from the 1,000 km^3 Carpenter Ridge Tuff, CO: Contributions to Mineralogy and Petrology, v. 167, 13 p., doi: 10.1007/s00410-014-1025-3.

Bacon, C.R. and Druitt, T.H., 1988, Compositional Evolution of the Zoned Calcalkaline Magma Chamber of Mount-Mazama, Crater Lake, Oregon: Contributions to Mineralogy and Petrology, v. 98, no. 2, p. 224-256.

Bergantz, G., Schleicher, J.M., and Burgisser, A., 2015, Open-system dynamics and mixing in magma mushes: Nature Geoscience, v. 8, p. 793-795, doi: 10.1038/NGEO2534.

Bikerman, M., 1972, New K-Ar ages on volcanic rock from Catron and Grant Counties, New Mexico: Isochron West, no. 3, p. 9-12.

Bikerman, M., 1989, Rb, Sr, Rb-Sr, and isotopic Sr values for volcanic rocks from southwestern part of the Mogollon-Datil volcanic field: New Mexico Geology, v. 11, p. 76-83.

Bikerman, M., 1994, Are the western Mogollon-Datil mid-Cenozoic ash flows cogenetic? Pearce element ratios and isotope aspects of the question *in* New Mexico Geological Society Guidebook, 45th Field Conference: Soccorro, NM, New Mexico Geological Society, 187-192.

Bikerman, M., Bell, K., and Card, J.W., 1992, Strontium and neodymium isotopic study of the western Mogollon-Datil volcanic region, New Mexico, USA: Contributions to Mineralogy and Petrology, v. 109, no. 4, p. 459-470, doi: 10.1007/BF00306549.

Chamberlain, K., 2015, Unraveling the magmatic processes behind zoned fall units on Ascension Island, South Atlantic: 2015 American Geophysical Union Fall Meeting.

Chapin, C.E., Wilks, M., and McIntosh, W.C., 2004, Space-time patterns of Late Cretaceous to present magmatism in New Mexico-comparison with Andean volcanism and potential for future volcanism: New Mexico Bureau of Geology and Mineral Resources Bulletin, v. 160, p. 13-40.

Davidson, J., Turner, S., and Plank, T., 2013, Dy/Dy*: Variations arising from mantle sources and petrogenetic process: Journal of Petrology, v. 54, no. 3, p. 525-537, doi: 10.1093/petrology/egs076.

Davis, J.M., and Hawkesworth, C.J., 1993, The petrogenesis of 30-20 Ma basic and intermediate volcanics from the Mogollon-Datil volcanic field, New Mexico, USA: Contributions to Mineralogy and Petrology, v. 115, no. 2, p. 165-183, doi: 10.1007/BF00321218.

Davis, J.M., and Hawkesworth, C.J., 1994, Early calc-alkaline magmatism in the Mogollon-Datil Volcanic Field, New Mexico, USA: Journal of the Geological Society [London], v. 151, no. 5, p. 825-843, doi: 10.1144/gsjgs.151.5.0825.

De Silva, S., Zandt, G., Trumbull, R., Viramonte, J.G., Salas, G., and Jiménez, N., 2006, Large ignimbrite eruptions and volcano-tectonic depressions in the Central Andes: a thermomechanical perspective *from* Troise, C., de Natale, G., and Kilburn, C.R.J. (eds) Mechanisms of Activity and Unrest at Large Calderas, Geological Society, London, Special Publications, v. 269, p. 47-63.

DePaolo, D.J., 1981a, Trace element and isotopic effects of combined wallrock assimilation and fractional crystallization: Earth Planet Science Letters, v. 53, p. 189-202.

DePaolo, D.J., 1981b, A Neodymium and Strontium isotopic study of the Mesozoic Calc-alkaline granitic batholiths of the Sierra Nevada and Peninsular Ranges, California: Journal of Geophysical Research, v. 86, no. B11, p. 10470-10788.

Duffield, W. A. and Dalrymple, G. B., 1990, The Taylor Creek Rhyolite of New Mexico; a rapidly emplaced field of lava domes and flows: Bulletin of Volcanology, v. 52, p. 475–487.

Elston, W.E., Coney, P., and Rhodes, R.C., 1970, Progress report on the Mogollon Plateau Volcanic Province, southwestern New Mexico: No. 2*, *in* Woodward, L.A., ed., Tyrone-Big Hatchet Mountain-Florida Mountains Region: New Mexico Geological Society, 21st Annual Field Conference, Guidebook, p. 75-86.

Elston, W.E., 1984, Mid-Tertiary ash flow tuff cauldrons, southwestern New Mexico: Journal of Geophysical Research, v. 89, no. B10, p. 8733-8750, doi: 10.1029/JB089iB10p08733.

Elston, W.E., 2008, The ~28 Ma Bursum Cauldron, viewed from the Aldo Leopold Vista and from Holt Mountain, *in* Mack, G.H., Witcher, J.C., and Leuth, V.W., eds., Geology of the Gila Wilderness-Silver City area: New Mexico Geological Society, 59th Annual Field Conference, Guidebook, p. 14-16.

Forni, F., Bachmann, O., Mollo, S., de Astis, G., Gelman, S.E., and Ellis, B.S., 2016, The origin of a zoned ignimbrite: Insights into the Campanian Ignimbrite magma chamber (Campi Flegrei, Italy): Earth and Planetary Science Letters, v. 449, p. 259-271, doi: 10.1016/j.epsl.2016.06.003.

Gelman, S.E., Deering, C.D., Bachmann, O., Huber, C., and Gutiérrez, F.J., 2014, Identifying the crystal graveyards remaining after large silicic eruptions: Earth and Planetary Science Letters, v. 403, p. 299–306, doi: 10.1016/j.epsl.2014.07.005.

Glazner, A.F., Bartley, J.M., Coleman, D.S., Gray, W., and Taylor, R.Z., 2004, Are plutons assembled over millions of years by amalgamation from small magma chambers?: GSA Today, v. 14, no. 4, p. 5-11.

Graeter, K., Beane, R.J., Deering, C.D., Gravley, D., and Bachmann, O., 2015, Formation of rhyolite at the Okataina Volcanic Complex, New Zealand: New insights from analysis of quartz clusters in plutonic lithics: American Mineralogist, v. 100, no. 8-9, p. 1778-1789, doi: 10.2138/am-2015-5135.

Hayes, B., Bédard, J.H., and Lissenberg, C.J., 2014, Olivine slurry replenishment and the development of igneous layering in a Franklin Sill, Victoria Island, Arctic Canada: Journal of Petrology, v. 56, no. 1, p. 83-112, doi: 10.1093/petrology/egu072.

Hildreth, W. and Wilson, C., 2007, Compositional zoning of the Bishop Tuff: Journal of Petrology, v. 48, no. 5, p. 951-999, doi: 10.1093/petrology/egm007.

Huber, C., Bachmann, O., and Dufek, J., 2012, Crystal-poor versus crystal-rich ignimbrites: A competition between stirring and reactivation: Geology, v. 40, no. 2, p. 115-118, doi: 10.1130/G32425.

Jarvis, K.E., 1988, Inductively coupled plasma mass spectrometry; a new technique for the rapid or ultra-trace level determination of the rare-earth elements in geological materials: Chemical Geology, v. 68, p. 31-39.

Jellinek, A.M., and DePaolo, D.J., 2003, A model for the origin of large silicic magma chambers: precursors of caldera-forming eruptions: Bulletin of Volcanology, v. 65, p. 363-381, doi: 10.1007/s00445-003-0277-y.

Johnson, D.M., Hooper, P.R., and Conrey, R.M., 1999, XRF analysis of rock and minerals for major and trace elements on a single low dilution Li-tetraborate fused bead: Advances in X-ray analysis, v. 41, p. 843-867.

Kay, S., Coira, B., Caffe, P., Chen, C., 2010, Regional chemical diversity, crustal and mantle sources and evolution of central Andean Puna plateau ignimbrites: Journal of Volcanology and Geothermal Research, v. 198, p. 81-111, doi: 10.1016/j.jvolgeores.2010.08.013.

Kern, J.M., de Silva, S., Schmitt, A.K., Kaiser, J.F., Iriarte, R., and Economos, R., 2016, Geochronological imaging of an episodically constructed subvolcanic batholith: U-Pb in zircon chronochemistry of the Altiplano-Puna Volcanic Complex of the Central Andes: Geosphere, v. 12, no. 4.

Le Maitre, R.W., Streckeisen, A., Zanettin, B., Le Bas, M.J., Bonin, B., Bateman, P., Bellieni, G., Dudek, A., Efremova, S., Keller, J., Lamere, J., Sabine, P.A., Schmid, R., Sorensen, H., and Woolley, A.R., 2002, Igneous Rocks: A Classification and Glossary of Terms, Recommendations of the International Union of Geological Sciences, Subcommission of the Systematics of Igneous Rocks: Cambridge University Press, ISBN 0-521-66215-X.

Leeman, W.P. and Phelps, D.W., 1981, Partitioning of rare earths and other trace elements between sanidine and coexisting volcanic glass: Journal of Geophysical Research v. 86, doi: 10.1029/JB080i011p10193.

Lipman, P.W., 1967, Mineral and chemical variations within an ash-flow sheet from Aso caldera, southwestern Japan: Contributions to Mineralogy and Petrology, v. 16, no. 4, p. 300-327.

Lipman, P.W., 2007, Incremental assembly and prolonged consolidation of Cordilleran magma chambers: evidence from the Southern Rocky Mountain volcanic field: Geosphere, v. 3, no. 1, p. 42-70.

Lipman, P.W. and Bachmann, O., 2015, Ignimbrites to batholiths: Integrating perspectives from geological, geophysical, and geochronological data: Geosphere, v. 11, no. 3, p. 705-743, doi: 10.1130/GES01091.1.

Mack, G.H., 2004, Middle and Late Cenozoic crustal extension, sedimentation, and volcanism in the southern Rio Grande rift, Basin and Range, and southern Transition Zone of southwestern New Mexico, *in* Mack, G.H., and Giles, K.A., eds., The Geology of New Mexico: A Geologic History: New Mexico Geologic Society, p. 389-406.

Mahood, G.A. and Hildreth, E.W., 1983, Large partition coefficients for trace elements in high-silica rhyolites: Geochimica et Cosmochimica Acta, v. 47, p. 11-30, doi: 10.1016/0016-7037(83)90087-X.

McIntosh, W.C., Sutter, J.F., Chapin, C.E., and Kedzie, L.L., 1990, High-precision $^{40}Ar/^{39}Ar$ sanidine geochronology of ignimbrites in the Mogollon-Datil volcanic field, southwestern New Mexico: Bulletin of Volcanology, v. 52, no. 8, p. 584-601, doi: 10.1007/BF00301210.

McIntosh, W.C., Chapin, C.E., Ratté, J.C., and Sutter, J.F., 1992, Time-stratigraphic framework for the Eocene-Oligocene Mogollon-Datil volcanic field, southwest New Mexico: GSA Bulletin, v. 104, p. 851-871.

McLemore, V., 1994, Volcanic-epithermal deposits in the Mogollon-Datil volcanic field, west-central New Mexico, *in* Mogollon Slope (West-Central New Mexico and East-Central Arizona), Chamberlin, R. M.; Kues, B. S.; Cather, S. M.; Barker, J. M.; McIntosh, W. C.; [eds.], New Mexico Geological Society 45th Annual Fall Field Conference Guidebook, p. 299-309.

McMillan, N.J., Dickin, A.P., and Haag, D., 2000, Evolution of magma source regions in the Rio Grande rift, southern New Mexico: Geological Society of America Bulletin, v. 112, no. 10, p. 1582-1593.

McMillan, N.J., 2004, Magmatic record of Laramide subduction and the transition to Tertiary extension: Upper Cretaceous through Eocene igneous rocks of New Mexico *in* The geology of New Mexico: a geologic history: New Mexico Geological Society, Special Edition, v. 11, p. 249-270.

Michelfelder, G.S. and McMillan, N.J., 2012, Geochemistry, origin, and U-Pb zircon ages of the Sierra Cuchillo Laccolith, Sierra County, New Mexico, *in* Lucas, S.G., McLemore, V.T., Lueth, V.W., Spielmann, J.A., and Krainer, K., eds., Geology of the Warm Springs Region: New Mexico Geological Society, 63rd Annual Field Conference, Guidebook, p. 249-260.

Michelfelder, G.S., Feeley, T.C., Wilder, A.D., and Klemetti, E.W., 2013, Modification of the continental crust by subduction zone magmatism and *vice-versa*: Across-strike geochemical variations of silicic lavas from individual eruptive centers in the Andean central volcanic zone: Geosciences, v. 3, p. 633-667, doi: 10.3390/geosciences3040633.

Ramos, F., 1992, Isotope geology of the metamorphic core of the Central Grouse Creek Mountains, Box Elder County, Utah: Thesis for Masters of Science, The University of California-Las Angeles, 223 pages.

Ratté, J.C., 1981, Geologic map of the Mogollon quadrangle, Catron County, New Mexico: U.S. Geological Survey Geologic Quadrangle Map GQ-1557, scale 1:24 000, 1 sheet.

Ratté, J.C., Marvin, R.F., and Naeser, C.W., 1984, Calderas and ash flow tuffs of the Mogollon Mountains, southwestern New Mexico: Journal of Geophysical Research, v. 89, no. B10, p. 8713-8732, doi: 10.1029/JB089iB10p08713.

Ratté, J.C., Gaskill, D.L., Eaton, G.P., Peterson, D.L., Stotelmeyer, R.B., and Meeves, H.C., 1979, Mineral Resources of the Gila Primitive Area and Gila Wilderness, New Mexico: Geological Survey Bulletin 1451, 229 p.

Ratté, J.C., McIntosh, W.C., and Bove, D., 1994, Geologic map of the Milligan Mountain quadrangle, Catron County, New Mexico: U.S. Geological Survey, scale 1: 24,000.

Rentz, S., Michelfelder, G.S., and Salings, E., 2016, The Cooney Tuff: ash fall in a calk-alkaline subduction related volcanic field, southern New Mexico: Geological Society of America, Abstracts with Programs, v. 48, no. 7, doi: 10.1130/abs/2016AM-281935.

Rosi, M., Vezzoli, L., Castelmenzano, A., Grieco, G., 1999, Plinian pumice fall deposit of the Campanian Ignimbrite eruption (Phlegraean Fields, Italy): Journal of Volcanology and Geothermal Research, v. 91, p. 179-198.

Rudnick, R.L. and Fountain, D.M., 1995, Nature and composition of the continental crust: a lower crustal perspective: Reviews in Geophysics, v. 33, p. 267-309.

Seager, W. R., 2004, Laramide (Late Cretaceous–Eocene) tectonics of southwestern New Mexico, *in* Mack, G.H., and Giles, K.A., eds., The Geology of New Mexico: A Geologic History: New Mexico Geologic Society Special Publication, v. 11, p. 183-202.

Schnetzler, C.C. and Philpotts, J.A., 1970, Partition coefficients of rare-earth elements between igneous matrix material and rock-forming mineral phenocrysts; II: Geochimica et Cosmochimica Acta, v. 34, no. 3, p. 331-340, doi: 10.1016/0016-7037(70)90110-9.

Smith, R.L., 1979, Ash-flow magmatism: GSA Special Papers, v. 180, p. 5-28, doi: 10.1130/SPE180-p5.

Taylor, S.R. and McLennan, S.M., 1985, The continental crust: its composition and evolution: Oxford: Blackwell.

Újvári, G., Varga, A., Ramos, F.C., Kovács, J., Németh, T., and Stevens, T., 2012, Evaluating the use of clay mineralogy, Sr-Nd isotopes and zircon U-Pb ages in tracking dust provenance: An example from loess of the Carpathian Basin: Chemical Geology, v. 304-305, p. 83-96.

Wasson, J.T., 1985, Meteorites: their record of early solar-system history: W.H. Freeman and Co., New York, NY.

Wedepohl, K.H., 1995, The composition of the continental crust: Geochimica et Cosmochimica Acta, v. 59, p. 1217-1232.

Willcock, M.A.W., Bargossi, G.M., Weinberg, R.F., Gasparotto, G., Cas, R.A.F., Giordano, G., and Marocchi, M., 2015, A complex magma reservoir system for a large volume intra- to extra-caldera ignimbrite: Mineralogical and chemical architecture of the VEI8, Permian Ora ignimbrite (Italy): Journal of Volcanology and Geothermal Research, v. 306, p. 17-40, doi: http://dx.doi.org/10.1016/j.jvolgeores.2015.09.015.

Wolff, J.A., Wörner, G., and Blake, S., 1990, Gradients in physical parameters in zoned felsic magma bodies: implications for evolution and eruptive withdrawal: Journal of Volcanology and Geothermal Research, v. 43, no. 1-4, p. 37-55.

Wolff, J.A., Brunstad, K.A., Gardner, J.N., 2011. Reconstruction of the most recent volcanic eruptions from the Valles caldera, New Mexico: Journal of Volcanology and Geothermal Research, v. 199, p. 53–68.

Wolff, J., Ellis, B., Ramos, F.C., Starkel, W.A., Boroughs, S., Olin, P.H., Bachmann, O., 2015, Remelting of cumulates as a process for producing chemical zoning in silicic tuffs: A comparison of cool, wet and hot, dry rhyolitic magma systems: Lithos, v. 236-237, p. 275-286.

Zimmerer, M.J. and McIntosh, W.C., 2013, Geochronologic evidence of upper-crustal in situ differentiation: silicic magmatism at the Organ caldera complex, New Mexico: Geosphere, v. 9, no. 1, p. 155-169, doi: 10.1130/GES00841.1.

Table 1. Major- and trace-element compositions of the BCT, AST, Fanney Rhyolite (FR), Davis Canyon Tuff (DCT), and Shelley Peak Tuff (SPT) measured by XRF.

Sample #	MO-02	MO-03	180-SP-2	12-RE-1	12-RE-2	MO-05	MO-06
Unit	BCT	BCT	BCT	BCT	BCT	AST	FR
SiO_2 (wt%)	75.89	80.14	75.40	76.75	76.13	80.56	77.27
TiO_2 (wt%)	0.281	0.206	0.187	0.205	0.189	0.241	0.135
Al_2O_3 (wt %)	12.57	10.26	12.35	12.25	12.10	9.49	11.10
FeO* (wt %)	0.79	1.02	1.29	1.13	1.07	1.27	0.74
MnO (wt %)	0.004	0.021	0.082	0.071	0.077	0.022	0.038
MgO (wt%)	0.14	0.13	0.24	0.10	0.11	0.12	0.06
CaO (wt%)	0.16	0.09	0.31	0.26	0.24	0.28	0.10
Na_2O (wt %)	1.83	1.93	3.81	3.83	3.80	1.25	0.31
K_2O (wt %)	6.90	4.82	4.82	5.07	5.05	5.91	8.90
P_2O_5 (wt%)	0.032	0.021	0.016	0.011	0.011	0.057	0.007
Sum	98.58	98.64	98.52	99.69	98.78	99.19	98.67
LOI %	1.20	0.81	0.94	0.30	0.98	0.77	0.61
Ni (ppm)	2	1	6	2	2	2	2
Cr (ppm)	4	3	3	1	3	3	1
Sc (ppm)	4	2	5	3	3	3	2
V (ppm)	29	19	13	14	24	22	6
Ba (ppm)	342	205	57	58	61	418	82
Rb (ppm)	285	196	301	251	265	207	522
Sr (ppm)	106	114	30	20	18	262	54
Zr (ppm)	316	219	182	222	217	175	146
Y (ppm)	80	81	65	94	83	21	31
Nb (ppm)	26.2	23.3	35.6	31.2	32.3	12.6	21.0
Ga (ppm)	17	14	21	21	20	13	13
Cu (ppm)	6	6	4	2	2	3	2
Zn (ppm)	53	41	90	58	62	19	29
Pb (ppm)	13	15	44	28	24	11	18
La (ppm)	56	40	31	33	36	32	36
Ce (ppm)	128	92	70	85	78	60	71
Th (ppm)	23	20	36	29	29	14	25
Nd (ppm)	60	45	22	43	36	22	21
U (ppm)	4	3	6	6	7	2	4

Table 1 continued

Sample #	MO-31	180-SP-1	APA-1	APA-2
Unit	FR	SPT	SPT	DCT
SiO_2 (wt%)	76.67	71.33	71.91	76.16
TiO_2 (wt%)	0.140	0.319	0.374	0.142
Al_2O_3 (wt %)	12.40	13.60	13.86	12.81
FeO* (wt %)	0.83	1.67	1.80	0.97
MnO (wt %)	0.022	0.062	0.058	0.054
MgO (wt%)	0.09	0.49	0.26	0.10
CaO (wt%)	0.10	1.38	0.97	0.22
Na_2O (wt %)	0.64	4.32	3.79	3.59
K_2O (wt %)	6.79	4.67	5.16	4.85
P_2O_5 (wt%)	0.003	0.068	0.086	0.008
Sum	97.68	97.91	98.27	98.90
LOI %	1.63	1.51	1.71	1.06
Ni (ppm)	1	4	3	4
Cr (ppm)	1	3	1	2
Sc (ppm)	2	4	4	5
V (ppm)	9	19	18	7
Ba (ppm)	98	606	621	47
Rb (ppm)	323	177	198	221
Sr (ppm)	68	179	139	12
Zr (ppm)	165	240	287	153
Y (ppm)	27	32	39	47
Nb (ppm)	22.6	17.5	21.0	26.2
Ga (ppm)	16	16	18	19
Cu (ppm)	2	6	5	2
Zn (ppm)	27	27	116	37
Pb (ppm)	23	20	54	22
La (ppm)	23	48	56	47
Ce (ppm)	55	90	110	74
Th (ppm)	30	21	24	30
Nd (ppm)	14	32	38	36
U (ppm)	5	3	5	5

*LOI=Loss on ignition

Table 2. Trace-element compositions* of BCT, AST, Fanney Rhyolite (FR), Davis Canyon Tuff (DCT), and the Shelley Peak Tuff (SPT) measured by ICP-MS.

Sample #	MO-02	MO-03	180-SP-2	12-RE-1	12-RE-2
Unit	BCT	BCT	BCT	BCT	BCT
La	55.66	40.08	31.05	34.77	36.15
Ce	126.72	91.76	69.37	86.30	83.49
Pr	16.11	12.32	7.60	11.04	10.46
Nd	60.89	47.08	24.21	41.79	37.93
Sm	14.37	12.36	5.81	12.05	9.89
Eu	1.10	0.71	0.25	0.50	0.45
Gd	13.34	12.28	6.12	12.51	10.50
Tb	2.40	2.33	1.29	2.47	2.08
Dy	15.02	14.96	9.30	16.16	13.91
Ho	3.07	2.99	2.12	3.41	2.98
Er	8.38	8.09	6.78	9.55	8.62
Tm	1.22	1.18	1.13	1.41	1.32
Yb	7.33	6.95	7.74	8.66	8.41
Lu	1.10	1.02	1.30	1.30	1.32
Ba	343	206	54	52	58
Th	22.63	19.53	36.76	28.98	31.01
Nb	25.54	21.61	34.21	29.51	31.32
Y	78.53	78.83	63.92	90.50	81.08
Hf	9.89	7.55	8.73	8.85	8.76
Ta	1.81	1.60	2.46	2.22	2.28
U	3.80	3.07	6.11	5.81	6.87
Pb	12.13	13.68	42.14	25.79	22.63
Rb	272.4	188.3	291.6	238.1	253.5
Cs	17.25	9.17	3.45	3.37	4.23
Sr	106	117	32	20	19
Sc	3.8	2.2	3.8	3.1	3.1
Zr	319	220	188	223	215

*All measurements presented in ppm.

Table 2 continued

Sample #	MO-05	MO-06	MO-31	180-SP-1	APA-1	APA-2
Unit	AST	FR	FR	SPT	SPT	DCT
La	31.82	34.99	22.68	48.15	54.86	44.72
Ce	61.61	67.87	54.20	91.43	108.31	73.73
Pr	6.69	6.67	4.53	9.83	12.12	11.48
Nd	22.72	20.21	13.53	33.04	41.34	37.85
Sm	4.14	3.90	2.76	6.05	7.62	8.60
Eu	0.66	0.22	0.15	1.08	0.96	0.41
Gd	3.43	3.47	2.55	5.16	6.37	7.52
Tb	0.58	0.70	0.54	0.89	1.11	1.46
Dy	3.61	4.74	3.91	5.42	6.81	9.45
Ho	0.77	1.06	0.93	1.17	1.41	1.86
Er	2.20	3.26	3.00	3.38	4.08	5.11
Tm	0.35	0.55	0.52	0.54	0.63	0.80
Yb	2.34	3.67	3.69	3.50	4.04	5.22
Lu	0.37	0.59	0.62	0.57	0.65	0.77
Ba	414	79	98	618	625	46
Th	14.58	25.88	29.98	22.32	24.15	30.03
Nb	11.68	19.31	21.95	16.50	19.49	25.89
Y	20.75	31.39	26.01	32.01	37.81	44.51
Hf	4.94	5.96	6.69	7.05	8.31	6.40
Ta	0.83	1.47	1.65	1.16	1.47	1.90
U	2.98	3.82	4.75	3.82	5.23	5.53
Pb	11.43	17.51	22.20	19.51	52.95	19.58
Rb	198.9	507.3	312.5	170.6	189.7	210.6
Cs	6.07	11.68	12.15	3.60	3.69	3.37
Sr	268	56	70	185	139	13
Sc	2.4	2.0	2.0	4.1	3.8	4.3
Zr	175	149	166	240	287	152

Table 3. Radiogenic isotope ratios for three samples of the Bloodgood Canyon Tuff.

Sample #	180-SP-2	12-RE-1	12-RE-5b
$^{87}Sr/^{86}Sr$	0.718746	0.725120	0.727142
Error	0.000014	0.000012	0.000011
$^{87}Sr/^{86}Sr_i$	0.708222	0.711396	0.71993407*
$^{143}Nd/^{144}Nd$	0.512280	0.512288	0.512286
Error	0.000005	0.000005	0.000005
$^{143}Nd/^{144}Nd_i$	0.512253	0.512256	0.51225282*
$^{206}Pb/^{204}Pb$	18.749	18.740	18.769
Error	0.001	0.001	0.001
$^{207}Pb/^{204}Pb$	15.582	15.591	15.581
Error	0.001	0.001	0.001
$^{208}Pb/^{204}Pb$	38.868	38.883	38.911
Error	0.002	0.002	0.002

*$^{87}Sr/^{86}Sr_i$ for 12-RE-5b estimated based on 40 ppm Sr and 250 ppm Nd. $^{143}Nd/^{144}Nd_i$ for 12RE-5b estimated based on 40 ppm Nd and 10 ppm Sm.

Table 4. Petrologic Modeling Constraints from Figure 13, Model A.

Parents	La (ppm)	Yb (ppm)	k_D Yb	k_D La	F	R
APA-2[1]	44.72[1]	5.22[1]	0.04[3]	0.81[3]	0.019	0.9
05BM-174[2]	9[2]	3[2]				

[1]Rentz et al. (2016) [2]Amato et al. (2011) [3]Bulk partition coefficient from Bacon and Druitt (1988), Leeman and Phelps (1981), Schnetzler and Philpotts (1970), and Mahood and Hildreth (1983).

Table 5. Petrologic Modeling Constraints from Figure 13, Model B.

Parents	CaO (wt%)	SiO_2 (wt%)	Nd (ppm)	La (ppm)	F
180-SP-2	0.31	75.40	24.21	31.05	0.068
MO-03	0.09	80.14	47.08	40.08	

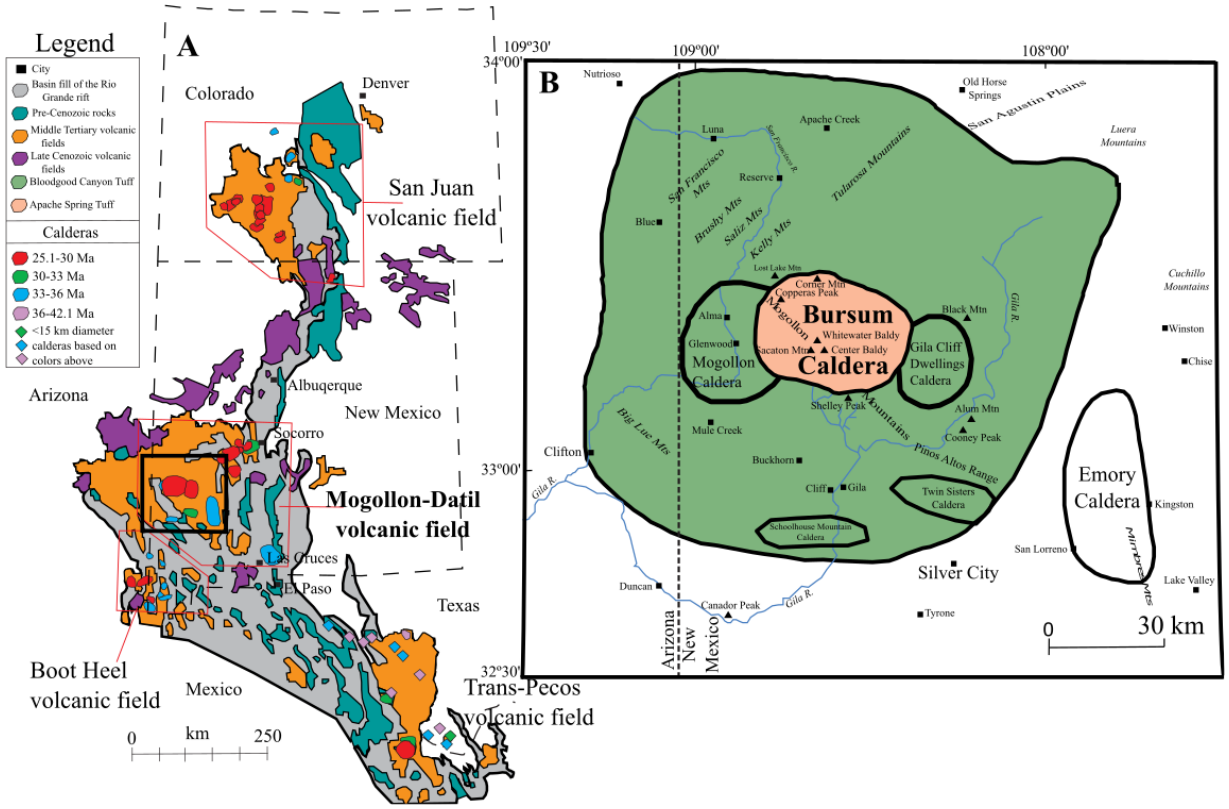

Figure 1. (A) Regional map showing calderas and Cenozoic volcanic fields within the Rio Grande rift. Major volcanic fields highlighted in red and field area (B) highlighted with a black box. Modified from Michelfelder and McMillan (2012) and Chapin et al. (2004). (B) Regional map showing calderas and the extent of the Bloodgood Canyon Tuff and Apache Spring Tuff. Modified from Ratté et al. (1984).

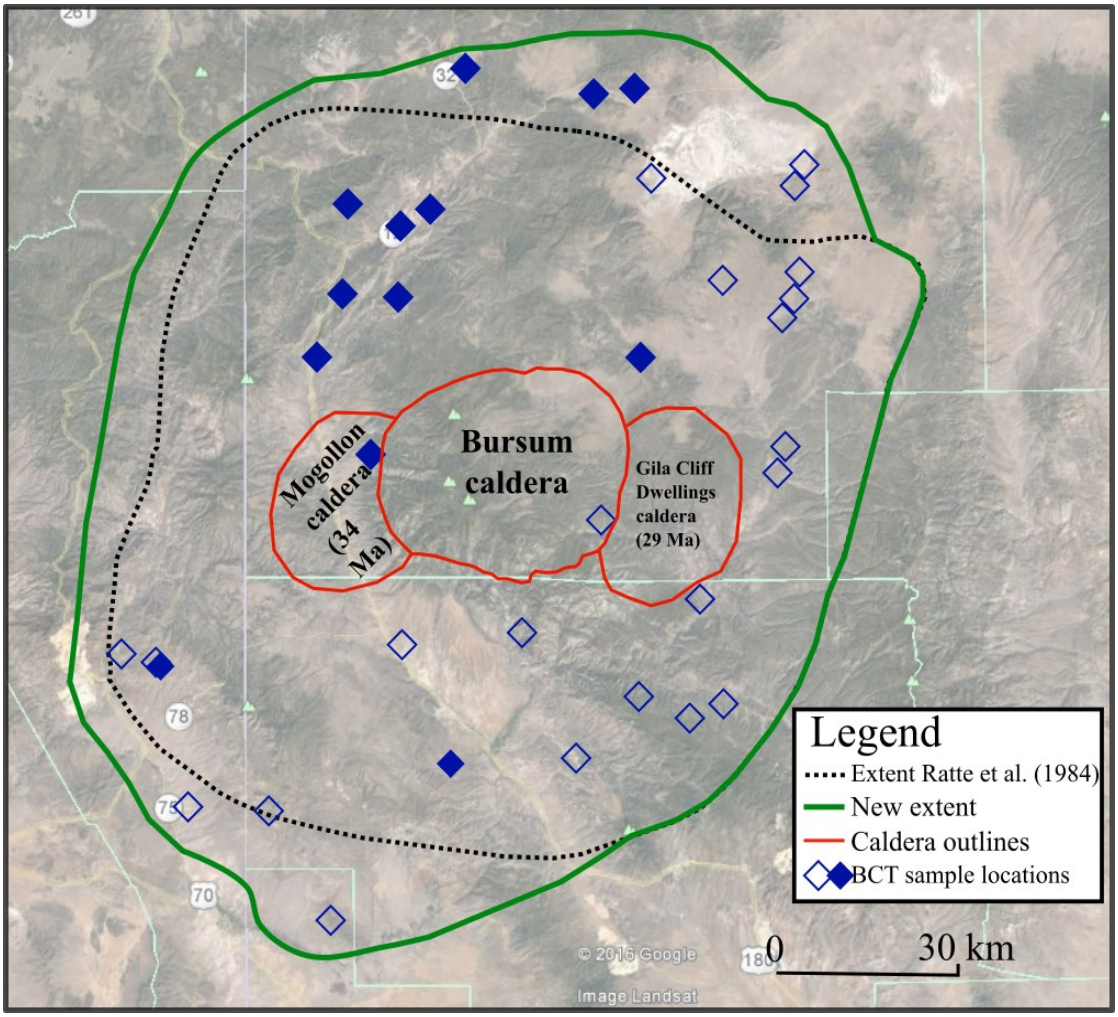

Figure 2. Extent map of Bloodgood Canyon Tuff overlain on a Google Earth image. Caldera outlines modified from Ratté et al. (1984) and McIntosh et al. (1992). New extent modified from McIntosh et al. (1992). Filled sample location points are samples collected in this study; hollow sample location points were presented in McIntosh et al. (1992).

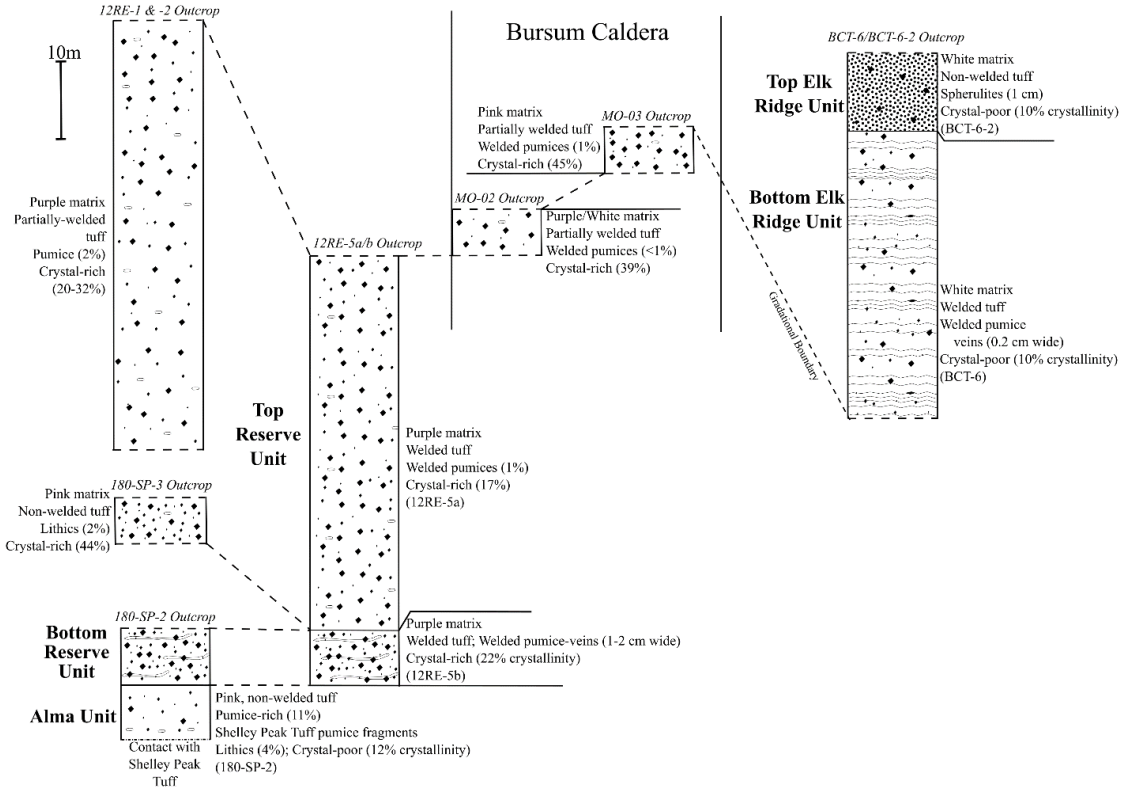

Figure 3. Stratigraphic section of the Bloodgood Canyon Tuff. Sections from selected outcrops on the west (left), within (center), and north (right) of the Bursum caldera depict petrography of the BCT in the selected outcrop.

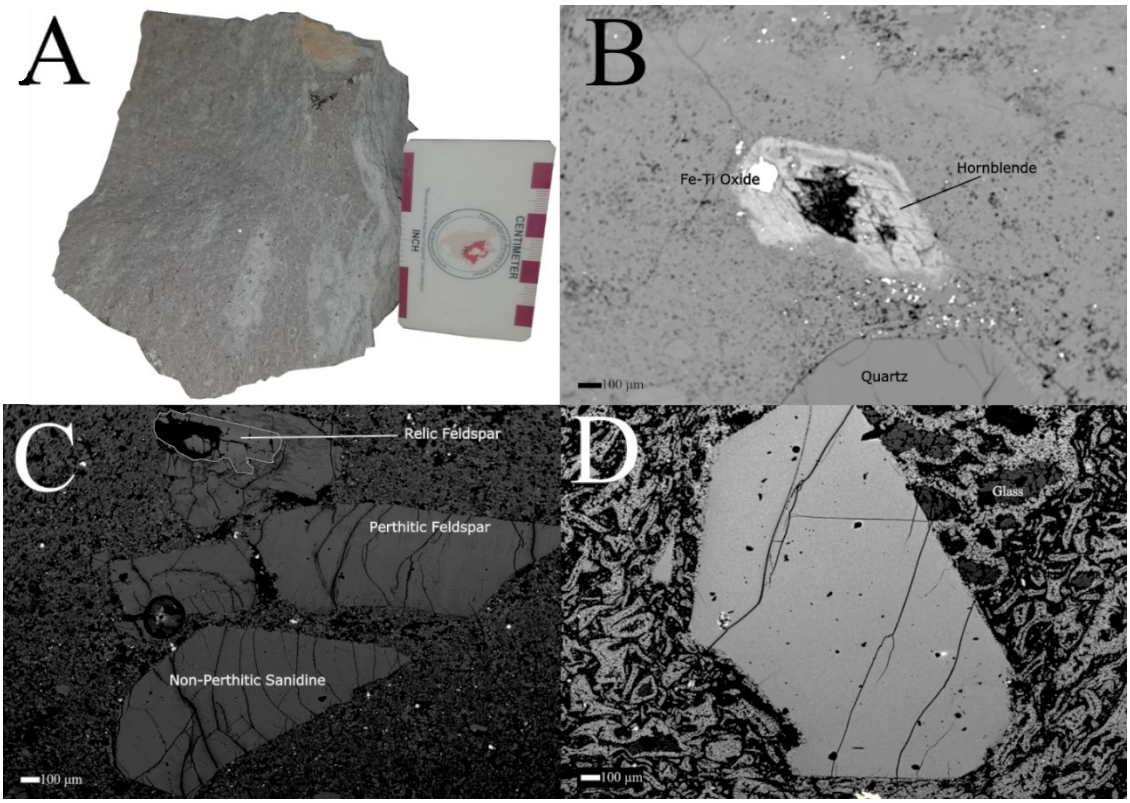

Figure 4. (a) Whole-rock photo of a sample from the middle of the stratigraphic section. Long pumice veins are present in the rock. (b) EMP image of a hornblende from the middle of the stratigraphic section. (c) EMP image of four sanidine phenocrysts from the middle of the stratigraphic section. Many sanidines in this sample have perthite textures. (d) Sanidine phenocryst from the top of the stratigraphic section. There is no obvious compositional zoning in feldspar phenocrysts from the BCT save for the perthitic textures.

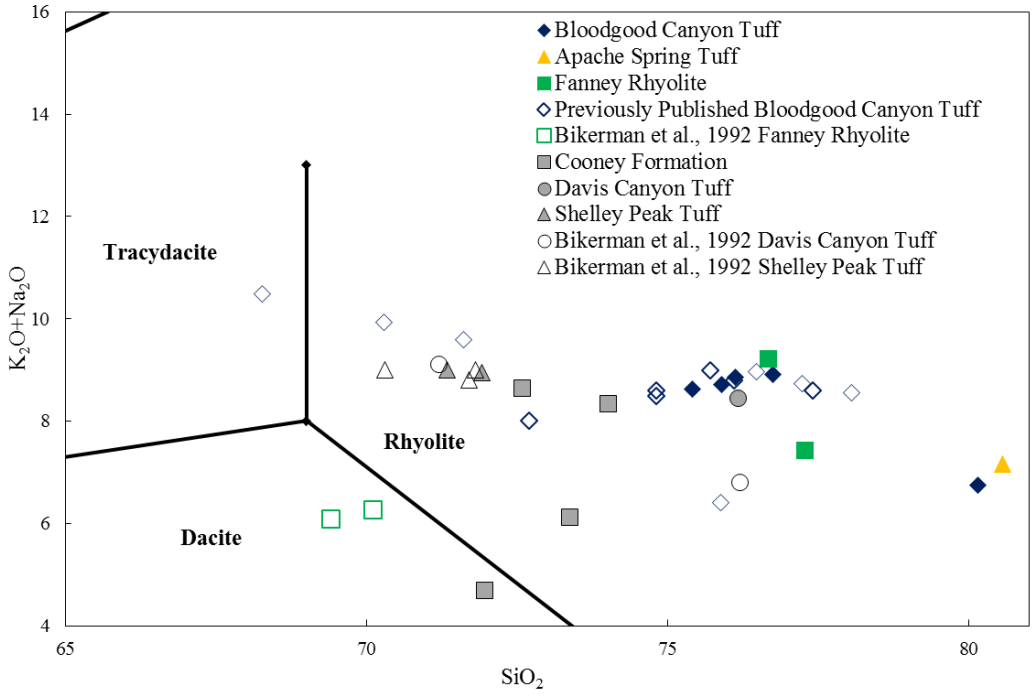

Figure 5. Total-Alkali vs Silica diagram for the Bursum Ignimbrite Complex (fields from La Maitre et al., 2002). All values are in wt %. Open symbols represent data from Bikerman et al. (1992) and Ratté et al. (1994). Gray symbols points represent units erupted from nearby calderas (Rentz et al., 2016).

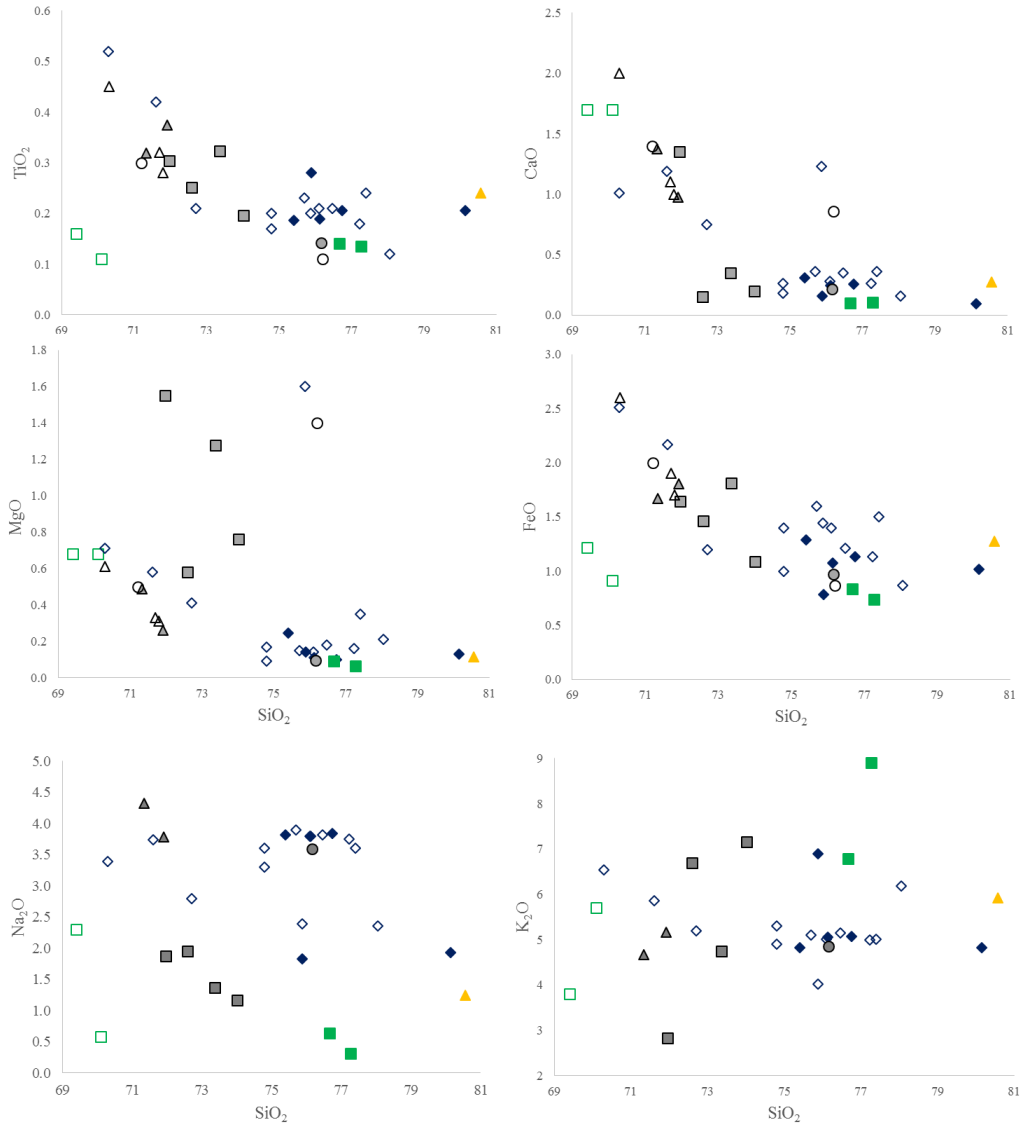

Figure 6. Major-Element Harker diagrams for the Bursum Ignimbrite Complex. All values are in wt %. Field definitions are as in Figure 5.

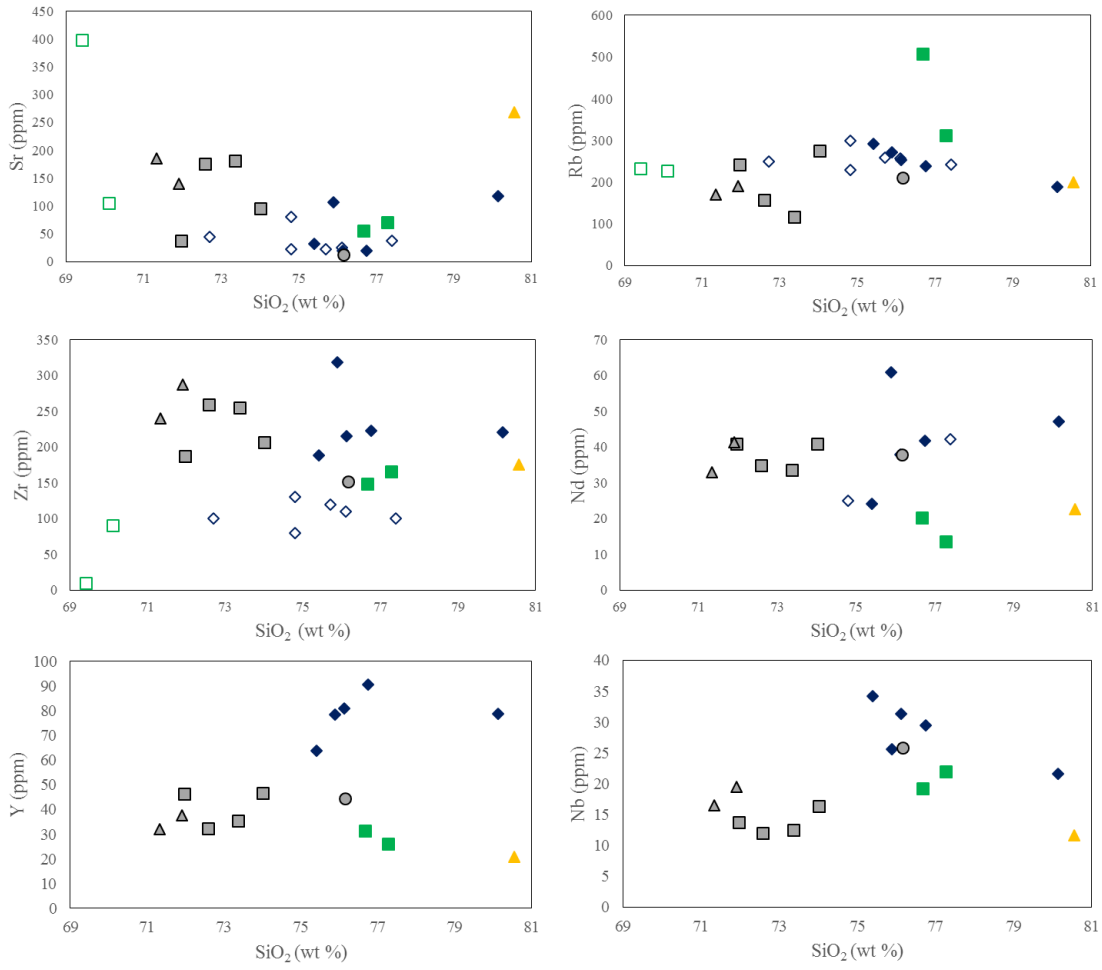

Figure 7. Trace-element Harker diagrams for the Bursum Ignimbrite Complex. Field definitions are as in Figure 5.

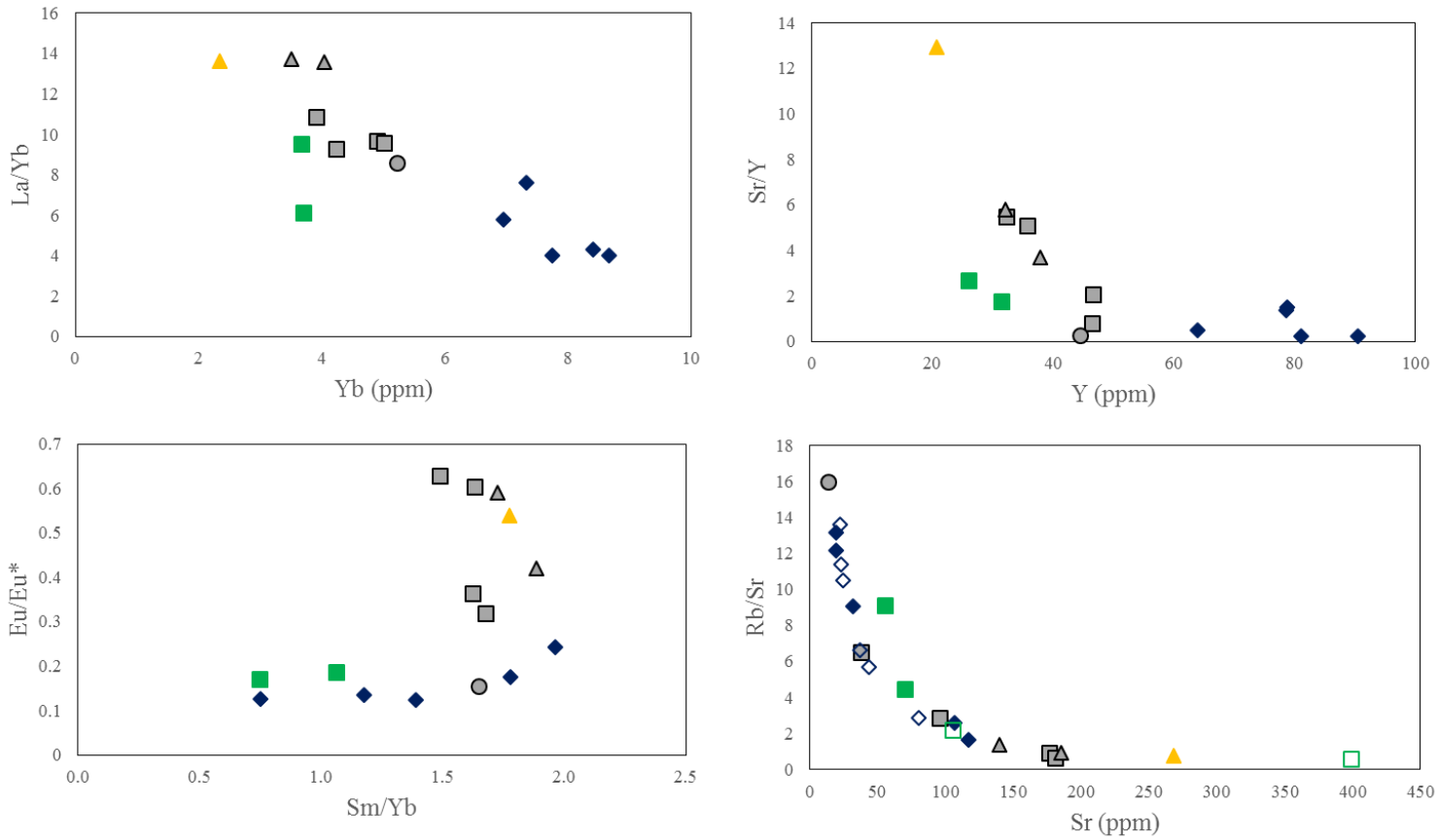

Figure 8. Bivariant trace element plots for the Bursum Ignimbrite Complex. Field definitions are as in Fig. 5.

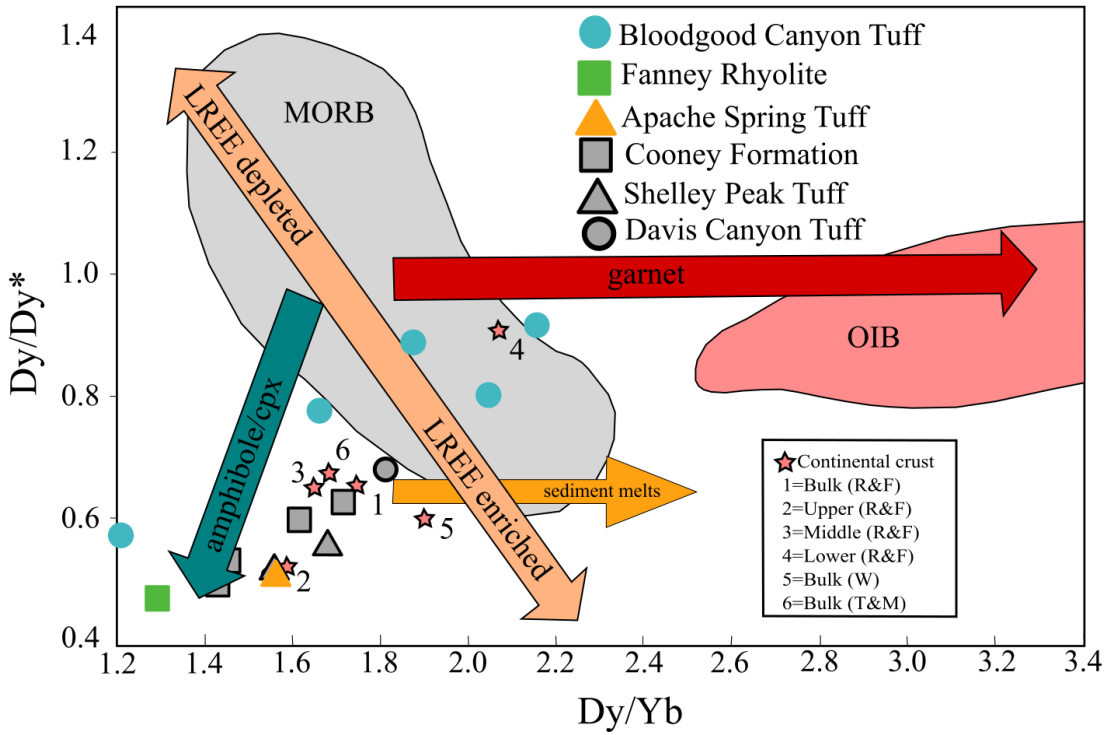

Figure 9. Plot of Dy/Dy* vs. Dy/Yb comparing the Bursum Ignimbrite Complex. Fields from Davidson et al. (2013). Continental crust estimates from Rudnick and Fountain (R&F; 1995), Wedepohl (W; 1995), and Taylor and McLennan (1985). Data for the Cooney, Davis Canyon, and Shelley Peak tuffs from Rentz et al. (2016).

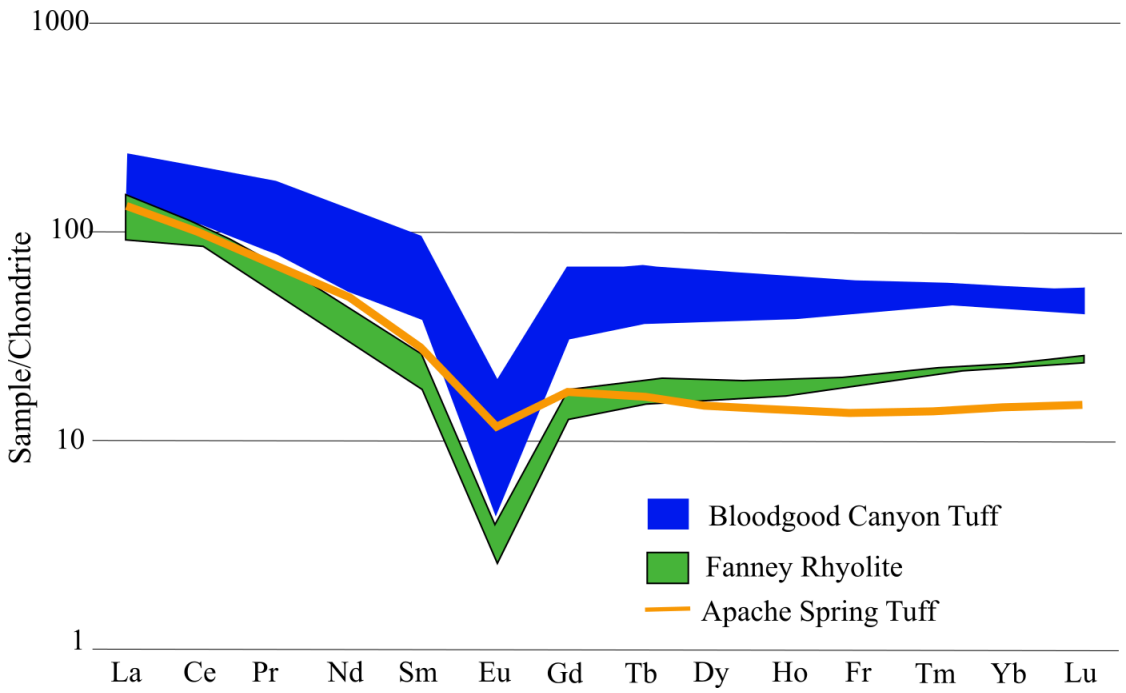

Figure 10. Log diagram of rare-earth elements in order of atomic number. Samples normalized to data from Wasson (1985).

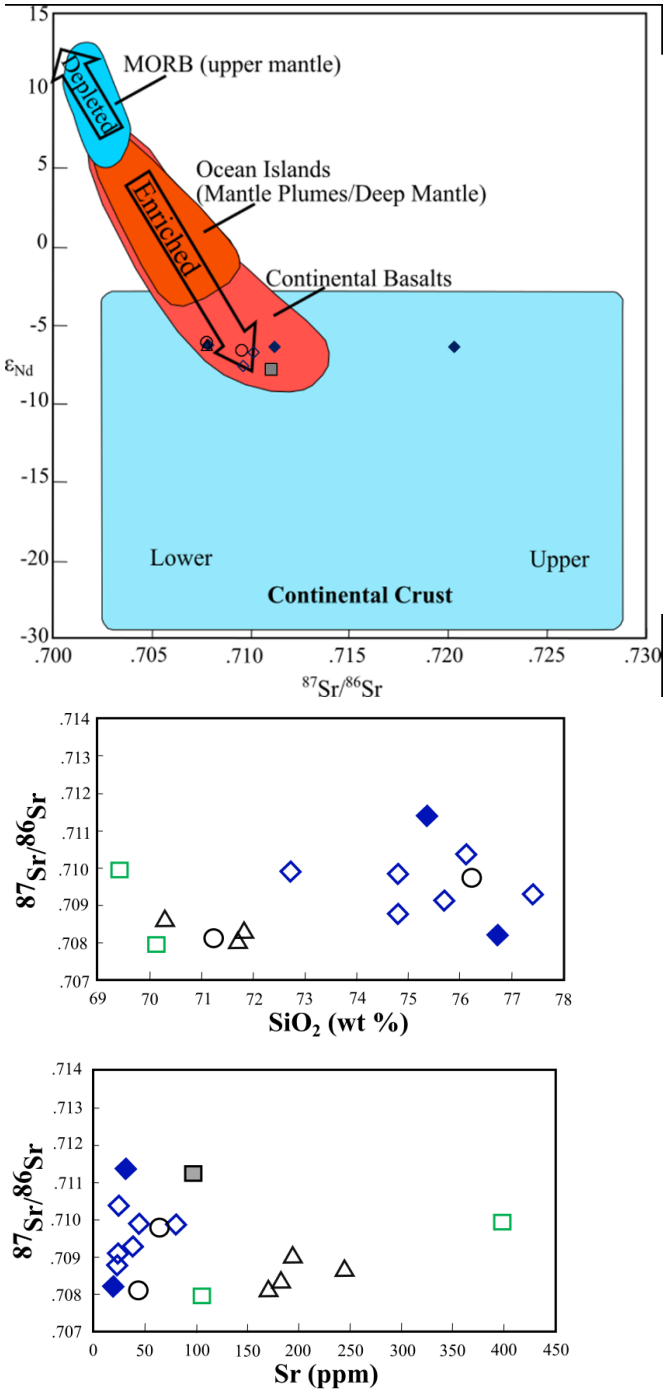

Figure 11. $^{87}Sr/^{86}Sr$ vs. εNd, SiO_2 (wt %), and Sr (ppm) for the Bursum Ignimbrite Complex. Open points represent data by Bikerman et al. (1992). Cooney Formation data from Rentz et al. (2016). Fields from DePaolo (1981b).

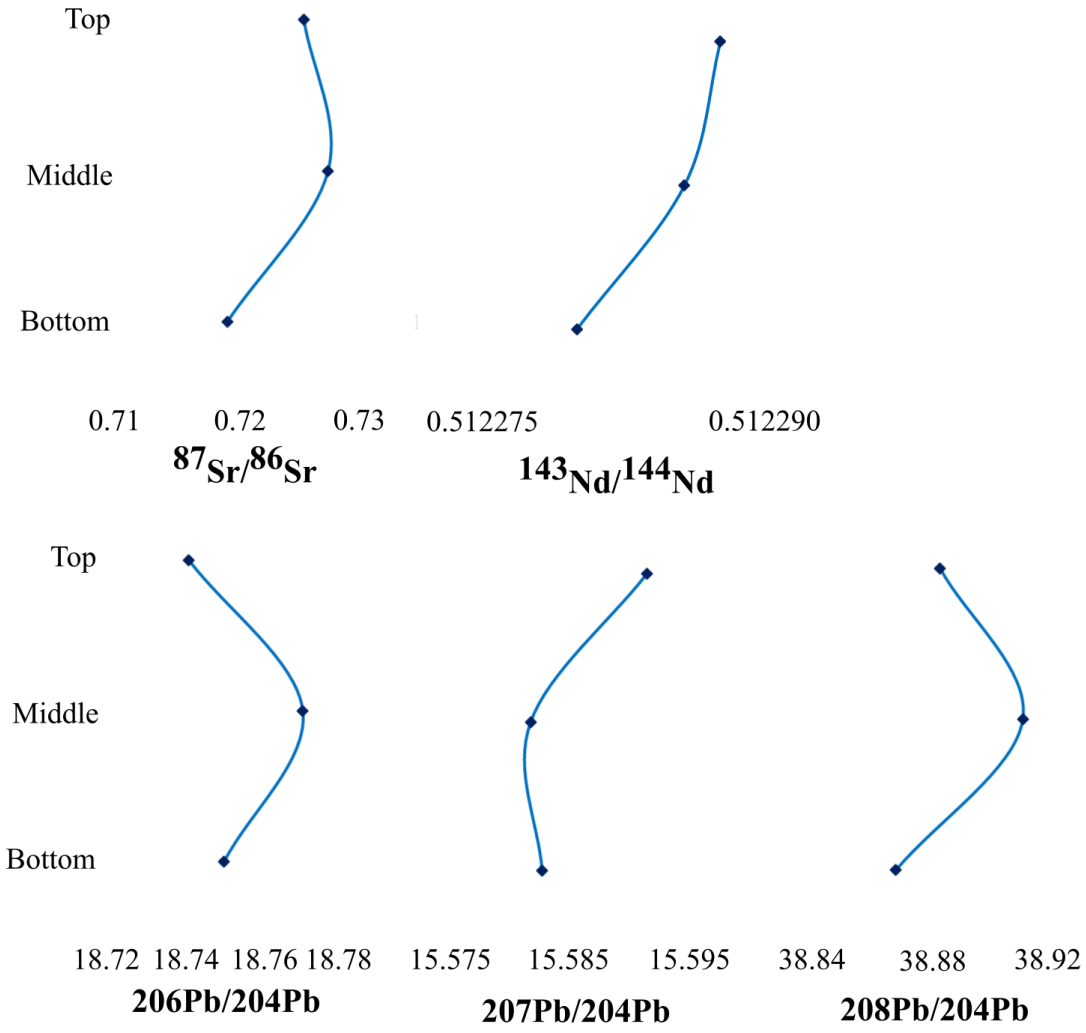

Figure 12. Radiogenic isotope ratios for three samples from the Bloodgood Canyon Tuff, in order of their position in the stratigraphic column.

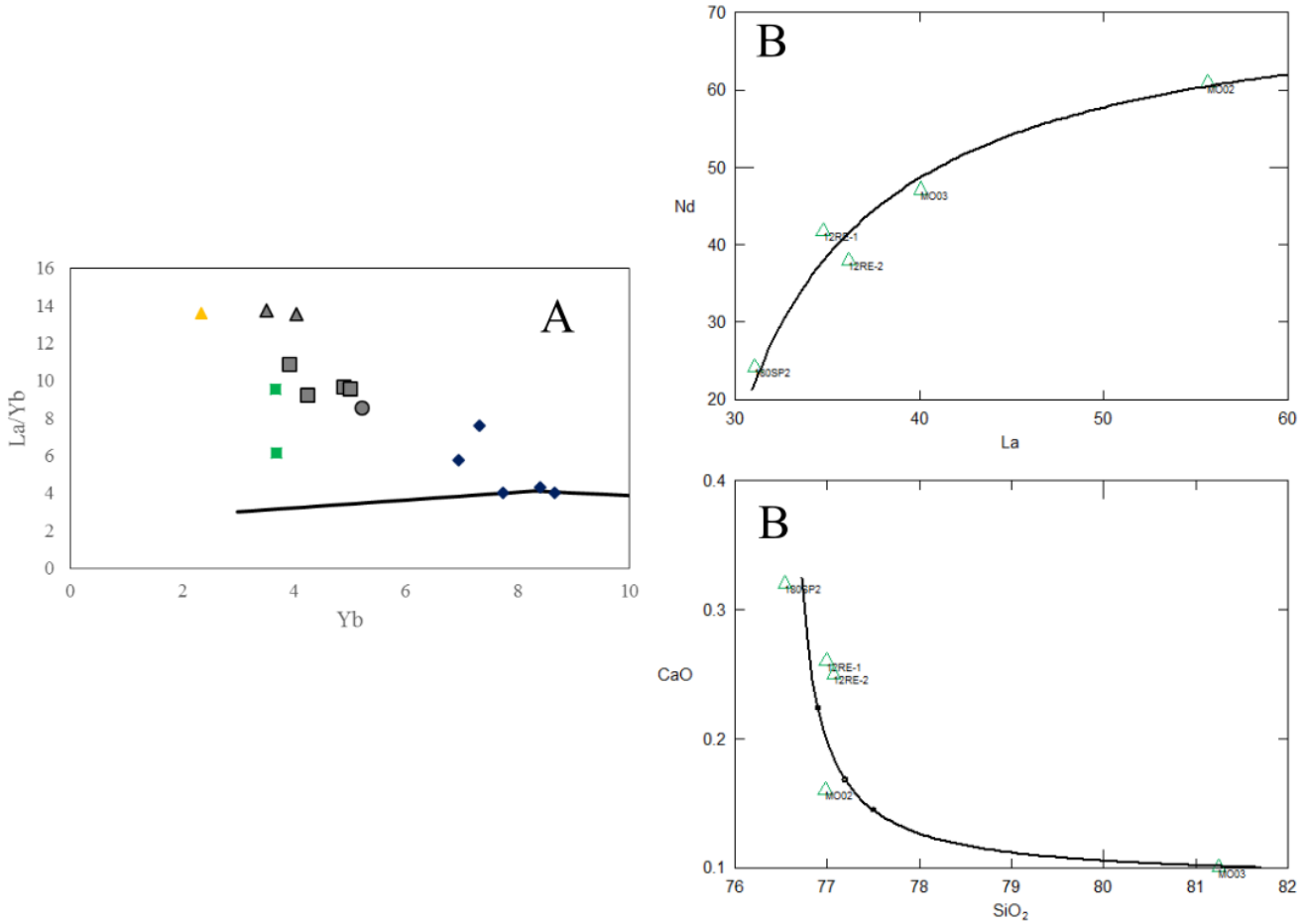

Figure 13. **(a)** AFC model of Davis Canyon Tuff and an amphibolite (Amato et al., 2011). This model, when mass balanced, only forms the bottom of the BCT section when 1.9% of 15BM-174 assimilated. Field Definitions are as in Figure 5. **(b)** Mixing model for the top (MO-03 and MO-02) and the bottom (180-SP-2) of the section using least squares mixing models. This mass-balanced model forms the middle of the BCT (12RE-1 and 12RE-2) with 6.8% of MO-03 mixed. Specific parameters in Table 4 and Table 5.

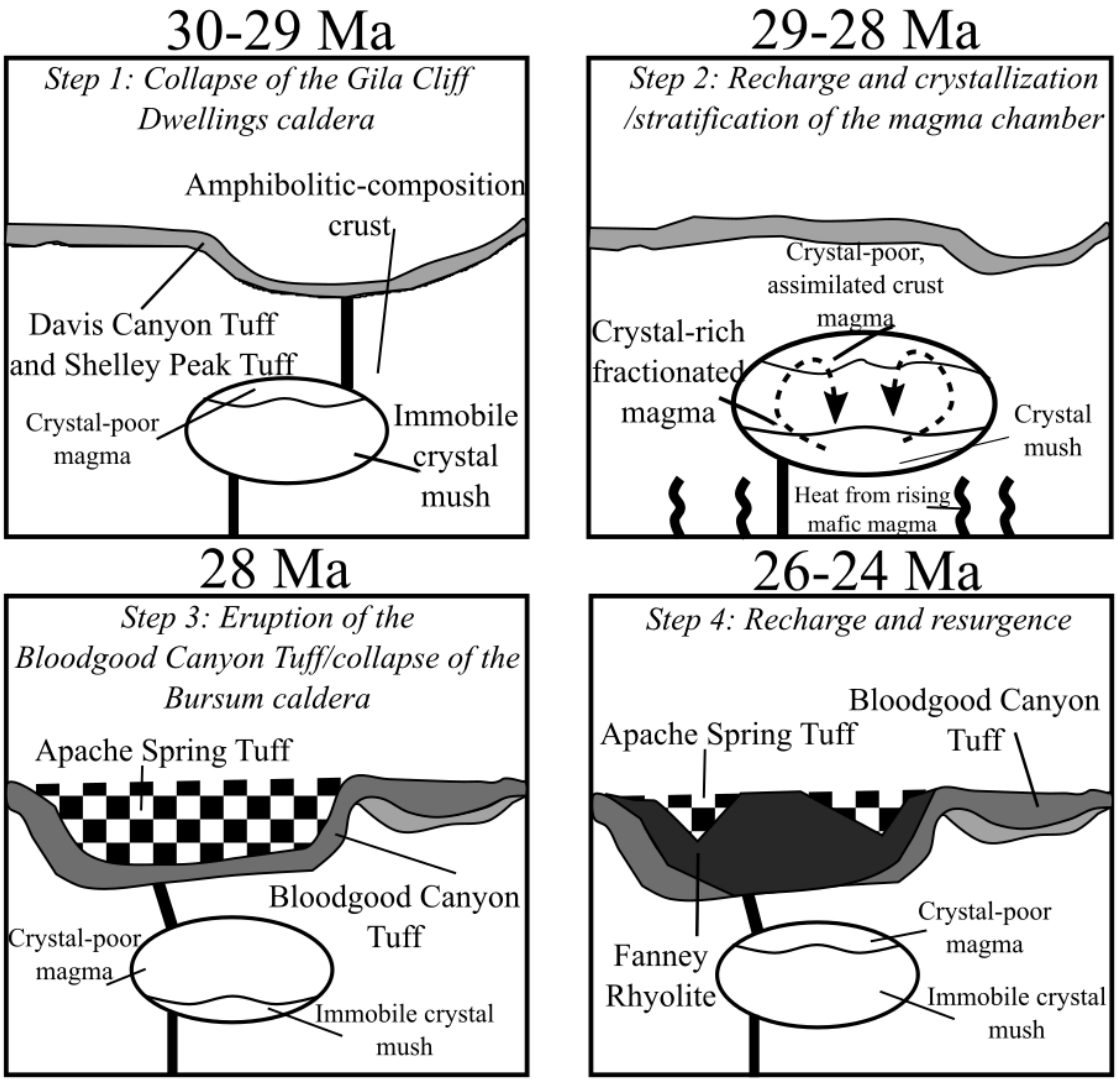

Figure 14. Evolution diagram for the BCT, AST, and Fanney Rhyolite. Not to scale.

EVOLUTION OF THE BLOODGOOD CANYON TUFF, WESTERN MOGOLLON-DATIL VOLCANIC FIELD, NEW MEXICO: EVIDENCE FROM MINERAL CHEMISTRY AND CSD ANALYSIS

Introduction

Large-volume ignimbrites present a unique perspective for magma accumulation in the crust. Two competing models for ignimbrite-building have been proposed: short-lived accumulations that erupt the entire chamber (Glazner et al. 2004) or incrementally built plutonic bodies that erupt large-volume ignimbrites (De Silva et al. 2006; Lipman 2007). In this study, I examine a large-volume ignimbrite in the central Mogollon-Datil volcanic field to determine whether large-volume volcanism was a result of short-lived accumulations or a long-lived erupting plutonic body.

Evidence for remobilized crystal mushes are present in many large-volume ignimbrites and volcanic systems around the world (e.g. Lassen Volcanic Center, Klemetti and Clynne 2014; Yellowstone Caldera, Upper Basin Member, Girard and Stix 2009; Ongatiti Ignimbrite, New Zealand, Cooper and Wilson 2014). A series of higher-temperature intrusions at the base of crystal mushes can provide enough heat to initiate mixing and mobilize a once-rigid skeleton of crystals (Huber et al. 2010; Bergantz et al. 2015; Schleicher et al. 2016). Remobilized crystal mushes extract eruptible melt from compositionally mature magmatic systems, erupting either crystal-rich compositionally unzoned dacites (monotonous intermediates) or crystal-poor zoned rhyolites (Bachmann and Bergantz 2004; Huber et al. 2012). However, individual magmatic systems can erupt different products based on local geology, ongoing tectonics, evolution of the system, and

composition (Bachmann and Bergantz 2004; Huber et al. 2010; Huber et al. 2012; Allan et al. 2013; Michelfelder et al. 2013; Cooper and Wilson 2014).

The "mush model" has been increasingly proposed as the source of crystal-poor and crystal-rich ignimbrites (Bachmann and Bergantz 2004; Hildreth 2004; Hildreth and Wilson 2007; Girard and Stix 2009; Huber et al. 2009; Bégué et al. 2014; Cooper and Kent 2014; Cooper 2017). Many crystal mushes are remobilized by incoming higher-temperature recharge, and whether eruption occurs before homogenization occurs is one of the driving mechanisms determining whether ignimbrites will be crystal-poor or crystal-rich (Huber et al. 2012). Mush remobilization can occur at the local scale, erupting crystal-poor ignimbrites, or activate batholith-sized reservoirs, erupting highly voluminous, crystal-rich ignimbrites (Bachman et al. 2002; Huber et al. 2010; Bachmann and Huber 2016). Mushes extract in multiple batches of magma reactivated by tectonic processes such as rifting, creating isolated patches of eruptible magma that do not mix and are triggered by depressurization instead of new magma input (Bégué et al. 2014). The variety of behaviors that magma chambers can exhibit presents a problem for unraveling the history of volcanic systems, because there is no one-size-fits-all model (Bachmann and Huber 2016). However, minerals hold the key to piecing together individual magma histories, through diffusion modeling, residence times, geochemistry, petrography, and other methods to track the evolution of individual magma batches (Wolff and Ramos 2014; Cooper 2017).

The whole-rock petrology and geochemistry of large-volume ignimbrites represent the surface expression of these processes and can be used to understand the development of the system. Numerous ash-flow tuffs are present in the Oligocene

Mogollon-Datil volcanic field (MDVF) in southern New Mexico. One of the largest is known as the Bloodgood Canyon Tuff (BCT; Ratté et al. 1984). The BCT was included in regional studies in the 1980s and 1990s, but no simple model was proposed to account for the complexity of the tuff (Ratté et al. 1984; Bikerman et al. 1992; Bikerman 1994) and its relationship to other ignimbrites in the MDVF. In this paper, I present mineral chemistry and geothermobarometry data from sanidine and hornblende phenocrysts from various points in the stratigraphic section of the BCT and combine these data with whole rock major- and trace-element and radiogenic isotope data to explain the complexity of the BCT. Based on this data, I suggest a two-step model for the BCT based on recent models of magma storage: continuous mobilization of a batholith-sized crystal mush to an upper reservoir and subsequent destabilization of that reservoir.

Geologic Background

The Mogollon-Datil volcanic field (MDVF; 45-24 Ma) is a manifestation of the Laramide volcanic arc situated 500 km from the trench of the subducting Farallon plate and the overriding North American plate. Bimodal magmatism was initiated by upwelling mantle material after the Farallon plate "rolled back" underneath the North American plate (Davis and Hawkesworth 1993; 1994; McMillan et al. 2000). The MDVF covers an area of 40,000 km^2 and erupted over 12,000 km^3 of high-K, calc-alkaline, basalt and rhyolite, large-volume ignimbrites and small-volume lava flows and domes (Elston et al. 1970; Davis and Hawkesworth 1994). From 45-36 Ma volcanism was characterized by the Kneeling Nun Tuff and Belltop Formation. The peak of volcanism occurred from 36-24 Ma when the Farallon slab rolled-back and initiated extension in the Rio Grande rift,

Basin and Range, and the Transition Zone. The large influx of material as a result of crustal relaxation and rollback initiated an ignimbrite flare-up and bimodal volcanism in the MDVF (Chapin et al. 2004; McMillan 2004). During the peak of the flare-up (28.9-27.4 Ma), greater than 6000 km^3 of rhyolite magma erupted from eleven regional ignimbrites (Chapin et al. 2004; McIntosh et al. 1992). As the ignimbrite flare-up was waning, volcanism occurred less frequently and shifted from high-silica rhyolites to andesite lava flows. Over time volcanism began to resemble mantle-derived material as the Rio Grande rift continued to thin the crust (McMillan et al. 2000).

The Bursum Ignimbrite Complex. The Bursum Ignimbrite Complex is a series of ignimbrites erupted from a group of nested calderas (the Mogollon, Gila Cliff Dwellings, and Bursum calderas) in the western MDVF during the peak of volcanism (Ratté et al. 1984; Elston 1984; Salings et al. in review). Ignimbrites and volcanic rocks erupted from these calderas range from calc-alkaline dacites to high-silica rhyolites (Ratté et al. 1984; Bikerman et al. 1992; Chapin et al. 2004; Davis and Hawkesworth 1994). The oldest erupted product in the Bursum Ignimbrite Complex is the Cooney Formation (34-32 Ma; Ratté et al. 1984), a series of tuffs sourced from the Mogollon caldera with interbedded volcaniclastic sediments and basalt lava flows (Rentz et al. 2016). The Cooney Formation erupted soon after the initiation of the ignimbrite flare-up (Ratté et al. 1984; McIntosh et al. 1992).

The Shelley Peak and Davis Canyon tuffs (29.01-28.1 Ma; McIntosh et al. 1992), suggested to be sourced from the Gila Cliff Dwellings caldera, are both found stratigraphically below the Bloodgood Canyon Tuff, but are chemically and petrographically distinct. The Shelley Peak Tuff (28.1 Ma; McIntosh et al. 1992) is

younger than the Davis Canyon Tuff (29.01 Ma; McIntosh et al. 1992) but the presence of clinopyroxene and plagioclase and lack of sanidines distinguishes it from other ignimbrites in the area.

The Bloodgood Canyon Tuff (BCT; 28 Ma; McIntosh et al. 1992) is sourced from the largest and youngest of the nested calderas, the Bursum caldera. The largest volume ignimbrite in the area, the BCT (1300 km^3; Salings et al. 2016) is a high-silica rhyolite outflow sheet with compositional zoning in relation to gray and brown pumice modal percent (Ratté et al. 1984; Elston 1984). Generally, the SiO_2 content increases up the stratigraphic section, from low-silica rhyolite and trachydacite to high-silica rhyolites (Bikerman et al. 1992; Ratté et al. 1994; Salings et al. 2016) with the silica positively correlated with an increase in modal percent of white-gray pumices. LREEs are enriched relative to HREE and all samples have pronounced Eu anomalies (Salings et al. 2016). Crystallinity varies between moderately crystalline (12%) to highly crystalline (up to 44% in some samples; Salings et al. 2016). Most if not all glass has been devitrified. Mineral phases include mainly sanidine and quartz, with various concentrations of biotite, hornblende, Fe-Ti oxides, titanite, apatite, and zircon (Ratté et al. 1984; Elston 1984; Salings et al. 2016; Salings et al. in review).

The stratigraphy of the Bloodgood Canyon Tuff (BCT) is reviewed in Salings et al (in review) and summarized in figure 1. The base of the BCT is characterized by the enrichment of lithics and pumice fragments and generally lack of phenocrysts. The base, in contact with the Shelley Peak Tuff, is an unwelded ash-flow that contains the lowest $^{87}Sr/^{86}Sr$ ratios and lowest SiO_2 content of the rest of the section (Bikerman 1989; Bikerman et al. 1992; Salings et al. 2016). The middle of the BCT is welded and is

characterized by large flattened pumices and a high crystallinity. Large (>1 mm) phenocrysts of quartz and sanidine dominate this part of the section. The top of the exposed BCT section is crystal-rich and welded, but is depleted in pumice fragments compared to the rest of the section.

The Apache Spring Tuff (27.9 Ma; McIntosh et al. 1992) is also thought to be sourced from the Bursum caldera (Ratté et al. 1984), but whole-rock geochemistry presented in Salings et al (in review) suggests it is not related to the BCT. The Apache Spring Tuff has been suggested to be intracaldera fill of the Bursum caldera and is mostly exposed as a breccia on the edges of the caldera (Ratté et al. 1984). The final unit of the Bursum Ignimbrite Complex is the Fanney Rhyolite, a series of intrusions, lava flows, and small-volume tuffs that makes up the resurgent phase of the Bursum caldera (Ratté et al. 1984; Salings et al. in review). The Fanney Rhyolite is geochemically very distinct from the BCT, but mineral phases and location suggest the two units are sourced from the same caldera (Ratté et al. 1984; Salings et al. in review).

Other Regional Ignimbrites. There are two other ignimbrites in the region that can be mistaken for the BCT due to their similar crystallinity, chemical composition, and mineral phases: the tuff of Triangle C Ranch and the Fall Canyon Tuff (Ratté 1981; Ratté et al. 1984; 1994; McIntosh et al. 1990; 1992). The Fall Canyon Tuff (29.4 Ma; Ratté 1981), found on the margin of the Bursum caldera, is petrographically similar to the BCT, but is interlaid with sandstone and contains more sodic plagioclase and clinopyroxene than the BCT (Ratté 1981). The tuff of Triangle C Ranch (28.0 Ma; McIntosh et al. 1992) is a high-silica tuff believed to have erupted from the Bursum Caldera but is only mapped north of the caldera rim (Ratté et al. 1994). Based on

paleomagnetic data, the tuff of Triangle C Ranch erupted at least 5000 years after the BCT (McIntosh et al. 1992). It is petrographically indistinguishable from the BCT but locally separated from the BCT by a volcaniclastic sandstone (McIntosh et al. 1990; Ratté et al. 1994).

Methods

Electron Microprobe. Electron microprobe (EMPA) data for K-feldspar and hornblende grains from three different samples of the BCT and plagioclase grains for one sample of the Cooney Formation were obtained using a JEOL JXA-8230 at the University of Iowa. Phenocrysts and groundmass phases were analyzed in carbon coated standard (30 μm) polished thin sections. BSE images were acquired using a beam set at 15 kV and 20 nA. Spot analyses (5 μm) of ~25 Feldspar grains per BCT sample and line transects of 8 K-feldspars in the BCT were collected, and 12 albite grains in the Cooney Formation were analyzed; Si, Al, Na, K, Ca, Fe, Ti, Pb, Ba, and Sr were analyzed and normalized to the Astimex Orthoclase standard for Feldspar grains. Cores and/or rims were analyzed for most feldspars, but grains with perthite textures were analyzed for composition differences between perthite sections with either spot analyses or line transects. Spot analyses (5 μm) of 3-6 hornblende grains per sample were analyzed for Si, Al, Mg, K, Na, Ca, K, Cr, Mn, and Ti and normalized to the UI #1 K-Hornblende and UI #1 A-Hornblende standards. Major elements were run for 15 seconds, and trace elements were run for 30 seconds, and detection limits are ~50 ppm. Energy-Dispersive X-Ray Spectroscopy (EDS) maps of Si, Al, K, Na, Ca, Fe, Mg, Ti, Ba, Cr, Dy, F, Mn, Ni, P, Pb, S, Th, V, Y, Zr, and Cl were collected for whole thin sections of each sample.

Crystal Size Distributions. Crystal size distributions were determined using Si EDS maps for all three BCT samples, K EDS maps for two samples, and a Na EDS map for one BCT sample analyzed by EMPA. Si EDS maps represented quartz and K or Na maps represented alkali feldspars. A Na EDS map was used for sample 12RE5b CSD analyses because the high K content in welded pumices in the sample made it difficult to digitally separate pumice from phenocrysts. *ImageJ v6.0* was used to convert EDS maps into binary images and to outline phenocrysts and remove quartz and sanidine grains embedded in the thin section glass. Resolution issues with grains <0.25 μm made it difficult to analyze, so these grains were excluded from final measurements, and hence CSD results are unable to measure syn-ascent crystallization (Witter et al. 2016). Particles were analyzed in *ImageJ v6.0*, exported into a CSD file using the *CSDCorrections* plugin, and run through the *CSDCorrections v1.53* program (Higgins 2000). The *CSDCorrections* program was used to account for the intersection probability effect and made partial corrections for the cut section effect when using 2D surfaces (Higgins 2000). The fabric for all CSD calculations was assumed to be massive due to lack of flow banding or foliation, and vesicles were 0% due to the welded nature of the samples. The "Roundness of grains" factor was set to 0.2 (where 1=ellipsoid and 0=block) based on visual inspection for both quartz and alkali feldspar in all samples due to the high population of euhedral grains that are partially resorbed. Size bins that had correction factors >1 were thrown out, usually at the ≤0.158 mm size bin, and bins with less than 5 grains were not included in the final CSD curves. *CSDSlice* (Morgan and Jerram 2006) was used to obtain accurate 3D dimensions of crystal shapes in each sample for alkali feldspars and quartz to input into the *CSDCorrections* program. Alkali feldspars

were tabular in shape (samples 180-SP-2 1:1.25:1.6; 12RE5b 1:1:1.3; 12RE5a 1:1:2.6), while quartz represented rectangular prisms (samples 180-SP-2 1:1:1.5; 12RE5b 1:1.15:1.3; 12RE5a 1:1.5:2.7). All quartz and alkali feldspar crystals were analyzed along the Ellipse Major axis.

Results

Whole-Rock Petrography. Bloodgood Canyon Tuff. The Bloodgood Canyon Tuff (BCT) is a rhyolitic ash-flow sheet; modal percentages of BCT samples are illustrated in Figure 2 and presented in Table 1. Alkali feldspar is the most dominant mineral phase in the BCT (9-28 modal %), followed by quartz (1-4% of total crystals), and accessory phases of titanite, Fe-Ti oxides, biotite, and trace hornblende, apatite, and zircon. Pumice is present as large (~1 cm) fragments in the base of the BCT, as fiamme (~1 cm wide) in the middle of the stratigraphic section, and as welded fragments at the top of the stratigraphic section (Salings et al. in review). Pumice exhibits two different textures and appearances: brown pumice that are relatively low-silica (68-70%), high-Mg and white pumice that contain high-silica (78%; Ratté et al. 1994). Brown pumice contain euhedral clinopyroxene and hornblende phenocrysts while white pumice contain euhedral to subhedral sanidines. Lithic fragments are only common in the base of the BCT, where they commonly occur as fragments of more mafic material similar to the Shelley Peak Tuff.

Three representative samples of the stratigraphic section were chosen for an in-depth mineral grain analysis of the BCT. Sample 180-SP-2 is a partially welded ash-flow tuff collected from the outcrop in contact with the Shelley Peak Tuff and best represents

the base of the BCT (Fig. 1). It contains ~15% lithic and pumice fragments (1 cm) from both unknown sources and the Shelley Peak Tuff. Phenocrysts make up 12% of the sample, and consist of alkali feldspar, quartz, hornblende, biotite, Fe-Ti oxides, and titanite (Fig. 2). Sample 12RE5b is a welded ash-flow tuff collected from an outcrop near Reserve, NM (Fig. 1). Petrographically, 12RE5b is similar to the rocks at the top of the 180-SP-2 outcrop, suggesting they are stratigraphically equivalent. The middle of the stratigraphic section is defined as the welded zone due to flattened pumices. Crystallinity is significantly higher in this section of the BCT; phenocrysts make up 22% of the sample, and consists mainly of large (>1 mm) alkali feldspars and quartz (Fig. 2). Other phases include biotite, Fe-Ti oxides, hornblende, and titanite (Fig. 2). Sample 12RE5a is a welded ash-flow tuff that was collected from the same outcrop as sample 12RE5b, but collected stratigraphically above it. Sample 12RE5a contains the same mineral phases as 12RE5b, but pumices are not flattened. This petrographic change represents a change from the middle of the stratigraphic section to the top of the stratigraphic section of the BCT. Phenocrysts and pumice make up 17% (Fig. 2) and 6% of sample 12RE5a, respectively. Plagioclase is not present in any of the BCT samples, with the exception of one inclusion found in 12RE5b, therefore "feldspar" will refer to alkali feldspars in the context of the BCT.

Cooney Formation. Sample MO-09 is a low-silica rhyolite collected from the Bursum caldera margin that contains abundant sodic plagioclase and biotite. Plagioclases are present as euhedral to subhedral, extremely sieved grains. Plagioclase grains are seriate, ranging from 500-3000 μm. Biotite grains are present as euhedral to subhedral, slightly altered grains. Resorption is present in some biotite while other grains are altered

by Fe-Ti oxides. Biotite grains are generally <500 μm. There is no visible K-feldspar, hornblende, or titanite in sample MO-09, as seen in the BCT.

Mineral Phases of the Bloodgood Canyon Tuff. Alkali Feldspar. Alkali feldspars in all three samples are optically unzoned and unsieved, but some grains have "plucked" areas, and relatively few grains display twinning. Most grains contain some degree of resorption, but no new growth zones are observed. Crypto-perthite textures are observed under BSE images, but perthite is not observed in reflected or transmitted light, or cathodluminescence (Fig. 3). Melt inclusions are common in alkali feldspars, but there are few mineral inclusions other than Fe-Ti oxides. Feldspar grains are fractured, and sizes are seriate, ranging from <100 μm to >2000 μm.

Feldspars are classified into 4 populations based on texture. These populations of feldspar grains include: Class 1 feldspars are anhedral and perthitic, Class 2 feldspars are anhedral and non-perthitic, Class 3 feldspars are euhedral and perthitic, and Class 4 feldspars are euhedral and non-perthitic. In large (>1000 μm) phenocrysts, perthite textures are only seen on the edges of the grains. Some smaller phenocrysts (100-200 μm) show perthite textures through the entire crystal. There is no correlation between crystal size and class. Examples of Class 1 and Class 3 perthites are shown in Fig. 3 and examples of Class 2 and Class 4 non-perthites are shown in Fig. 4.

Quartz. Quartz is found dominantly as subhedral phenocrysts in all samples of the BCT. Larger phenocrysts (> 1000 μm) occur in the middle and top of the stratigraphic section, while the bottom of the section has lower modal % of quartz and generally smaller phenocrysts (≤1000 μm). Quartz phenocrysts are resorbed and fractured similar to the alkali feldspars, do not contain new growth zones in cathodluminescence imaging,

and smaller grains are generally more resorbed than larger phenocrysts. Quartz grains are seriate, ranging in size from 0.1 mm to 3 mm. Quartz grains in pumices from samples 180-SP-2 and 12RE5b are the same size as quartz grains in the matrix in their respective samples. No observable grains are found in pumices from 12RE5a.

Hornblende and Biotite. Hornblende is a trace mineral in the BCT that is often found significantly altered (Fig 5a-d). Hornblende grains in the groundmass are often altered euhedral grains and ~100 μm in length. Hornblende phenocrysts present in the Shelley Peak Tuff pumice and lithic fragments found in sample 180-SP-2 are mostly unaltered, euhedral, and ~500 μm in length. Biotite grains are euhedral to subhedral, and range from 100 μm-500 μm. Some biotite grains have reaction rims of Fe-Ti oxides or have Fe-Ti oxides inclusions. No biotite phenocrysts were observed in pumice grains.

Other Mineral Phases. Zircon, apatite, and titanite are present in trace amounts in certain sections of the BCT. Zircon was not observed in the base of the stratigraphic section. Zircon present in the middle and upper parts of the section are small (<100 μm), euhedral grains and present as an accessory phase. Small (<100 μm), euhedral apatite is present in 180-SP-2, but not seen significantly in other samples.

Titanite is present in all samples of the BCT, but in varying modal percentages. Titanite is an accessory phase (1%) in the base and middle of the stratigraphic section, but as a trace phase in the top of the section. Unaltered euhedral titanite grains range from 100 μm-500 μm. Altered titanites are anhedral, 200-300 μm and some are surrounded by reaction rims. Titanites in the middle of the section are generally larger than in other sections (~400-500 μm vs. 100-300 μm).

Mineral Chemistry. Feldspar phenocryst compositions are shown in Figure 6 and presented in Table 2 (Appendix A; B). All feldspar grains analyzed in sample MO-09 were albites, ranging from Ab_{97}-Ab_{99} (Fig. 6). However, the BCT sample feldspars vary more in composition than the Cooney Formation. All non-perthitic feldspar grains are sanidine composition (Or_{39}-Or_{63}), but some feldspars have anorthoclase-composition perthites (Or_{14}-Or_{25}). One labradorite grain was analyzed in 12RE5b, but is considered a xenocrystic inclusion in a sanidine. Sanidine phenocrysts in sample 180-SP-2 range from Or_{44}-Or_{63}, but most grains analyzed are ~Or_{50}. Sample 12RE5b contains many sanidine phenocrysts with perthitic textures, and as such feldspar compositions range from sanidine to anorthoclase (Or_{14}-Or_{52}). The single zoned labradorite is included inside perthite. Sample 12RE5a contains less perthitic sanidine phenocrysts than sample 12RE5b, and compositions range from Or_{36}-Or_{51}.

Major- and trace-element compositions for feldspars from each sample of the BCT are shown separated by textural class in Figure 7. Most trace elements are constrained to a 1000 ppm range, with the exception of outliers in Ba, Fe and Sr content, across all feldspar classes. Sr and Fe show no trends between classes, but Ba content ranges from 20-1420 ppm in Class 1, below detection limit-770 ppm in Class 2, below detection limit-1460 ppm in Class 3, and below detection limit to 980 ppm in Class 4. Pb content ranges from 40-650 ppm in Class 1, below detection limit to 580 ppm in Class 2, 50-450 ppm in Class 3, and 20-520 ppm in Class 4. Ti content ranges from below detection limit to 400 ppm in Class 1, below detection limit to 310 ppm in Class 2, 30-350 ppm in Class 3, and below detection limit to 350 ppm in Class 4.

There are three populations of phenocrysts in euhedral crystals based on Pb concentration (Class 2 and 4): low Pb (0-120 ppm), medium Pb (150-280 ppm), and high Pb (350-580 ppm) concentrations. Increasing Ti in 12RE5a shows a positive correlation with Pb. A negative correlation is observed between Ti and Pb content in sample 12RE5b. Sample 180-SP-2 phenocrysts with <200 ppm Ti increase in Pb as Ti approaches 200 ppm, but decrease again when Ti content is >200 ppm. Pb content decreases with increasing Fe content in samples 12RE5a and 12RE5b, but sample 180-SP-2 has three populations of phenocrysts that have different trends. High Pb samples (>400 ppm) and medium Pb (200-300) decrease in Pb as Fe content increases, but low Pb phenocrysts (<100 ppm) increase in Pb as Fe content increases. There is no correlation between minor and trace element concentration and % Or.

Line transects of % Or concentrations (Fig. 8) and Sr, Ba, and Pb concentrations (Fig. 9) were measured on selected sanidines in all three samples. Some points in the line transects were not included in the final data because the composition totals were ≤97% and were not statistically viable. Or % varies significantly in perthitic sanidines such as 12RE5b-2 (22-52 % Or), 12RE5b-4 (25-44 % Or), 12RE5b-19 (14-38 % Or), and Class 1 grain 180-SP-2-7 varies by 20% Or (44-63 % Or). Sanidines 180-SP-2-17, 180-SP-2-5, 12RE5a-16, and 12RE5a-24 vary by less than 10% Or. There is no systematic correlation between textural classes and minor and trace element concentrations. Sr varies by 400 ppm in all samples except the perthite 12RE5b-19, in which it increases by ~500 ppm from end to end. Trace elements within both perthitic and non-perthitic sanidines can vary significantly (Fig. 9). In larger grains (>1 mm) Sr, Ba, and Pb concentrations

increase and decrease in the line transect from core to rim. Generally, when Sr concentration increases, Ba concentration decreases.

Crystal Size Distributions. Crystal size distribution (CSD) curves, resulting from the measurement of the long axis of individual alkali feldspar and quartz crystals are compiled in Figure 10. Natural logarithm of crystal size density is plotted versus crystal length. The CSDs for all the samples range from -7 to 1 (logarithmic scale) and are inversely correlated to crystal length (Fig. 10) The CSD curves are non-linear and curves display a clear upward concave trend for all samples. The observed concave upward trend precludes the application of a single-crystal population model (Marsh 1988; Cashman and Marsh 1988; Higgins and Roberge 2003, 2007; Salisbury et al. 2008). Two to three distinct kinks appear for each mineral phase, with a steeper slope in smaller (<1 mm) grain sizes and a gentler slope in larger grain sizes. Samples 12RE5a and 12RE5b have larger phenocrysts than 180-SP-2, and as such their CSD curves extend out farther (Fig. 10). The population density for these larger size fractions are more variable than observed in the smaller fractions as illustrated by the variable logarithmic values in Figure 10.

The alkali feldspar CSD for sample 12RE5a starts with a sharp slope but the slope decreases after 0.5 mm while the CSD for 180-SP-2 starts with a negative correlation between crystal size and population density, and returning to a positive correlation with a relatively steep slope. The alkali feldspar CSD for 12RE5b is relatively log-linear (Q = 0.4). Quartz CSDs for all three samples show similar concave up patterns. Changes in slope occur at ~0.75 mm-1 mm and again at ~1.5 mm. Samples 180-SP-2 and 12RE5b have very similar trends in smaller crystal fractions while 12RE5a and 12RE5b have similar trends in larger quartz fractions.

Thermobarometry. Sanidine and hornblende grains were analyzed to determine thermobarometry for the system (Appendix C; D). Sanidines were compared with albite phenocrysts from MO-09 to find the temperature of the magma chamber using the Two Feldspar method (Putirka 2008). Temperatures ranged between 700ºC and 900ºC using this method. Oxygen isotope data collected by Hoffman and Michelfelder (2016) in quartz and plagioclase phenocrysts in the Shelley Peak Tuff yielded temperatures of ~750ºC, and it is reasonable to assume the BCT is approximately around the same temperature since the Shelley Peak Tuff is sourced from the same system and is of similar age. Pressures were obtained using the Al-in-hornblende method (Ague and Brandon 1996). Calculated pressures range from 0.66-0.96 GPa for grains with mol Al >1 and 0.10-0.33 GPa for grains with mol Al <1 (Fig. 5e). However, grains with mol Al <1 are altered, and the only unaltered grains with CaO >1 were found in lithic fragments or pumices and yielded pressures of >0.7 GPa.

Discussion

Minor and Trace Element Patterns. Major, minor, and trace element patterns within mineral grains can reveal crucial information about the evolution of a magmatic system (e.g. plagioclase zoning Ginibre and Wörner 2007; Ginibre et al. 2007; hornblende zoning Bachman and Dungan 2002; Allan et al. 2013). The intrusion of a different-composition magma (or lack thereof) will be reflected in mineral grains growing at the time, provided the elements don't diffuse out (Ginibre et al. 2007). Many hypothesized remobilized mush ignimbrites contain complex zoning and resorption within grains (e.g. Carpenter's Ridge Tuff; Bachman et al. 2014) as well as a whole-rock

composition change to lower SiO_2 contents with increased crystallinity (Huber et al. 2012).

There does not appear to be a systematic change in major or trace elements, across individual grains or between phenocrysts of different classes. Percent Orthoclase only significantly varies in anhedral perthites, so perthite texture does not indicate magma mixing with a significantly different composition magma. Ginibre and Wörner (2007) and Ginibre et al. (2007) suggest Fe and Sr concentrations within plagioclase can be used to track recharge events in the magma chamber. Fe and Sr concentrations in sanidines from the BCT do not vary significantly (except outliers) and suggests any recharge of significantly different composition magma was minimal or buffered by the magmatic system (Fig. 10). Line transects of individual grains display at most 400 ppm change in Sr. This change happens gradually across grains and does not seem to correlate with other grain analyzed (Fig. 9). The biggest changes happen in perthites, probably as a result of partition coefficient changes due to thermal disequilibrium (Ginibre and Wörner 2007). This suggests that there was not an intrusion of different composition magma in the chamber before eruption, and thermal disequilibrium occurred prior to eruption of the BCT.

Changes in slope in the CSD curves suggests multiple rejuvenation or mixing events (Brugger and Hammer 2010; Witter et al. 2016), but the absence of major- and trace-element zoning suggests that the recharge magma was either similar composition or buffered preventing new zoning and maintaining equilibrium (Bachmann and Bergantz 2008; Huber et al. 2009). If the system had been homogenous and undergone remobilization, new growth around crystals would have been observed (e.g. The Fish

Canyon Tuff; Bachman et al. 2002; Wotzlaw et al. 2013). Cooper and Wilson (2014) suggest that convective stirring after remobilization can homogenize the melt, providing a mechanism to create large phenocrysts and perthites from a crystal mush. This melt mixing with the eruptible top of the magma chamber, combined with incoming heat from a high-temperature mafic intrusion, creates a homogeneous extractable melt from the crystal mush. However, this model proposed by Cooper and Wilson (2014) for the crystals in the Ongatiti system display complex zoning, unlike phenocrysts from the BCT. Due to the absence of complex zoning, I suggest that the BCT itself may not have come directly from a remobilized crystal mush. Instead, remobilized magma migrated to a separate shallower reservoir and accumulated there. This migration left behind minerals from the remobilized mush (Kent et al. 2010) and quartz and alkali feldspar crystallized in the shallower reservoir that was in equilibrium, so no major composition changes were occurring. If quartz and alkali feldspar had crystallized in the mush and migrated with the magma, there would be evidence of compositional zoning (Cooper and Wilson 2014).

Xenocrystic Hornblendes. The pressures obtained from hornblendes in all three samples call into question the source of the hornblendes analyzed. Pressures >0.6 GPa correlate with lower crust depths, but the $^{143}Nd/^{144}Nd$ ratios of the BCT suggest a high degree of crustal contamination (0.512253-0.512256; Bikerman 1989; Bikerman et al. 1992; Salings et al. 2016). Grains that give pressures normally expected for an upper crustal magma chamber (~0.1-0.2 GPa; Bachmann et al. 2002) are significantly altered and have low mol Al contents, and are therefore unable to give reliable data. Modeling in Salings et al. (in review) suggests that the magma chamber was assimilating with an amphibolite-composition rock or hornblende-biotite granite (Amato et al. 2011),

therefore hornblendes found in the BCT may simply be of xenocrystic nature sourced from a wallrock contamination. However, hornblendes from brown pumices are unaltered as opposed to hornblendes in the BCT, but also gave pressures of >0.6 GPa (Fig. 5e). Therefore, if hornblende is a stable phase in the mush or a deeper reservoir cumulate below the BCT reservoir, they would reflect lower-crustal pressures.

Crystal Size Distributions. The concave up shape of the CSD curves in all samples for both quartz and alkali feldspars suggests that at least two populations of crystal sizes existed in the chamber during time of eruption (Brugger and Hammer 2010; Ngonge et al. 2013). Similar curve patterns for both crystal modes also provides evidence for the co-crystallization of sanidine and quartz. The steep slope in smaller crystal size fractions and gentle slope in larger crystal size fractions and resorption and crypto-perthite textures suggests Ostwald ripening, where a population of smaller grains are being resorbed in favor of larger grains during chamber destabilization (Shea et al. 2009). The absence of a linear trend, representing fractional crystallization (Marsh 1988), agrees with the mixing model developed in Salings et al. (in review). In this model, the Davis Canyon Tuff assimilated with wallrock to create the base of the stratigraphic section of the BCT.

The CSD curves for the base of the BCT (sample 180-SP-2) show a larger population of smaller (<1 mm) grains, probably as a result of new nucleation due to assimilation and fractional crystallization, while larger grains are antecrysts from previous crystallization periods (Brugger and Hammer 2010; Ngonge et al. 2013). The CSD curves for the middle of the BCT (sample 12RE5b) are close to linear for alkali feldspars, suggesting alkali feldspars were less influenced by intrusion in this section of

the chamber and continued to crystallize without many new nucleation events. Quartz CSD curves are less linear than alkali feldspar curves in all samples, suggesting quartz was more likely to initiate new nucleation events after new intrusions. CSD curves suggest multiple recharge events, but the lack of zoning in feldspars and quartz suggests the recharge magma was of similar composition or buffered.

An influx of heat to the magma chamber from the regional ignimbrite flare-up drove the system towards resorption of sanidines and quartz, and soon after the thermally unstable chamber erupted (Chapin et al. 2004; Degruyter et al. 2015). More evidence of thermal destabilization is the slight convex up pattern in CSD curves at >1 mm in sample 12RE5b, where most of the perthite textures are found. According to experimental data by Brugger and Hammer (2010), crystallization driven by decompression will force this trend.

Magmatic Processes in the Bloodgood Ignimbrite Complex. The K-feldspar and quartz grains in the BCT have populations of large (>1 mm) and small (~0.1mm) phenocrysts, but the mineral grain compositions do not vary much (Figs. 7 and 8). Lack of zoning and sieving in feldspar phenocrysts do not indicate a major mixing event, so there is evidence for a reservoir that was in equilibrium for a long time, as opposed to a remobilized mush, which would display complex zoning (Bachmann et al. 2002; Witter et al. 2016; Troch et al. 2017). Crystallinity varies within the stratigraphic section while mineral grain compositions and assemblages remain mostly constant, this may be a relic of syn-eruption processes.

Lack of zoning in sanidines suggests the magma reservoir was in equilibrium, and batches of extracted melt from the lower crustal pyroxene-plagioclase reservoir is

providing new similar-composition magma to grow the reservoir. If these batches are of similar composition, no significant composition changes will affect crystal growth patterns (Ginibre et al. 2007). Other regional studies for the MDVF have proposed a basaltic-andesite mush of batholith scale (Elston 2008; Chamberlin et al. 2002; Chamberlin 2015). The similarity of the Shelley Peak Tuff mineral phases to this proposed mush suggests that the Shelley Peak Tuff is derived directly from the mush while the BCT is derived from an extracted melt of the mush. Though the Shelley Peak Tuff and Davis Canyon Tuff both erupted from the Gila Cliff Dwellings caldera, the mineral assemblages for each tuff are vastly different (Ratté et al. 1984). The Davis Canyon Tuff is crystal-poor and contains quartz and sanidine of similar major-element composition as the BCT (McIntosh et al. 1990) while the Shelley Peak Tuff is crystal-rich and contains pyroxene and plagioclase (Ratté et al. 1984). It is probable that the Shelley Peak Tuff represented a time in the magmatic history where dike propagation off the cumulate caused eruption, usually of andesitic intrusions, but also of pyroxene-plagioclase-bearing rhyolites (Kent et al. 2010).

Magma Chamber Destabilization. Perthite textures are mostly present in the middle and top section of the BCT, indicating the whole section was not erupted at once, as perthite mostly represents sudden changes in magma chamber conditions (Yund 1984). A relic labradorite feldspar found in the middle of the section that has similar Sr concentrations as the Cooney Formation, but this is not enough evidence to suggest the Cooney Formation was an early magma reservoir of the BCT so more data needs to be collected to confirm this connection.

The lack of systematic variation in % Or within grains (Fig. 8) does not indicate a major composition change in the magma, but instead indicates a thermal destabilization of the magma chamber for a relatively short period before eruption. Some small (~100 μm) sanidines in the middle of the section are completely encased in perthite (Fig. 8f), and as such change the most in % Or, while larger grains (>1 mm) are only partially altered to perthite (Fig. 8d-e).

The sparsity of perthites in sample 180-SP-2 suggests that the magma chamber destabilized soon before the initial eruption and continued to be unstable after eruption of 180-SP-2, continuing to alter sanidines in the rest of the magma chamber, and another eruption soon afterward evacuated the remaining eruptible magma. CSD curves (Fig. 10) for both quartz and sanidines suggest thermal disequilibrium began to resorb smaller mineral grains in favor of larger grains before eruption of the BCT, but lack of recrystallization surfaces suggests there was not enough time to re-equilibrate and recrystallize. The BCT hence represents a window of time between destabilization and re-equilibration. Based on the timeline of the ignimbrite flare-up in the region (Chapin et al. 2004), I suggest that heat from an incoming basaltic/andesitic intrusion during the peak of the ignimbrite flare-up destabilized the magma chamber and caused eruption of the BCT. It is likely that without the amount of heat provided by the ignimbrite flare-up, the crystal mush would not have been thermally weakened enough to erupt so much material. Allan et al. (2013) suggests the rapid accumulation and extraction of Oruanui Ignimbrite eruption was driven by a continental rift, similar to rifting occurring near the MDVF at the time of eruption of the BCT, so this may also have played a factor in the large volume of eruptible melt (Chapin et al. 2004).

Relationships to Other Ignimbrites. Regional studies for the MDVF have proposed a basaltic-andesite mush of batholith scale feeding many of the large ignimbrite eruptions in the MDVF (Elston 2008; Chamberlin et al. 2002; Chamberlin 2015). Evidence for regional magmatic processes similar to the processes in the BCT is revealed in the similar lithology and chemistry of other ignimbrites (Fig. 11). Sanidine chemistry done by McIntosh et al. (1990) reveals that many ignimbrites erupted in the MDVF have sanidines with the same general composition as sanidines found in the BCT and many units also contain crypto-perthitic textures, including the Shelley Peak Tuff. The presence of plagioclase feldspar instead of sanidine in the Cooney Formation and other older tuffs in the MDVF, such as the Kneeling Nun and Rubio Peak (Chapin et al. 2004) suggests that early magmatism was dominated by reservoirs containing plagioclase feldspar, and over time these systems evolved to crystallize alkali feldspar instead of plagioclase.

Percent Or range from 43%-66% in ignimbrites in the region (McIntosh et al. 1990), but there remains no correlation between % Or and time, as sanidines with higher % Or than most BCT sanidines occur both before and after eruption of the BCT. Many other ignimbrites in the area could contain crypto-perthites for the same reason the BCT does: thermal disequilibrium in the magma chamber onset by the ongoing ignimbrite flare-up, and the absence of crypto-perthites in the Davis Canyon Tuff further supports the model that the BCT evolved from the Davis Canyon Tuff. The absence of crypto-perthites in the Apache Spring Tuff (McIntosh et al. 1990) suggests that, if the Apache Spring Tuff was erupted from the Bursum caldera, the magma chamber had re-equilibrated post-BCT eruption.

Evolution of the Bloodgood Canyon Tuff. I present an evolution diagram for the Bloodgood Canyon Tuff based on petrographic textures, CSDs, and mineral data (Fig. 12). Petrologic modeling (Salings et al. in review) and petrography suggests after the eruption of the Davis Canyon Tuff, the remaining magma assimilated with the surrounding hornblende-biotite granite/amphibolite-composition wallrock (Amato et al. 2011). The Davis Canyon Tuff magma was crystal-poor and was composed primarily of quartz and sanidine (Ratté 1981), but feeding this reservoir was extracted melt from a pyroxene-plagioclase cumulate. The lack of mafic phenocrysts in the Davis Canyon Tuff and BCT suggests that crystals from the cumulate do not travel into the reservoir because of crystal entrainment, and the few that may are unstable in the new reservoir, but the remaining reservoir is more highly evolved and so crystallizes sanidine and quartz after extraction (Ellis et al. 2014). The higher crystallinity of the BCT compared to the Davis Canyon Tuff suggests that after eruption of the Davis Canyon Tuff, the reservoir continues to crystallize sanidine and quartz. The presence of amphibole suggests the water content in the magma was high, and melt extraction was an easier process than it had previously been, as some units erupted before the BCT do not contain hornblende (Ratté 1981; Pistone et al. 2017; Huber et al. 2010).

After eruption of the Davis Canyon Tuff, heat from an increased influx of mantle material at the base of the pyroxene-plagioclase cumulate caused dike propagation off the cumulate. The mineral phases present in the Shelley Peak Tuff suggests that this unit is a manifestation of a dike which traveled through the crust and through the reservoir of extracted melt before erupting. This dike is able to pass through the magma reservoir without fully mixing because of temperature and rheology differences (Bergantz et al.

2015), but some sanidines from the reservoir were dragged up with the intrusion, leaving contaminated sanidines in the Shelley Peak Tuff (McIntosh et al. 1990). The heat caused by the intrusion of the Shelley Peak Tuff (~750ºC) into the reservoir caused thermal disequilibrium in the chamber, which had previously been sitting at <750°C (Hoffman and Michelfelder 2016).

The thermal disequilibrium caused previously unaltered sanidines and quartz to become resorbed and perthites began forming in the sanidines. Soon after the chamber became unstable, the first eruption of the BCT began, erupting the base of the unit. Continued thermal disequilibrium destabilizes the magma chamber, and crystals are still being resorbed while sanidines become increasingly perthitic. However, before the chamber can completely re-equilibrate, another eruption of the BCT forces the collapse of the Bursum caldera, releasing a large portion of the crystal mush in a Taupo-fashion caldera collapse (Allan et al. 2013).

Evidence for a continuous eruption is seen in distal deposits from the middle of the section to the top is also shown in the crystallinity of the middle of the section. During eruption, larger crystals tend to drop out first, causing a normal gradation of crystallinity (Willcock et al. 2015). Collapse of the Bursum caldera has been linked to the eruption of the BCT through previous studies (Ratté et al. 1984; Elston 1984), and the collapse after initial eruptions destabilized the magma chamber and block-faulting is also seen in large calderas (Ratté et al. 1984).

After eruption of the BCT, it is believed that the tuff of Triangle C Ranch erupted from the Bursum caldera. Soon afterwards, the Apache Spring Tuff began to fill in the subsiding Bursum caldera (Ratté et al. 1984), but whether this unit is actually sourced

from the Bursum caldera is unclear (Salings et al. in review). Two million years after, when the ignimbrite flare-up was waning, a lower-volatile magma devoid of hornblendes and pyroxenes erupted and made up the resurgent dome of the Bursum caldera.

Conclusion

The Bloodgood Canyon Tuff represents a large accumulation of magma by continuous intrusions of similar-composition magma extracted from a batholith-scale pyroxene-plagioclase cumulate in the lower crust. Though hornblende is present in the unit, degree of alteration and Al-in-Hornblende pressures suggest these phenocrysts are xenocrystic in nature or came from the remaining magma leftover from the Shelley Peak Tuff eruption. Sanidine phenocrysts suggest different crystallization periods, and three different populations of Pb concentrations. Since there is no complex zoning present it is unlikely that the BCT was remobilized from a crystal mush. Populations of perthite textures also suggest that thermal magma chamber destabilization from incoming high-temperature mafic magma initiated the initial eruption of the BCT, and soon afterward the rest of the chamber destabilized and initiated collapse of the Bursum caldera, ejecting much of the remaining eruptible magma.

References

Ague JJ, Brandon MT (1996) Regional tilt of the Mount Stuart batholith, Washington, determined using aluminum-in-hornblende barometry: Implications for northward translation of Baja British Columbia. Bull Geol Soc Am 108:471–488. doi: 10.1130/0016-7606(1996)108<0471:RTOTMS>2.3.CO;2.

Allan ASR, Morgan DJ, Wilson CJN, Millet MA (2013) From mush to eruption in centuries: Assembly of the super-sized Oruanui magma body. Contrib to Mineral Petrol 166:143–164. doi: 10.1007/s00410-013-0869-2

Amato JM, Heizler MT, Boullion AO, et al (2011) Syntectonic 1.46 Ga magmatism and rapid cooling of a gneiss dome in the southern Mazatzal Province: Burro Mountains, New Mexico. Geol Soc Am Bull 123:1720–1744. doi: 10.1130/B30337.1.

Bachmann O, Bergantz GW (2004) On the Origin of Crystal-poor Rhyolites: Extracted from Batholithic Crystal Mushes. J Petrol 45:1565–1582. doi: 10.1093/petrology/egh019

Bachmann O, Bergantz G (2008) The Magma Reservoirs That Feed Supereruptions. Elements 4:17–21. doi: 10.2113/GSELEMENTS.4.1.17

Bachmann O, Deering CD, Lipman PW, Plummer C (2014) Building zoned ignimbrites by recycling silicic cumulates : Insight from the 1,000 km^3 Carpenter Ridge Tuff, CO. Contrib to Mineral Petrol 167:0–13. doi: 10.1007/s00410-014-1025-3

Bachmann O, Dungan MA (2002) Temperature-induced Al-zoning in hornblendes of the Fish Canyon magma, Colorado. Am Mineral 87:1062–1076.

Bachmann O, Dungan MA, Lipman PW (2002) The Fish Canyon magma body, San Juan volcanic field, Colorado: Rejuvenation and eruption of an upper-crustal batholith. J Petrol 43:1469–1503. doi: 10.1093/petrology/43.8.1469

Bachmann O, Huber C (2016) Silicic magma reservoirs in the Earth's crust. Am Mineral 101:2377–2404. doi: 10.2138/am-2016-5675

Bégué F, Deering CD, Gravley DM, et al (2014) Extraction, storage and eruption of multiple isolated magma batches in the paired Mamaku and Ohakuri eruption,Taupo volcanic zone, New Zealand. J Petrol 55:1653–1684. doi: 10.1093/petrology/egu038

Bikerman M (1989) Rb, Sr, Rb-Sr, and isotopic Sr values for volcanic rocks from the southwestern part of the Mogollon-Datil volcanic field. New Mex Geol 11:76–83.

Bikerman M, Bell K, Card JW (1992) Strontium and neodymium isotopic study of the western Mogollon-Datil volcanic region, New Mexico, USA. Contrib to Mineral Petrol 109:459–470. doi: 10.1007/BF00306549

Bikerman M (1994) Are the western Mogollon-Datil mid-Cenozoic ash flows cogenetic? Pearce element ratios and isotopic aspects of the question. New Mex Geol Soc Guid Mogollon Slope, West-Central New Mex East Cent Arizona 187–192.

Brugger CR, Hammer JE (2010) Crystal size distribution analysis of plagioclase in experimentally decompressed hydrous rhyodacite magma. Earth Planet Sci Lett 300:246–254. doi: 10.1016/j.epsl.2010.09.046

Cashman, KV, Marsh, BD (1988) Crystal size distribution (CSD) in rocks and the kinetics and dynamics of crystallization II: Makaopuhi lava lake. Contr Mineral Petrol 99:5: 292-305. doi:10.1007/BF00375363

Chapin CE, Wilks M, Mcintosh WC (2004) Spacetime patterns of Late Cretaceous to present magmatism in New Mexico—comparison with Andean volcanism and potential for future volcanism. New Mex Bur Geol Miner Resour Bull 160:13–40.

Chamberlin RM (2015) Geochemical, mineralogical, textural and map data for crystal-rich, caldera facies Hells Mesa Tuff and a comagmatic lava dome, central New Mexico: with a note on compositional zoning. New Mexico Bureau of Geology and Mineral Resources Open File Report 568.

Chamberlin, RM, Chapin, CE, McIntosh, WC (2002) Westward migrating ignimbrite calderas and a large radiating mafic dike swarm of Oligocene age, central Rio Grande rift, New Mexico: surface expression of an upper mantle diapir? Geol Soc Am Abstracts with Programs 34:6: 438.

Cooper, KM (2017) What does a magma reservoir look like? The “Crystal’s-Eye” View. Elements 13:23-28. doi: 10.2113/gselements.13.1.23

Cooper KM, Kent AJR (2014) Rapid remobilization of magmatic crystals kept in cold storage. Nature 506:480–3. doi: 10.1038/nature12991

Cooper GF, Wilson CJN (2014) Development, mobilisation and eruption of a large crystal-rich rhyolite: The Ongatiti ignimbrite, New Zealand. Lithos 198–199:38–57. doi: 10.1016/j.lithos.2014.03.014

Davis J, Hawkesworth C (1993) The petrogenesis of 30-20 Ma basic and intermediate volcanics from the Mogollon-Datil Volcanic Field, New Mexico, USA. Contrib to Mineral Petrol 115:165–183. doi: 10.1007/BF00321218

Davis J, Hawkesworth C (1994) Early calc-alkaline magmatism in the Mogollon-Data Volcanic Field, New Mexico, USA. J Geol Soc London 151:825–843. doi: 10.1144/gsjgs.151.5.0825

De Silva SL, Gosnold WD (2007) Episodic construction of batholiths: Insights from the spatiotemporal development of an ignimbrite flare-up. J Volcanol Geotherm Res 167:320–335. doi: 10.1016/j.jvolgeores.2007.07.015

Elston WE, Coney PJ, Rhodes RC, et al (1970) Progress report on the Mogollon Plateau volcanic province, southwestern New Mexico: No.2. New Mex Geol Soc Guideb 21:75–86.

Elston WE (1984) Mid-Tertiary ash flow tuff cauldrons, southwestern New Mexico. J Geophys Res 89:8733. doi: 10.1029/JB089iB10p08733

Ginibre C, Wörner G (2007) Variable parent magmas and recharge regimes of the Parinacota magma system (N. Chile) revealed by Fe, Mg and Sr zoning in plagioclase. Lithos 98:118–140. doi: 10.1016/j.lithos.2007.03.004

Ginibre C, Wörner G, Kronz A (2007) Crystal Zoning as an Archive for Magma Evolution. Elements 3:261–266.

Girard G, Stix J (2009) Magma recharge and crystal mush rejuvenation associated with early post-collapse Upper Basin Member rhyolites, Yellowstone caldera, Wyoming. J Petrol 50:2095–2125. doi: 10.1093/petrology/egp070

Glazner AF, Bartley JM, Coleman DS, et al (2004) Are plutons assembled over millions of years by amalgamation from small magma chambers? GSA Today 14:4. doi: 10.1130/1052-5173(2004)014<0004:APAOMO>2.0.CO;2

Higgins MD (2000) Measurement of crystal size distributions. Am Mineral 85:1105–1116.

Higgins MD, Roberge J (2003) Crystal Size Distribution of Plagioclase and Amphibole from Soufriere Hills Volcano, Montserrat: Evidence for Dynamic Crystallization-Textural Coarsening Cycles. J Petrol 44:1401–1411. doi: 10.1093/petrology/44.8.1401

Higgins MD, Roberge J (2007) Three magmatic components in the 1973 eruption of Eldfell volcano, Iceland: Evidence from plagioclase crystal size distribution (CSD) and geochemistry. J Volcanol Geotherm Res, 161:3: 247-260.

Hildreth W (2004) Volcanological perspectives on Long Valley, Mammoth Mountain, and Mono Craters: Several contiguous but discrete systems. J Volcanol Geotherm Res 136:169–198. doi: 10.1016/j.jvolgeores.2004.05.019

Hildreth W, Wilson CJN (2007) Compositional zoning of the bishop tuff. J Petrol 48:951–999. doi: 10.1093/petrology/egm007

Hoffman and Michelfelder (2016) Oxygen Isotope and Geochemical analysis of volcanic

rocks from south-central New Mexico: Insight on crustal contamination and magmatic evolution. Geol Soc Am Abstracts with Programs 48:7.

Huber C, Bachmann O, Manga M (2009) Homogenization processes in silicic magma chambers by stirring and mushification (latent heat buffering). Earth Planet Sci Lett 283:38–47. doi: 10.1016/j.epsl.2009.03.029

Huber C, Bachmann O, Manga M (2010) Two competing effects of volatiles on heat transfer in crystal-rich magmas: Thermal insulation vs defrosting. J Petrol 51:847–867. doi: 10.1093/petrology/egq003

Huber C, Bachmann O, Dufek J (2012) Crystal-poor versus crystal-rich ignimbrites: A competition between stirring and reactivation. Geology 40:115–118. doi: 10.1130/G32425.1

Kent AJR, Darr C, Koleszar AM, et al (2010) Preferential eruption of andesitic magmas through recharge filtering. Nat Geosci 3:631–636. doi: 10.1038/ngeo924

Klemetti EW, Clynne MA (2014) Localized Rejuvenation of a Crystal Mush Recorded in Zircon Temporal and Compositional Variation at the Lassen Volcanic Center, Northern California. PLoS ONE 9:12: e113157. doi: 10.1371/journal.pone.0113157

Marsh, BD (1988) Crystal size distribution (CSD) in rocks and the kinetics and dynamics of crystallization. Contr Mineral Petrol 99:3: 277-291. doi:10.1007/BF0037536

McIntosh WC, Sutter JF, Chapin CE, Kedzie LL (1990) High-precision 40Ar/39Ar sanidine geochronology of ignimbrites in the Mogollon-Datil volcanic field, southwestern New Mexico. Bull Volcanol 52:584–601. doi: 10.1007/BF00301210

McIntosh WC, Chapin CE, Ratté JC, Sutter JF (1992) Time-stratigraphic framework for the Eocene-Oligocene Mogollon-Datil volcanic field, southwest New Mexico. Geol Soc Am Bull 104:851–871. doi: 10.1130/0016-7606(1945)56

McMillan NJ (2004) Magmatic record of Laramide subduction and the transition to Tertiary extension: Upper Cretaceous through Eocene igneous rocks in New Mexico, in, Mack, G.H., and Giles, K.A., eds., The Geology of New Mexico: A Geologic History, New Mexico Geological Society Special Publication 11, 249-270.

McMillan NJ, Dickin AP, Haag D (2000) Evolution of magma source regions in the Rio Grande rift, southern New Mexico. Geol Soc Am Bull 112:1582. doi: 10.1130/0016-7606

Michelfelder G, Feeley T, Wilder A, Klemetti E (2013) Modification of the Continental Crust by Subduction Zone Magmatism and Vice-Versa: Across-Strike Geochemical Variations of Silicic Lavas from Individual Eruptive Centers in the Andean Central Volcanic Zone. Geosciences 3:633–667. doi: 10.3390/geosciences3040633

Morgan DJ, Jerram DA (2006) On estimating crystal shape for crystal size distribution analysis. J Volcanol Geotherm Res 154:1–7. doi: 10.1016/j.jvolgeores.2005.09.016

Pistone M, Blundy J, Brooker RA (2017) Water transfer during magma mixing events: Insights into crystal mush rejuvenation and melt extraction processes. Am Mineral 102:766 LP-776.

Putirka, K. (2008) Thermometers and Barometers for Volcanic Systems. In: Putirka, K., Tepley, F. (Eds.), Minerals, Inclusions and Volcanic Processes, Reviews in Mineralogy and Geochemistry, Mineralogical Soc. Am. 69:61-120.

Ratté JC (1981) Geologic map of the Mogollon quadrangle, Catron County, New Mexico.

Ratté JC, Marvin RF, Naeser CW, Bikerman M (1984) Calderas and ash flow tuffs of the Mogollon Mountains, southwestern New Mexico. J Geophys Res 89:8713. doi: 10.1029/JB089iB10p08713

Ratté JC, McIntosh WC, Bove D (1994) Geologic map of the Milligan Mountain quadrangle, Catron County, New Mexico.

Rentz S (2017) Geochronology of calc-alkaline ash flow tuff units in the Mogollon-Datil volcanic field, southern New Mexico, U-Pb in zircon. Thesis, Missouri State University.

Rentz S, Michelfelder GS, Salings E (2016) The Cooney Tuff: ash fall in a calk-alkaline subduction related volcanic field, southern New Mexico. Geol Soc of Am, Abstracts with Programs 48:7. doi: 10.1130/abs/2016AM-281935

Salisbury MJ, Bohrson WA, Clynne MA, et al (2008) Multiple plagioclase crystal populations identified by crystal size distribution and in situ chemical data: Implications for timescales of magma chamber processes associated with the 1915 eruption of Lassen Peak, CA. J Petrol 49:1755–1780. doi: 10.1093/petrology/egn045

Salings E, Michelfelder G, Rentz S (in review) Magma Evolution in the Bursum Ignimbrite Complex, western Mogollon-Datil volcanic field, New Mexico: Evidence for Zoning of a Rhyolite Magma by Remobilization of a Crystal Mush. J Volcanol Geotherm Res.

Schleicher JM, Bergantz GW, Breidenthal RE, Burgisser A (2016) Time scales of crystal mixing in magma mushes. Geophys Res Lett 43:1543–1550. doi: 10.1002/2015GL067372

Shea T, Larsen JF, Gurioli L, et al (2009) Leucite crystals: Surviving witnesses of magmatic processes preceding the 79AD eruption at Vesuvius, Italy. Earth Planet Sci Lett 281:88–98. doi: 10.1016/j.epsl.2009.02.014.

Willcock MAW, Bargossi GM, Weinberg RF, et al (2015) A complex magma reservoir system for a large volume intra- to extra-caldera ignimbrite: Mineralogical and chemical architecture of the VEI8, Permian Ora ignimbrite (Italy). J Volcanol Geotherm Res 306:17–40. doi: 10.1016/j.jvolgeores.2015.09.015

Witter, M, Furman, T, LaFemina, P, et al (2016) Understanding magmatic processes at Telica volcano, Nicaragua: Crystal size distribution and textural analysis. Am Mineral 101:5: 1052-1060. doi: https://doi.org/10.2138/am-2016-5379

Wolff JA, Ramos FC (2014) Processes in caldera-forming high-silica rhyolite magma: Rb-Sr and pb isotope systematics of the otowi member of the bandeliertuff,valles caldera, new Mexico, USA. J Petrol 55:345–375. doi: 10.1093/petrology/egt070

Wotzlaw J-F, Schaltegger U, Frick DA, et al (2013) Tracking the evolution of large-volume silicic magma reservoirs from assembly to supereruption. Geology 41:867–870. doi: 10.1130/G34366.1

Yund, R., 1984, Alkali Feldspar exsolution: Kinetics and dependence on alkali interdiffusion, in Brown, W. L., editor, Feldspars and feldspathoids: Structure, Properties, and Occurrences: Dordrecht, D. Reidel Publishing Company, NATO Advanced Science Institute Series C, v. 137, p. 281–315.

Table 1. Modal percentages from samples in the BCT

Sample #	Feldspar	Quartz	Biotite	Opaques	Titanite
180-SP-2	8.6	1.3	0.7	1.4	0.4
180-SP-3	28.2	3.8	7.6	3.8	--
12RE1	26.0	2.4	1.8	1.5	0.7
12RE2	17.0	1.6	--	1.6	0.4
12RE5a	15	1.6	--	1.1	--
12RE5b	17.9	2.9	0.2	1.2	0.1
BCT-6	9.1	3.7	--	0.8	--
BCT-6-2	9.3	0.2	--	0.1	--
12RE4	12.1	1	--	0.6	0.4
BCT-8a	11	0.9	0.1	2	0.1
BCT-8b	16.8	0.6	--	0.5	0.2

Table 2. Mineral chemistry of selected sanidine samples

Sample #	SiO_2	Al_2O_3	Na_2O	K_2O	TiO_2	CaO	FeO
12RE5b 1-1	67.534	18.851	5.733	8.591	0.002	0.184	0.22
12RE5b 1-3	67.665	18.873	5.763	8.488	0.025	0.174	0.25
12RE5b 7	65.922	18.836	5.593	8.59	0.026	0.197	0.209
12RE5b 11	63.285	19.254	6.394	7.467	0.023	0.476	0.204
12RE5b 15-1	64.846	19.301	7.051	6.746	0.005	0.433	0.219
12RE5b 15-2	65.121	18.887	5.861	8.457	--	0.24	0.271
12RE5b 20	63.945	19.524	6.856	6.537	0.035	0.66	0.203
12RE5b 20-2	64.271	19.6	7.95	5.81	0.005	0.803	0.233
12RE5a 1	66.646	18.91	6.239	8.026	0.003	0.205	0.219
12RE5a 1-2	66.656	18.832	6.066	8.333	0.015	0.191	0.213
12RE5a 3	64.568	18.506	5.634	8.597	--	0.167	0.219
12RE5a 11-1	67.243	18.866	5.729	8.654	0.014	0.188	0.243
12RE5a 11-2	66.459	18.836	5.563	8.844	0.004	0.204	0.201
12RE5a 17	65.743	19.064	5.773	8.476	0.015	0.196	0.259
12RE5a 19	63.954	18.896	6.135	8.206	0.02	0.176	0.19
180-SP-2 1	66.516	18.725	5.649	8.779	0.001	0.166	0.201
180-SP-2 4	66.693	18.791	5.574	8.894	0.011	0.158	0.255
180-SP-2 4-2	66.529	18.749	5.425	9.057	0.008	0.183	0.225
180-SP-2 9	66.759	18.879	5.462	8.928	0.016	0.202	0.248
180-SP-2 14	66.403	18.58	5.671	8.786	0.022	0.169	0.212
180-SP-2 15	65.459	18.236	5.394	8.708	0.007	0.207	0.237
180-SP-2 15-2	66.095	18.768	5.557	8.856	0.007	0.177	0.216
180-SP-2 18	66.129	18.939	5.618	8.999	0.015	0.143	0.23

*-- represents data below detection limit.

Table 2 continued

Sample #	Sr (ppm)	Pb (ppm)	Ba (ppm)
12RE5b 1-1	2110	470	--
12RE5b 1-3	1810	--	170
12RE5b 7	1920	--	--
12RE5b 11	2390	50	--
12RE5b 15-1	1990	--	760
12RE5b 15-2	1760	220	300
12RE5b 20	2380	250	1460
12RE5b 20-2	2140	--	580
12RE5a 1	2000	--	--
12RE5a 1-2	2150	--	370
12RE5a 3	2150	150	700
12RE5a 11-1	2030	120	740
12RE5a 11-2	2180	350	--
12RE5a 17	2080	200	--
12RE5a 19	1760	580	--
180-SP-2 1	2290	--	150
180-SP-2 4	2210	--	430
180-SP-2 4-2	1730	--	--
180-SP-2 9	2210	450	520
180-SP-2 14	2200	60	70
180-SP-2 15	1960	90	--
180-SP-2 15-2	1950	--	--
180-SP-2 18	2110	--	--

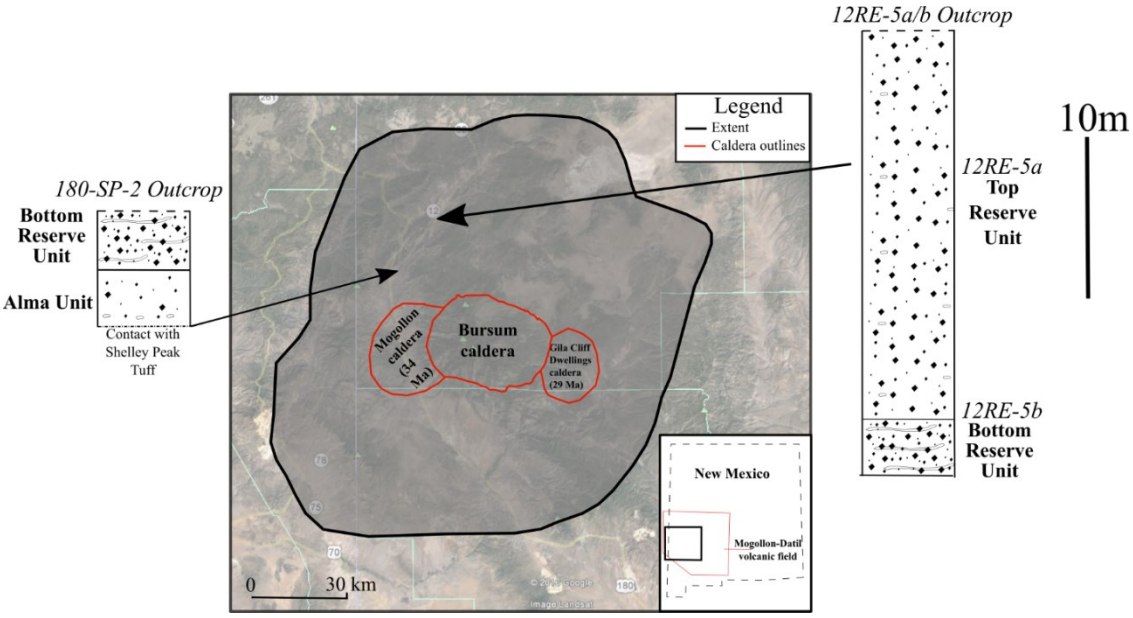

Figure 1. Regional map of the extent of the Bloodgood Canyon Tuff with stratigraphic sections of select sample locations

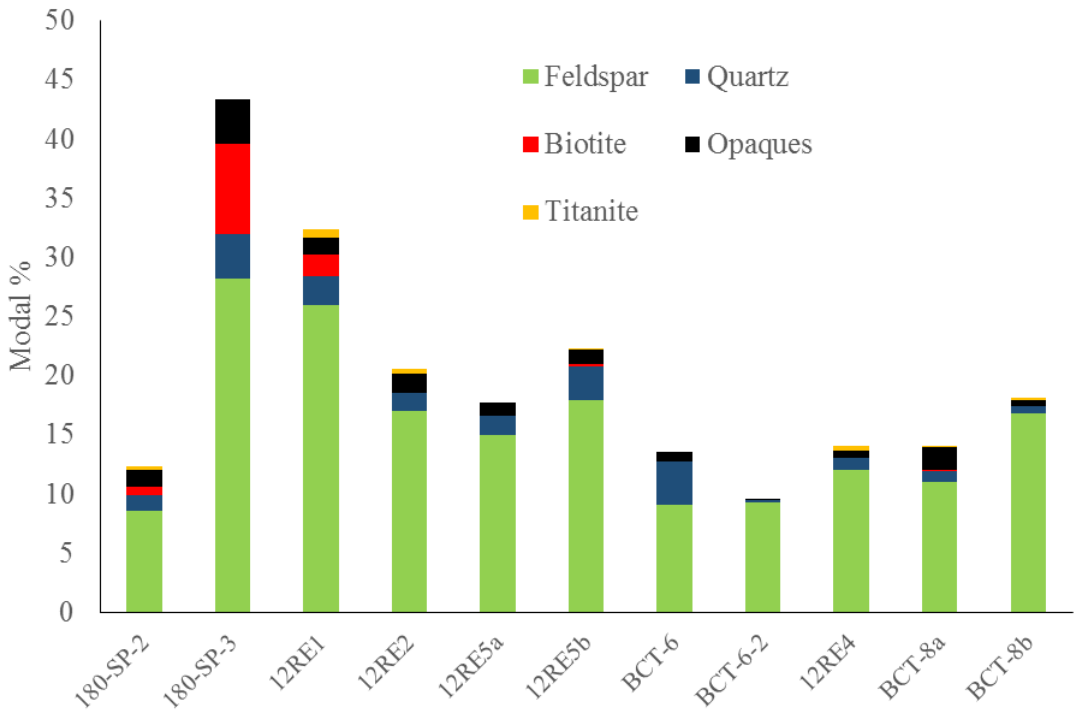

Figure 2. Modal percentages of mineral phases in samples collected from the Bloodgood Canyon Tuff. Trace phases not shown

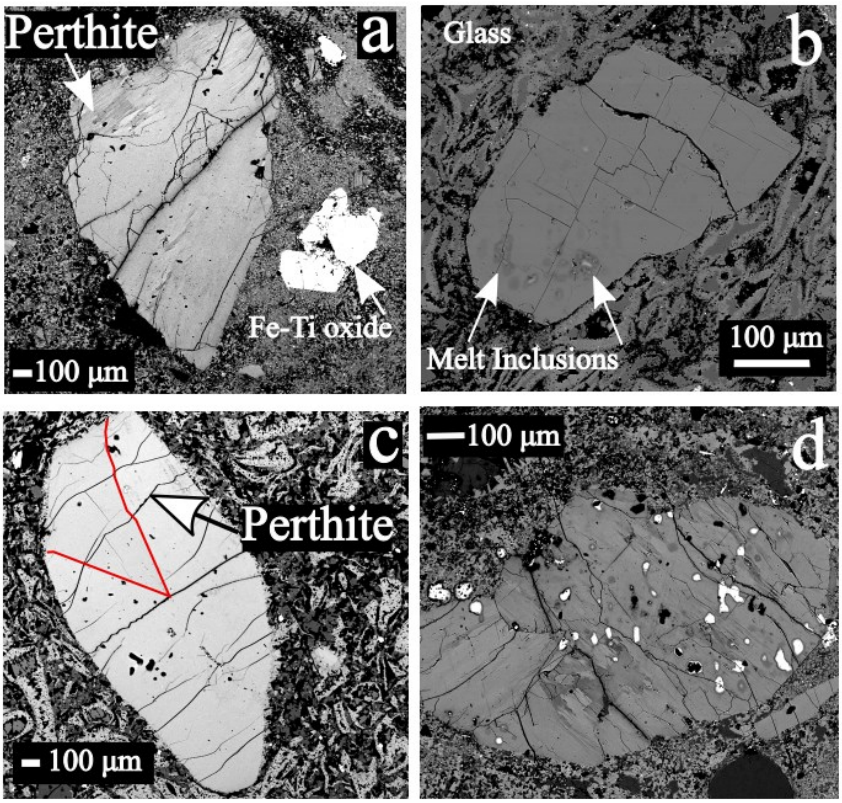

Figure 3a-d. BSE images of perthitic feldspars in various samples **a** Class 1 feldspar 12RE5b 2 from sample 12RE5b. Perthitic textures at present dominantly at the top of the grain. **b** Class 3 feldspar 180-SP-2 17 from sample 180-SP-2. Perthitic textures in this grain are very small but run through most of the grain. **c** Class 1 feldspar 12RE5a 11. The perthite is highlighted. **d** Class 1 feldspar 12RE5b 4. Perthite in this grain is irregular, possibly due to the amount of alteration

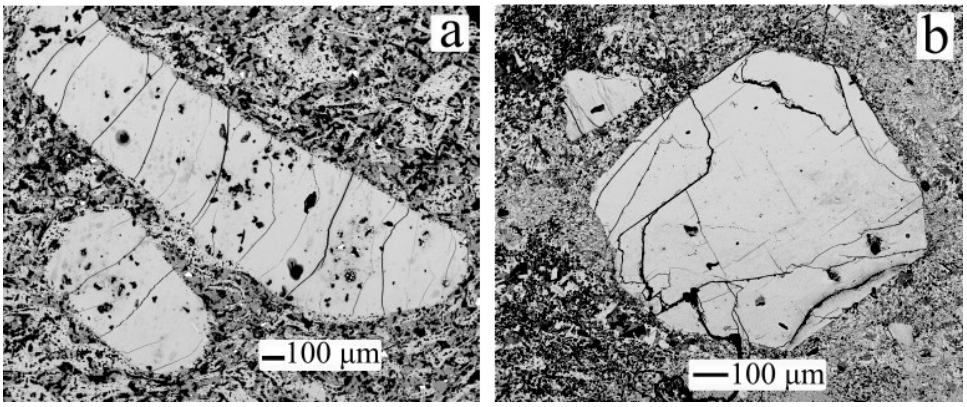

Figure 4a-b. BSE images of feldspar grains **a** Class 2 feldspars 12RE5a 3 (top) and 12RE5a 4 (bottom). **b** Class 4 feldspar grain 12RE5b 24. A small perthite feldspar is in the top left

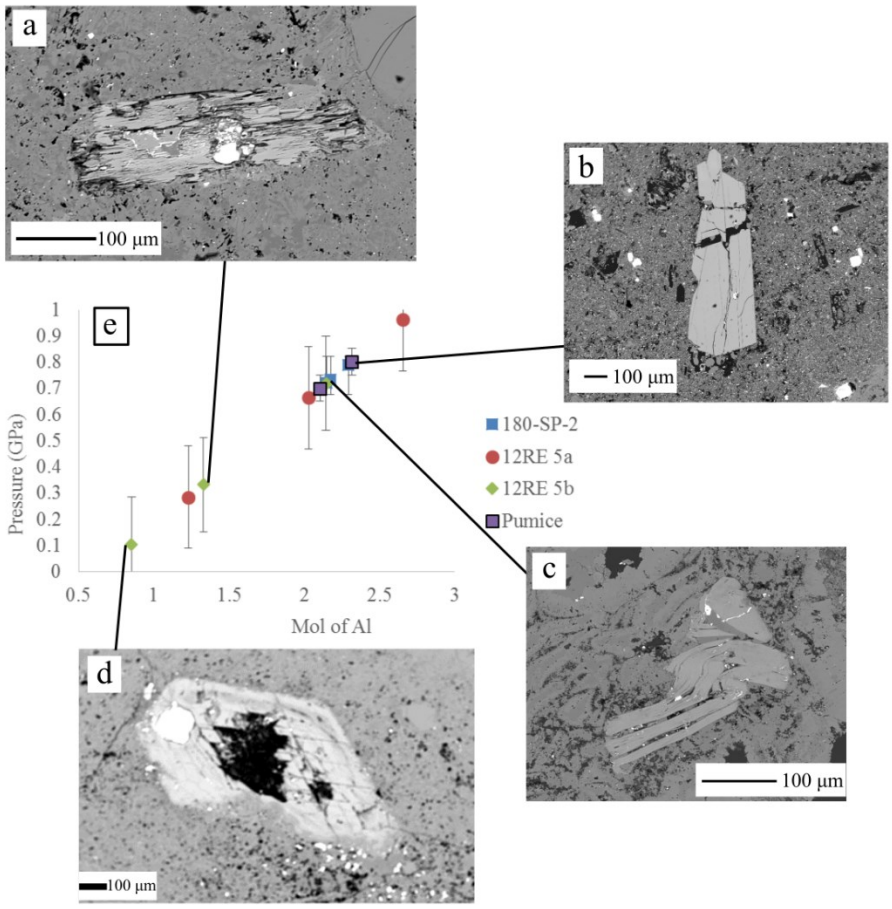

Figure 5a-e. Backscatter images of hornblendes in various samples of the BCT and pressure diagram from Al-in-Hornblende method (Ague and Brandon 1996) **a** 12RE5b H4 **b** 180-SP-2 H4, hornblende inside a pumice fragment of the Shelley Peak Tuff **c** 180-SP-2 H2 **d** 12RE5b H1 **e** Results of Al-in-Hornblende method compared to mol of Al. Pumice data points are from a brown pumice in 180-SP-2

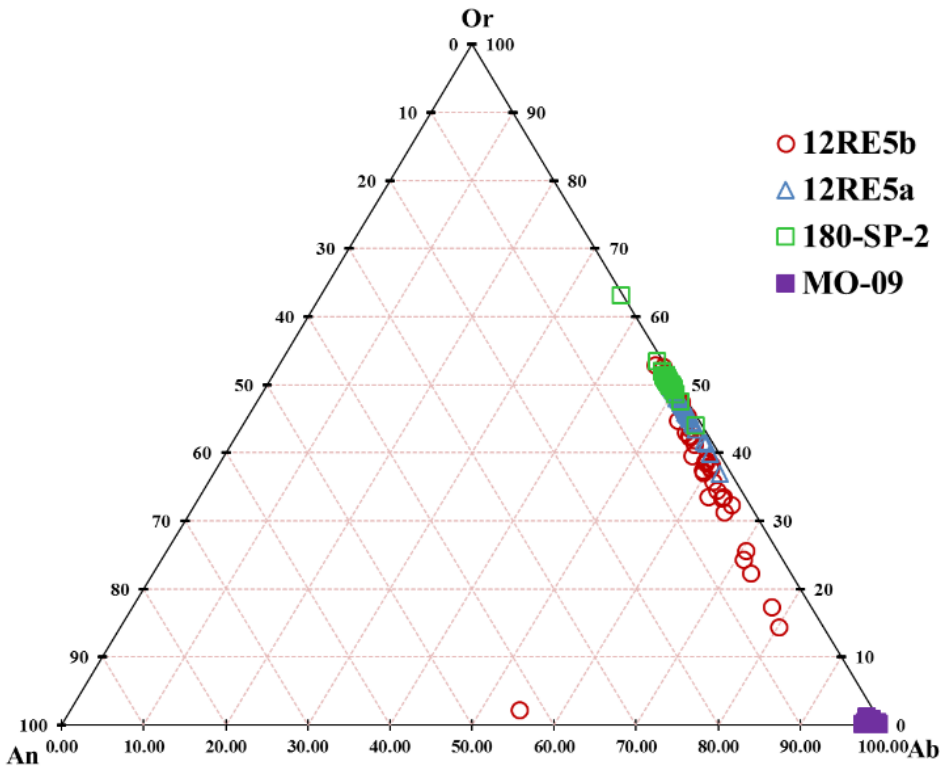

Figure 6. Feldspar ternary diagram depicting feldspar compositions for the BCT and Cooney Formation

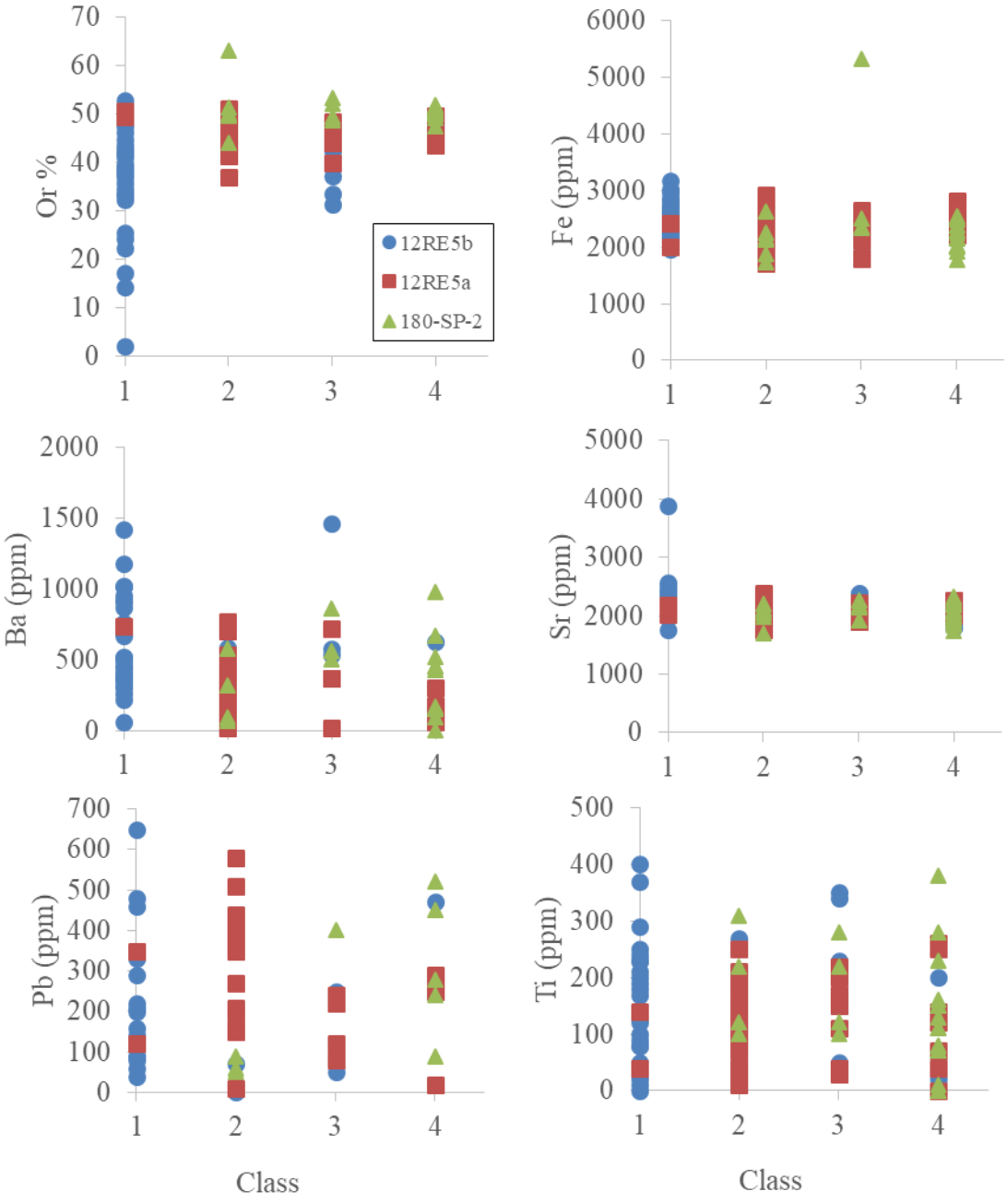

Figure 7. Major- and trace-elements in feldspar phenocrysts organized by class

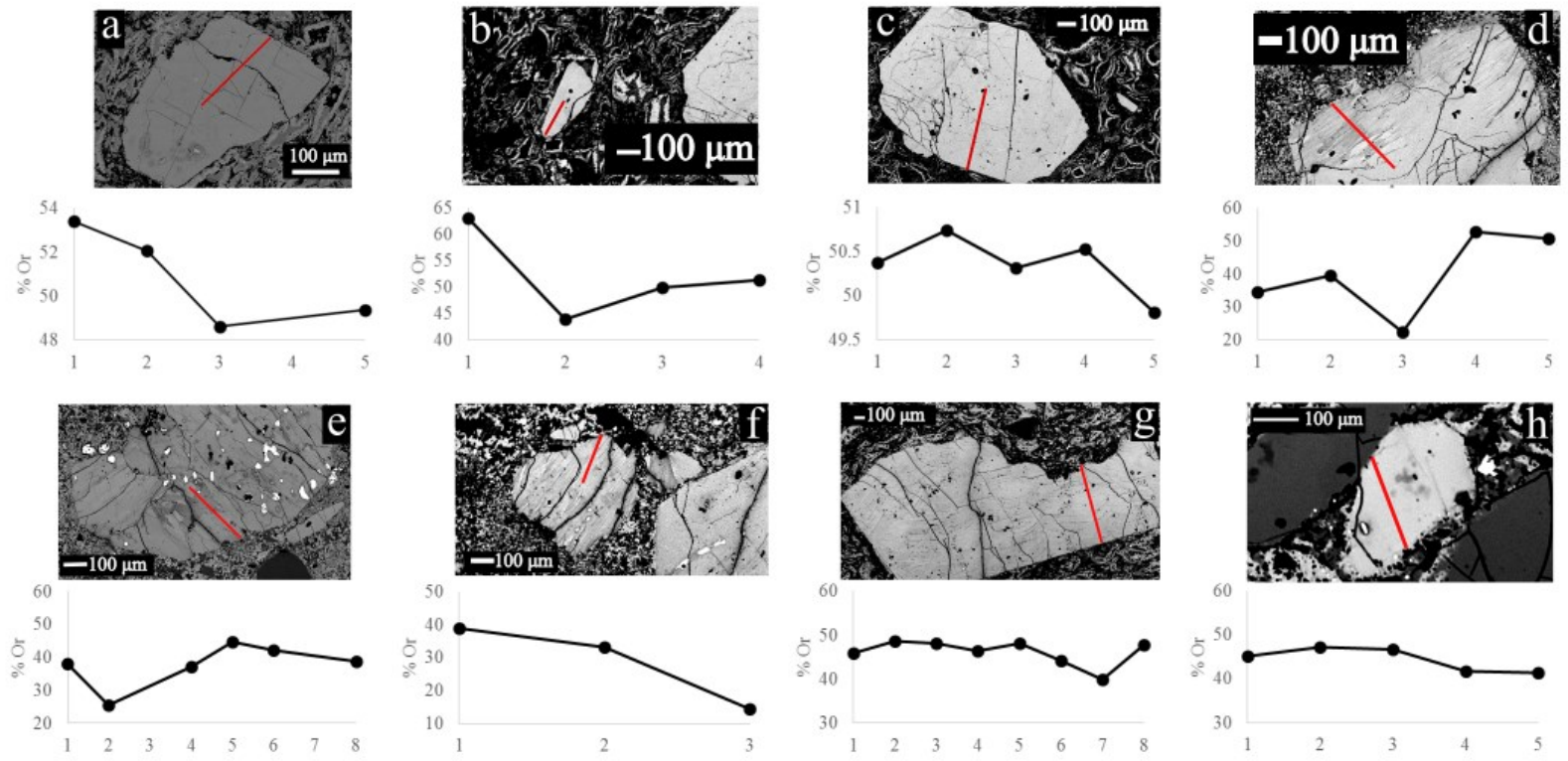

Figure 8. BSE images and line transects of % Or across select sanidines **a** 180-SP-2-17 **b** 180-SP-2-7 **c** 180-SP-2-5 **d** 12RE5b-2 **e** 12RE5b-4 **f** 12RE5b-19 **g** 12RE5a-16 **h** 12RE5a-24

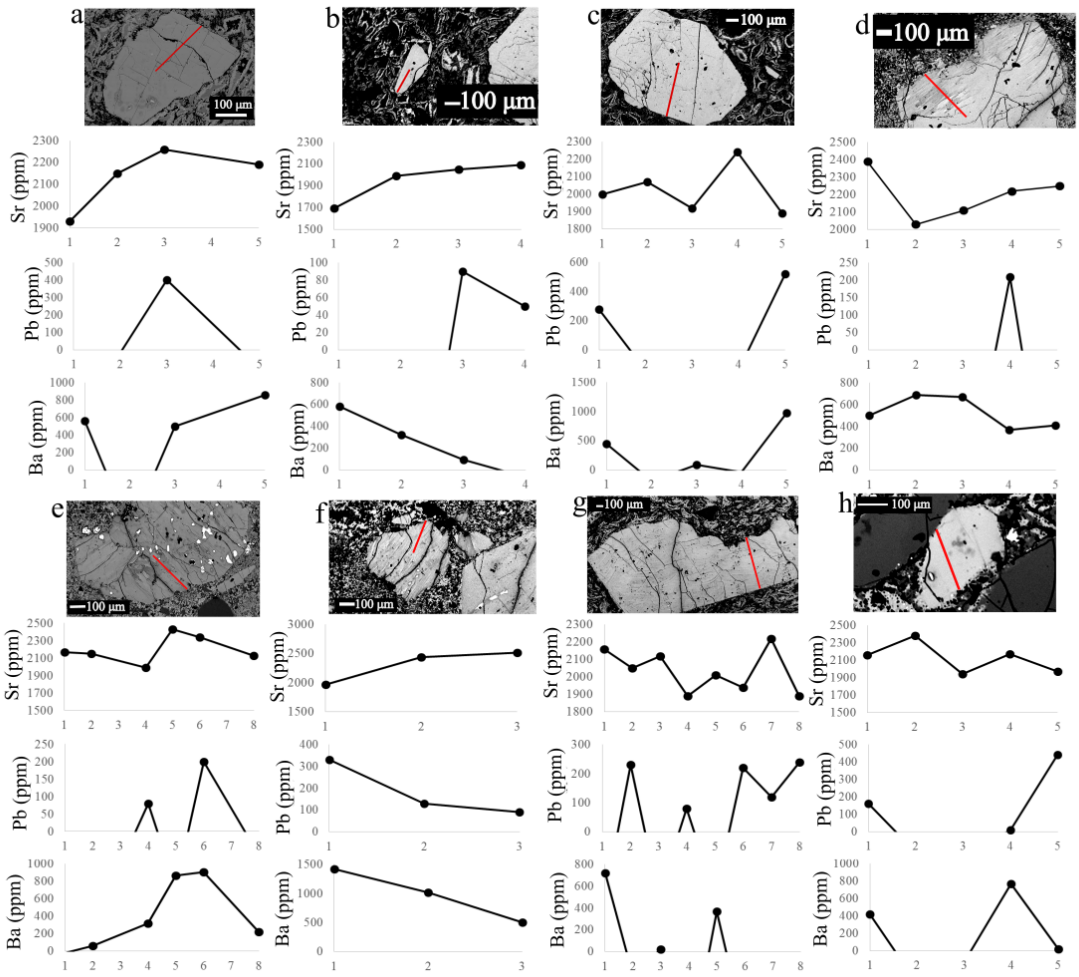

Figure 9. Line transects of Sr, Pb, and Ba across select sanidines **a** 180-SP-2-17 **b** 180-SP-2-7 **c** 180-SP-2-5 **d** 12RE5b-2 **e** 12RE5b-4 **f** 12RE5b-19 **g** 12RE5a-16 **h** 12RE5a-24

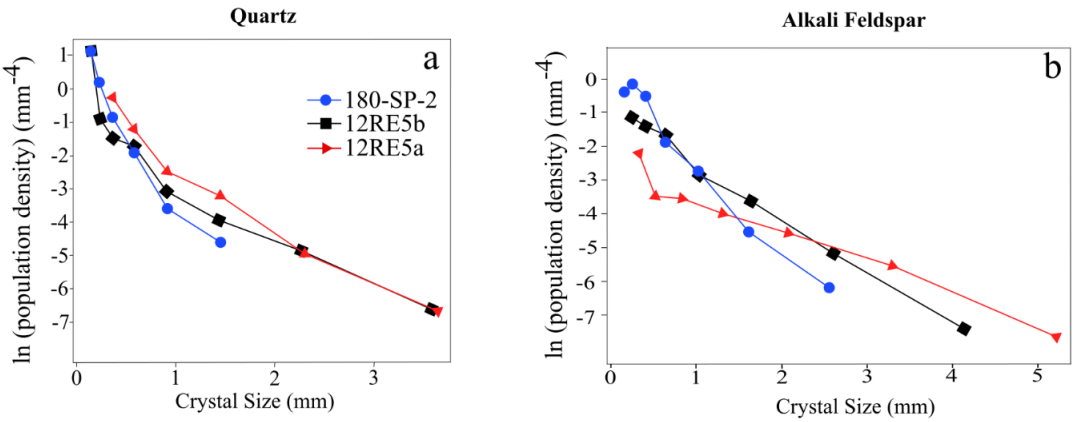

Figure 10. Crystal size distribution (CSD) curves of quartz and alkali feldspar for three samples from the Bloodgood Canyon Tuff. **a** Quartz CSD curves and **b** Alkali feldspar curves

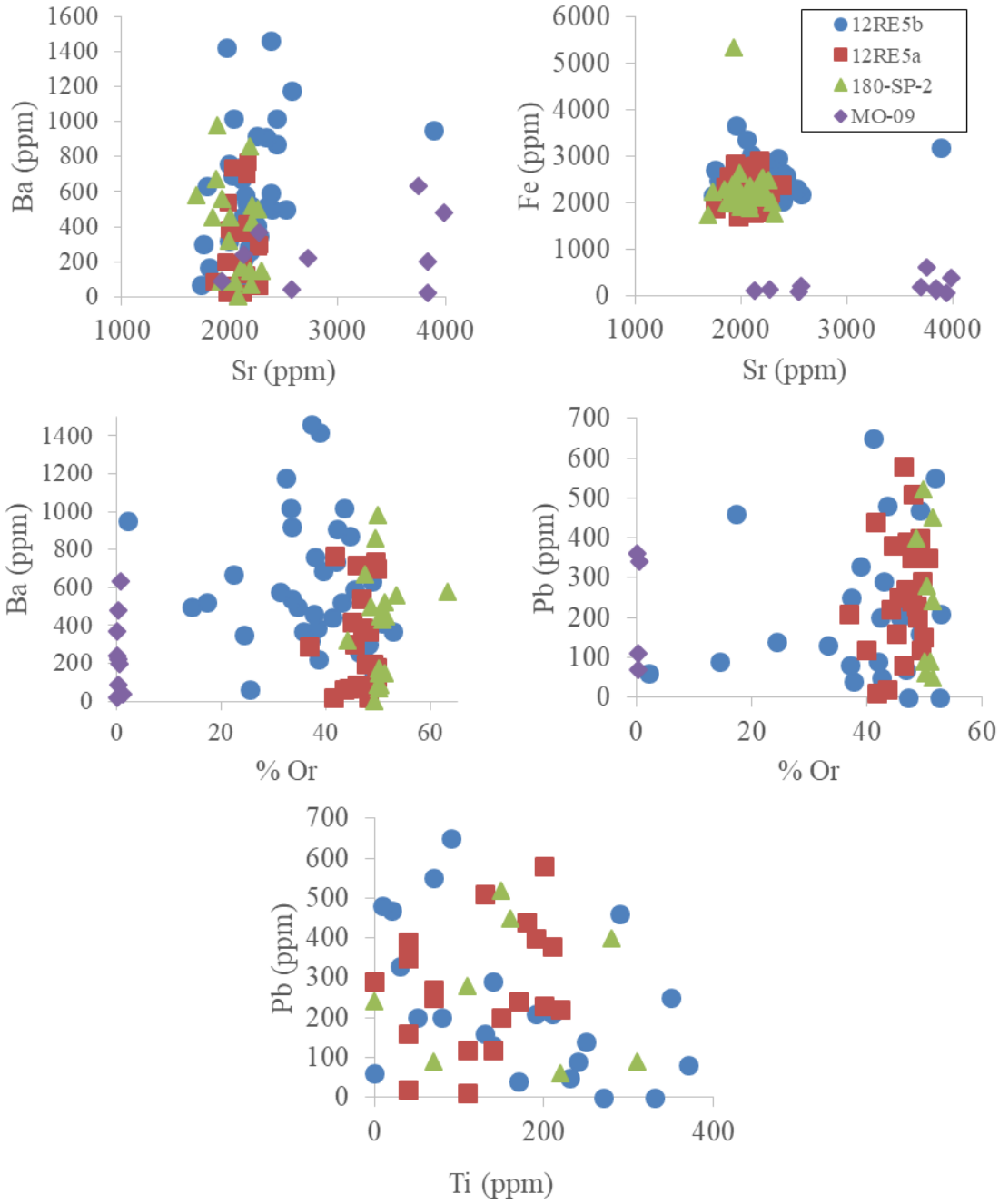

Figure 11. Trace element diagrams for three BCT samples and one Cooney Formation sample (MO-09)

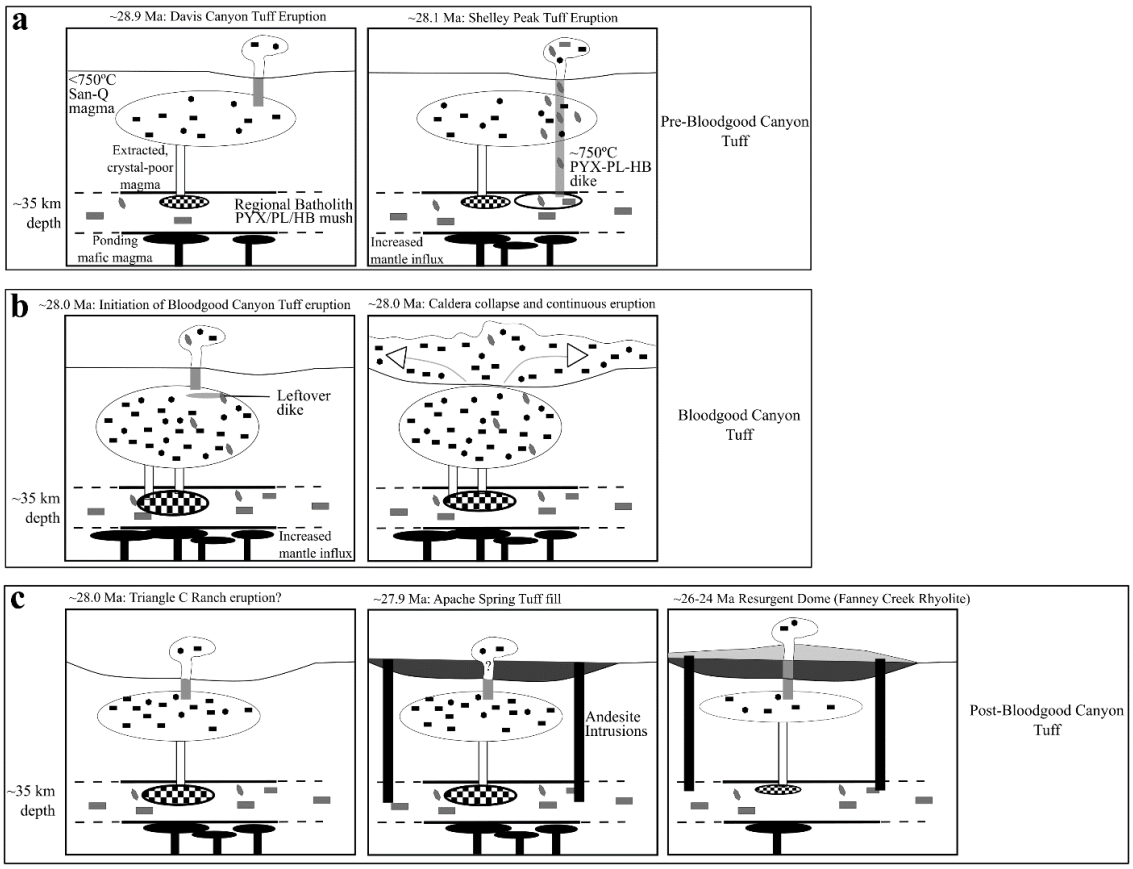

Figure 12. Evolution diagram for the BCT (not to scale). **a** Pre-Bloodgood Canyon Tuff (BCT): after eruption of the Davis Canyon Tuff, the remaining crystal-poor magma assimilates with the surrounding Hornblende-Biotite Granite wallrock as magma from extracted melt in the underlying cumulate intrudes into the magma reservoir. An increase in mantle influx causes an intrusion from the cumulate to rise through the crust and the reservoir to erupt. **b** Increased mantle influx causes the extracted melt volume to increase, building up the magma reservoir, and eventually destabilizes the magma chamber. After initial eruption of the BCT, the Bursum caldera collapses in a trapdoor fashion and erupts out much of the remaining eruptible magma. **c** After eruption of the BCT, the Triangle C Ranch may have erupted. Soon afterward or simultaneously, the Apache Spring Tuff filled in the Bursum caldera, though whether the Apache Spring Tuff is actually a product from the Bursum caldera is still unclear (Salings et al. in review). Between eruption of the BCT and resurgence, andesite intrusions from the cumulate were erupting in the region.

CONCLUSIONS

The manuscripts presented here examine the magmatic evolution of the Bloodgood Canyon Tuff (BCT) and its relation to the regional ignimbrite flare-up in the Mogollon-Datil volcanic field (MDVF). This study sought to answer three questions that are important to understanding the MDVF by focusing on the magma chamber evolution during the emplacement of the BCT. First, are the BCT and associated units, the Apache Spring Tuff, and Fanney Rhyolite petrologically related to each other (did they come from the same source)? Second, what magmatic processes led to the accumulation of magma prior to eruption of the BCT? Third, how does the BCT reflect the ignimbrite flare-up within the MDVF?

This study reveals that the BCT is geochemically distinct from the Apache Spring Tuff and the Fanney Rhyolite, but was formed by the assimilation of magma similar to the Davis Canyon Tuff with biotite hornblende granite/amphibolite composition wallrock. A series of intrusions fed by a plagioclase-clinopyroxene-rich cumulate from the middle/lower crust fed the growing magma reservoir of the BCT until, during the peak of the ignimbrite flare-up, the intrusion rate outpaced the stabilization, and thermal destabilization triggered an eruption. The high influx of mantle material due to the ignimbrite flare-up, provided the heat necessary to drive magma evolution in the region. Whole-rock major- and trace-element concentrations, radiogenic isotope ratios, petrography, mineral grain geochemistry, and petrologic modeling methods provide evidence that the Bloodgood Canyon Tuff was erupted from incremental assemblage of a

rhyolite composition magmatic body extracted from a dacitic plagioclase-pyroxene-hornblende crystal mush.

The following conclusions can be made from this study:

1. The pumice-poor nature of the BCT and the increased amount of crypto-perthite textures in the middle and top of the section compared to the bottom of the section suggests that the eruption was dense and collapse of the caldera occurred early in the eruption driving the continuation of the eruption and driving pyroclastic flows over plinian-fall deposits.

2. Compositional zoning within the ignimbrite suggest three compositional zones representing eruption from a stratigraphically zoned magma chamber. The stratigraphy of the BCT suggests that the crystallinity of the tuff exhibits a progressive nearly linear upward increase in phenocryst content (10-45 vol.%) and in particular an increase in sanidine phenocrysts. This suggests that prior to eruption, the cooler outer margin of a large magma body consisted of a rigid mush of interlocking crystals (>50 vol.%) and interstitial melt whereas the inner core of the body consisted of a more mobile crystal cumulate (<45 vol.%). Eruption started from center of the magma body driving evacuation from the center outward and from the top down.

3. Trace-elements (REEs, Dy/Dy*, Eu/Eu*) and radiogenic isotope ratios (Sr, Nd, and Pb) suggest a highly differentiated and contaminated source that was amphibole or clinopyroxene stable at the top of the chamber (Dy/Dy*=0.57; ϵNd= -6.8) and had more crustal contamination at the bottom of the chamber (Dy/Dy* = 0.92; εNd= -6.7). Mineral grain Sr and Ba concentrations suggest a feldspar-stable source, with not much variation throughout crystals. Mineral grain Pb values suggest three populations of euhedral sanidines, low-, medium-, and high-Pb concentrations.

4. Crystal size distributions reveal three crystallization events in the magma chamber before eruption, but the absence of visible zoning and systematic changes in trace elements suggests that the magma chamber was in equilibrium until immediately prior to eruption. There is no viable correlation between crystal sizes and trace element concentrations, so changes in the magma chemistry do not seem to be related to crystallization events. CSDs also indicate that smaller crystals were preferentially being resorbed over larger crystals (Ostwald ripening) before eruption, further establishing a quick timeline for thermal disequilibrium. The lack of recrystallization zones also indicates that eruption took place before the magma chamber could re-equilibrate.

5. Petrologic modeling and petrography shows that the base of the BCT was formed from the crustal melting of amphibolitic/ biotite-hornblende granite composition (Amato et al., 2011) crust after the eruption of the Davis Canyon Tuff, but the rest

was formed from continuous inputs of dacitic plagioclase-clinopyroxene-hornblende composition magma from a deeper reservoir. Variation in trace elements within single crystals but absence of visible zoning suggests multiple intrusion events of a similar composition magma into the base of the top reservoir. The higher whole-rock Sr content in the middle and top of the BCT suggests that the magma had a low Sr concentration, and Sr content in whole-rock analyses is related to the modal % of sanidines, and the presence of altered hornblendes suggests that hornblende was stable for a longer period before being resorbed into the new BCT magma.

6. The Shelley Peak Tuff was a tuff that erupted immediately prior to the BCT and is sourced from the same magma system. However, modal assemblages of plagioclase-clinopyroxene, and hornblende conflict with modal assemblages of the two tuffs immediately older and younger than it, which consist of quartz, sanidine, and biotite. The mush below the BCT and Davis Canyon Tuff reservoir is believed to consist of plagioclase-clinopyroxene, and hornblende, so it is suggested that increased mantle influx caused dike propagation off the crystal mush and the Shelley Peak Tuff completely bypassed the magma reservoir holding the BCT/Davis Canyon Tuff magmas.

7. Radiogenic Sr isotope ratios for the Shelley Peak Tuff and the BCT and pressures obtained from hornblendes in pumice fragments suggest the magma reservoir for the BCT was extracted from the lower reservoir when incoming high-temperature mafic material ponded and filtered below the crystal mush and provided heat to the overlying chamber. Crypto-perthite textures provide evidence that the magma chamber was under disequilibrium prior to eruption, but the absence of recrystallization textures suggests that the disequilibrium triggered eruption before re-equilibration could occur. The higher occurrence of crypto-perthites and frequency of larger-sized quartz and sanidine grains in the middle and top of the section suggests that the whole magma chamber was not evacuated at once, but rather in a two-step process. The first, initial eruption of the BCT after thermal destabilization evacuated the bottom of the stratigraphic section. Once eruption of the BCT was underway, the magma chamber further destabilized, initiating trap-door style collapse of the BCT and erupting the remaining eruptible magma to form the middle and top of the BCT, which are more derived from the actual crystal mush than the bottom of the stratigraphic section. Once the BCT erupted and collapsed the Bursum caldera, the AST erupted and evacuated another section of the chamber.

8. Two million years after the eruption of the BCT, the ignimbrite flare-up was waning, and the crystal mush had begun to lock up again (>50% crystallinity), forming another crystal-poor rhyolite lens that erupted as the Fanney Rhyolite. However, the relationship between the BCT, AST, and Fanney Rhyolite is still unclear, and further sampling is needed to establish a statistically viable correlation.

FULL REFERENCES LIST

Ague J.J. and Brandon M.T., 1996, Regional tilt of the Mount Stuart batholith, Washington, determined using aluminum-in-hornblende barometry: Implications for northward translation of Baja British Columbia. Bulletin of the Geological Society of America, v. 108, p. 471–488, doi: 10.1130/0016-7606(1996)108<0471:RTOTMS>2.3.CO;2.

Allan A.S.R., Morgan D.J., Wilson C.J.N., Millet M.A., 2013, From mush to eruption in centuries: Assembly of the super-sized Oruanui magma body. Contributions to Mineralogy and Petrology, v. 166, p. 143–164, doi: 10.1007/s00410-013-0869-2.

Amato, J., Heizler, M., Boullion, A., Sanderas, A.E., Toro, J., McLemore, V.T., and Andronicos, C.L., 2011, Syntectonic 1.46 Ga magmatism and rapid cooling of a gneiss dome in the southern Mazatzal Province: Burro Mountains, New Mexico: Geological Society of America Bulletin, v. 123, p. 1720-1744, doi: 10.1130/B30337.1.

Bachmann, O. and Bergantz, G., 2004, On the origin of crystal-poor rhyolites: extracted from batholithic crystal mushes: Journal of Petrology, v. 45, no. 8, p. 1565-1582, doi: 10.1093/petrology/egh019.

Bachmann, O. and Bergantz, G., 2006, Gas percolation in upper-crustal silicic crystal mushes as a mechanism for upward heat advection and rejuvenation of near-solidus magma bodies: Journal of Volcanology and Geothermal Research, v. 149, no. 1, p. 85-102.

Bachmann, O. and Bergantz, G., 2008, The magma reservoirs that feed supereruptions: Elements, v. 4, p. 17-21, doi: 10.2113/GSELEMENTS.4.1.17.

Bachmann, O., Deering, C.D., Lipman, P.W., and Plummer, C., 2014, Building zoned ignimbrites by recycling silicic cumulates: insight from the 1,000 km^3 Carpenter Ridge Tuff, CO: Contributions to Mineralogy and Petrology, v. 167, 13 p., doi: 10.1007/s00410-014-1025-3.

Bachmann, O., and Dungan, M.A., 2002, Temperature-induced Al-zoning in hornblendes of the Fish Canyon magma, Colorado: American Mineralogist, v. 87, p. 1062–1076.

Bachmann, O., and Huber, C., 2016, Silicic magma reservoirs in the Earth's crust: American Mineralogist, v. 101, p. 2377–2404, doi: 10.2138/am-2016-5675.

Bacon, C.R. and Druitt, T.H., 1988, Compositional Evolution of the Zoned Calcalkaline Magma Chamber of Mount-Mazama, Crater Lake, Oregon: Contributions to Mineralogy and Petrology, v. 98, no. 2, p. 224-256.

Bégué, F., Deering, C.D., Gravley, D.M., Kennedy, B.M., Chambefort, I., Gualda, G.A.R., and Bachmann, O., 2014, Extraction, storage and eruption of multiple isolated magma batches in the paired Mamaku and Ohakuri eruption,Taupo volcanic zone, New Zealand: Journal of Petrology, v. 55, p. 1653–1684, doi: 10.1093/petrology/egu038.

Bergantz, G., Schleicher, J.M., and Burgisser, A., 2015, Open-system dynamics and mixing in magma mushes: Nature Geoscience, v. 8, p. 793-795, doi: 10.1038/NGEO2534.

Bikerman, M., 1972, New K-Ar ages on volcanic rock from Catron and Grant Counties, New Mexico: Isochron West, no. 3, p. 9-12.

Bikerman, M., 1989, Rb, Sr, Rb-Sr, and isotopic Sr values for volcanic rocks from southwestern part of the Mogollon-Datil volcanic field: New Mexico Geology, v. 11, p. 76-83.

Bikerman, M., 1994, Are the western Mogollon-Datil mid-Cenozoic ash flows cogenetic? Pearce element ratios and isotope aspects of the question *in* New Mexico Geological Society Guidebook, 45th Field Conference: Soccorro, NM, New Mexico Geological Society, 187-192.

Bikerman, M., Bell, K., and Card, J.W., 1992, Strontium and neodymium isotopic study of the western Mogollon-Datil volcanic region, New Mexico, USA: Contributions to Mineralogy and Petrology, v. 109, no. 4, p. 459-470, doi: 10.1007/BF00306549.

Brugger C.R., Hammer J.E., 2010, Crystal size distribution analysis of plagioclase in experimentally decompressed hydrous rhyodacite magma: Earth and Planetary Science Letters, v. 300, p. 246–254, doi: 10.1016/j.epsl.2010.09.046.

Cashman, K.V., Marsh, B.D., 1988, Crystal size distribution (CSD) in rocks and the kinetics and dynamics of crystallization II: Makaopuhi lava lake: Contributions to Mineralogy Petrology, v. 99, no. 5, p. 292-305, doi:10.1007/BF00375363.

Chamberlain, K., 2015, Unraveling the magmatic processes behind zoned fall units on Ascension Island, South Atlantic: 2015 American Geophysical Union Fall Meeting.

Chamberlin R.M., 2015, Geochemical, mineralogical, textural and map data for crystal-rich, caldera facies Hells Mesa Tuff and a comagmatic lava dome, central New Mexico: with a note on compositional zoning: New Mexico Bureau of Geology and Mineral Resources Open File Report 568.

Chamberlin, RM, Chapin, CE, McIntosh, WC, 2002, Westward migrating ignimbrite calderas and a large radiating mafic dike swarm of Oligocene age, central Rio

Grande rift, New Mexico: surface expression of an upper mantle diapir?: Geological Society of America, Abstracts with Programs, v. 34, no. 6, p. 438.

Chapin, C.E., Wilks, M., and Mcintosh, W.C., 2004, Spacetime patterns of Late Cretaceous to present magmatism in New Mexico—comparison with Andean volcanism and potential for future volcanism: New Mexico Bureau of Geology and Mineral Resources, Bulletin, v. 160, p. 13–40.

Cooper, K.M., 2017, What does a magma reservoir look like? The "Crystal's-Eye" View: Elements, v. 13, p. 23-28, doi: 10.2113/gselements.13.1.23.

Cooper, K.M., and Kent, A.J.R., 2014, Rapid remobilization of magmatic crystals kept in cold storage: Nature, v. 506, p. 480–3, doi: 10.1038/nature12991.

Cooper, G.F., and Wilson, CJ.N., 2014, Development, mobilisation and eruption of a large crystal-rich rhyolite: The Ongatiti ignimbrite, New Zealand: Lithos, v. 198–199, p. 38–57, doi: 10.1016/j.lithos.2014.03.014.

Davidson, J., Turner, S., and Plank, T., 2013, Dy/Dy*: Variations arising from mantle sources and petrogenetic process: Journal of Petrology, v. 54, no. 3, p. 525-537, doi: 10.1093/petrology/egs076.

Davis, J.M., and Hawkesworth, C.J., 1993, The petrogenesis of 30-20 Ma basic and intermediate volcanics from the Mogollon-Datil volcanic field, New Mexico, USA: Contributions to Mineralogy and Petrology, v. 115, no. 2, p. 165-183, doi: 10.1007/BF00321218.

Davis, J.M., and Hawkesworth, C.J., 1994, Early calc-alkaline magmatism in the Mogollon-Datil Volcanic Field, New Mexico, USA: Journal of the Geological Society [London], v. 151, no. 5, p. 825-843, doi: 10.1144/gsjgs.151.5.0825.

De Silva, S., Zandt, G., Trumbull, R., Viramonte, J.G., Salas, G., and Jiménez, N., 2006, Large ignimbrite eruptions and volcano-tectonic depressions in the Central Andes: a thermomechanical perspective *from* Troise, C., de Natale, G., and Kilburn, C.R.J. (eds) Mechanisms of Activity and Unrest at Large Calderas, Geological Society, London, Special Publications, v. 269, p. 47-63.

DePaolo, D.J., 1981, Trace element and isotopic effects of combined wallrock assimilation and fractional crystallization: Earth Planet Science Letters, v. 53, p. 189-202.

DePaolo, D.J., 1981, A Neodymium and Strontium isotopic study of the Mesozoic Calc-alkaline granitic batholiths of the Sierra Nevada and Peninsular Ranges, California: Journal of Geophysical Research, v. 86, no. B11, p. 10470-10788.

Duffield, W. A. and Dalrymple, G. B., 1990, The Taylor Creek Rhyolite of New Mexico; a rapidly emplaced field of lava domes and flows: Bulletin of Volcanology, v. 52, p. 475–487.

Elston, W.E., Coney, P., and Rhodes, R.C., 1970, Progress report on the Mogollon Plateau Volcanic Province, southwestern New Mexico: No. 2*, *in* Woodward, L.A., ed., Tyrone-Big Hatchet Mountain-Florida Mountains Region: New Mexico Geological Society, 21st Annual Field Conference, Guidebook, p. 75-86.

Elston, W.E., 1984, Mid-Tertiary ash flow tuff cauldrons, southwestern New Mexico: Journal of Geophysical Research, v. 89, no. B10, p. 8733-8750, doi: 10.1029/JB089iB10p08733.

Elston, W.E., 2008, The ~28 Ma Bursum Cauldron, viewed from the Aldo Leopold Vista and from Holt Mountain, *in* Mack, G.H., Witcher, J.C., and Leuth, V.W., eds., Geology of the Gila Wilderness-Silver City area: New Mexico Geological Society, 59th Annual Field Conference, Guidebook, p. 14-16.

Forni, F., Bachmann, O., Mollo, S., de Astis, G., Gelman, S.E., and Ellis, B.S., 2016, The origin of a zoned ignimbrite: Insights into the Campanian Ignimbrite magma chamber (Campi Flegrei, Italy): Earth and Planetary Science Letters, v. 449, p. 259-271, doi: 10.1016/j.epsl.2016.06.003.

Gelman, S.E., Deering, C.D., Bachmann, O., Huber, C., and Gutiérrez, F.J., 2014, Identifying the crystal graveyards remaining after large silicic eruptions: Earth and Planetary Science Letters, v. 403, p. 299–306, doi: 10.1016/j.epsl.2014.07.005.

Ginire, C., and Wörner, G., 2007, Variable parent magmas and recharge regimes of the Parinacota magma system (N. Chile) revealed by Fe, Mg and Sr zoning in plagioclase: Lithos, v. 98, p. 118–140, doi: 10.1016/j.lithos.2007.03.004.

Ginibre C, Wörner G, and Kronz A, 2007, Crystal Zoning as an Archive for Magma Evolution: Elements, v. 3, p. 261–266.

Girard, G., and Stix, J., 2009, Magma recharge and crystal mush rejuvenation associated with early post-collapse Upper Basin Member rhyolites, Yellowstone caldera, Wyoming: Journal of Petrology, v. 50, p. 2095–2125, doi: 10.1093/petrology/egp070.

Glazner, A.F., Bartley, J.M., Coleman, D.S., Gray, W., and Taylor, R.Z., 2004, Are plutons assembled over millions of years by amalgamation from small magma chambers?: GSA Today, v. 14, no. 4, p. 5-11.

Graeter, K., Beane, R.J., Deering, C.D., Gravley, D., and Bachmann, O., 2015, Formation of rhyolite at the Okataina Volcanic Complex, New Zealand: New insights from

analysis of quartz clusters in plutonic lithics: American Mineralogist, v. 100, no. 8-9, p. 1778-1789, doi: 10.2138/am-2015-5135.

Hayes, B., Bédard, J.H., and Lissenberg, C.J., 2014, Olivine slurry replenishment and the development of igneous layering in a Franklin Sill, Victoria Island, Arctic Canada: Journal of Petrology, v. 56, no. 1, p. 83-112, doi: 10.1093/petrology/egu072.

Higgins, M.I.D., 2000, Measurement of crystal size distributions: American Mineralogist, v. 85, p. 1105–1116.

Higgins, M.D., and Roberge, J., 2003, Crystal Size Distribution of Plagioclase and Amphibole from Soufriere Hills Volcano, Montserrat: Evidence for Dynamic Crystallization-Textural Coarsening Cycles: Journal of Petrology, v. 44, p. 1401–1411, doi: 10.1093/petrology/44.8.1401.

Higgins M.D., Roberge J., 2007, Three magmatic components in the 1973 eruption of Eldfell volcano, Iceland: Evidence from plagioclase crystal size distribution (CSD) and geochemistry: Journal of Volcanology and Geothermal Research, v. 161, no. 3, p. 247-260.

Hildreth, W., 2004, Volcanological perspectives on Long Valley, Mammoth Mountain, and Mono Craters: Several contiguous but discrete systems: Journal of Volcanology and Geothermal Research, v. 136, p. 169–198, doi: 10.1016/j.jvolgeores.2004.05.019.

Hildreth, W. and Wilson, C., 2007, Compositional zoning of the Bishop Tuff: Journal of Petrology, v. 48, no. 5, p. 951-999, doi: 10.1093/petrology/egm007.

Hoffman, M. and Michelfelder, G., 2016, Oxygen Isotope and Geochemical analysis of volcanic rocks from south-central New Mexico: Insight on crustal contamination and magmatic evolution: Geological Society of America, Abstracts with Programs, v. 48, no. 7.

Huber, C., Bachmann, O., and Manga, M., 2009, Homogenization processes in silicic magma chambers by stirring and mushification (latent heat buffering): Earth and Planetary Science Letters, v. 283, p. 38–47, doi: 10.1016/j.epsl.2009.03.029.

Huber, C., Bachmann, O., and Manga, M., 2010, Two competing effects of volatiles on heat transfer in crystal-rich magmas: Thermal insulation vs defrosting: Journal of Petrology, v. 51, p. 847–867, doi: 10.1093/petrology/egq003.

Huber, C., Bachmann, O., and Dufek, J., 2012, Crystal-poor versus crystal-rich ignimbrites: A competition between stirring and reactivation: Geology, v. 40, no. 2, p. 115-118, doi: 10.1130/G32425.

Jarvis, K.E., 1988, Inductively coupled plasma mass spectrometry; a new technique for the rapid or ultra-trace level determination of the rare-earth elements in geological materials: Chemical Geology, v. 68, p. 31-39.

Jellinek, A.M., and DePaolo, D.J., 2003, A model for the origin of large silicic magma chambers: precursors of caldera-forming eruptions: Bulletin of Volcanology, v. 65, p. 363-381, doi: 10.1007/s00445-003-0277-y.

Johnson, D.M., Hooper, P.R., and Conrey, R.M., 1999, XRF analysis of rock and minerals for major and trace elements on a single low dilution Li-tetraborate fused bead: Advances in X-ray analysis, v. 41, p. 843-867.

Kay, S., Coira, B., Caffe, P., Chen, C., 2010, Regional chemical diversity, crustal and mantle sources and evolution of central Andean Puna plateau ignimbrites: Journal of Volcanology and Geothermal Research, v. 198, p. 81-111, doi: 10.1016/j.jvolgeores.2010.08.013.

Kern, J.M., de Silva, S., Schmitt, A.K., Kaiser, J.F., Iriarte, R., and Economos, R., 2016, Geochronological imaging of an episodically constructed subvolcanic batholith: U-Pb in zircon chronochemistry of the Altiplano-Puna Volcanic Complex of the Central Andes: Geosphere, v. 12, no. 4.

Klemetti E.W. and Clynne M.A., 2014, Localized Rejuvenation of a Crystal Mush Recorded in Zircon Temporal and Compositional Variation at the Lassen Volcanic Center, Northern California. PLoS ONE, v. 9:, no. 2, doi: 10.1371/journal.pone.0113157

Le Maitre, R.W., Streckeisen, A., Zanettin, B., Le Bas, M.J., Bonin, B., Bateman, P., Bellieni, G., Dudek, A., Efremova, S., Keller, J., Lamere, J., Sabine, P.A., Schmid, R., Sorensen, H., and Woolley, A.R., 2002, Igneous Rocks: A Classification and Glossary of Terms, Recommendations of the International Union of Geological Sciences, Subcommission of the Systematics of Igneous Rocks: Cambridge University Press, ISBN 0-521-66215-X.

Leeman, W.P. and Phelps, D.W., 1981, Partitioning of rare earths and other trace elements between sanidine and coexisting volcanic glass: Journal of Geophysical Research v. 86, doi: 10.1029/JB080i011p10193.

Lipman, P.W., 1967, Mineral and chemical variations within an ash-flow sheet from Aso caldera, southwestern Japan: Contributions to Mineralogy and Petrology, v. 16, no. 4, p. 300-327.

Lipman, P.W., 2007, Incremental assembly and prolonged consolidation of Cordilleran magma chambers: evidence from the Southern Rocky Mountain volcanic field: Geosphere, v. 3, no. 1, p. 42-70.

Lipman, P.W. and Bachmann, O., 2015, Ignimbrites to batholiths: Integrating perspectives from geological, geophysical, and geochronological data: Geosphere, v. 11, no. 3, p. 705-743, doi: 10.1130/GES01091.1.

Mack, G.H., 2004, Middle and Late Cenozoic crustal extension, sedimentation, and volcanism in the southern Rio Grande rift, Basin and Range, and southern Transition Zone of southwestern New Mexico, *in* Mack, G.H., and Giles, K.A., eds., The Geology of New Mexico: A Geologic History: New Mexico Geologic Society, p. 389-406.

Mahood, G.A. and Hildreth, E.W.,1983, Large partition coefficients for trace elements in high-silica rhyolites: Geochimica et Cosmochimica Acta, v. 47, p. 11-30, doi: 10.1016/0016-7037(83)90087-X.

Marsh, B.D., 1988, Crystal size distribution (CSD) in rocks and the kinetics and dynamics of crystallization. Contributions to Mineralogy and Petrology, v. 99, no. 3, p. 277-291, doi:10.1007/BF0037536.

McIntosh, W.C., Sutter, J.F., Chapin, C.E., and Kedzie, L.L., 1990, High-precision $^{40}Ar/^{39}Ar$ sanidine geochronology of ignimbrites in the Mogollon-Datil volcanic field, southwestern New Mexico: Bulletin of Volcanology, v. 52, no. 8, p. 584-601, doi: 10.1007/BF00301210.

McIntosh, W.C., Chapin, C.E., Ratté, J.C., and Sutter, J.F., 1992, Time-stratigraphic framework for the Eocene-Oligocene Mogollon-Datil volcanic field, southwest New Mexico: GSA Bulletin, v. 104, p. 851-871.

McLemore, V., 1994, Volcanic-epithermal deposits in the Mogollon-Datil volcanic field, west-central New Mexico, *in* Mogollon Slope (West-Central New Mexico and East-Central Arizona), Chamberlin, R. M.; Kues, B. S.; Cather, S. M.; Barker, J. M.; McIntosh, W. C.; [eds.], New Mexico Geological Society 45th Annual Fall Field Conference Guidebook, p. 299-309.

McMillan, N.J., 2004, Magmatic record of Laramide subduction and the transition to Tertiary extension: Upper Cretaceous through Eocene igneous rocks of New Mexico *in* The geology of New Mexico: a geologic history: New Mexico Geological Society, Special Edition, v. 11, p. 249-270.

McMillan, N.J., Dickin, A.P., and Haag, D., 2000, Evolution of magma source regions in the Rio Grande rift, southern New Mexico: Geological Society of America Bulletin, v. 112, no. 10, p. 1582-1593.

Michelfelder, G.S. and McMillan, N.J., 2012, Geochemistry, origin, and U-Pb zircon ages of the Sierra Cuchillo Laccolith, Sierra County, New Mexico, *in* Lucas, S.G., McLemore, V.T., Lueth, V.W., Spielmann, J.A., and Krainer, K., eds., Geology of

the Warm Springs Region: New Mexico Geological Society, 63rd Annual Field Conference, Guidebook, p. 249-260.

Michelfelder, G.S., Feeley, T.C., Wilder, A.D., and Klemetti, E.W., 2013, Modification of the continental crust by subduction zone magmatism and *vice-versa*: Across-strike geochemical variations of silicic lavas from individual eruptive centers in the Andean central volcanic zone: Geosciences, v. 3, p. 633-667, doi: 10.3390/geosciences3040633.

Morgan, D.J., and Jerram, D.A., 2006, On estimating crystal shape for crystal size distribution analysis: Journal of Volcanology and Geothermal Research, v. 154, p. 1–7, doi: 10.1016/j.jvolgeores.2005.09.016.

Pistone M., Blundy J., and Brooker R.A., 2017, Water transfer during magma mixing events: Insights into crystal mush rejuvenation and melt extraction processes: American Mineralogist, v. 102, p. 766-776.

Putirka, K., 2008, Thermometers and Barometers for Volcanic Systems. In: Putirka, K., Tepley, F. (Eds.), Minerals, Inclusions and Volcanic Processes, Reviews in Mineralogy and Geochemistry, Mineralogical Society of America, v. 69, p. 61-120.

Ramos, F., 1992, Isotope geology of the metamorphic core of the Central Grouse Creek Mountains, Box Elder County, Utah: Thesis for Masters of Science, The University of California-Las Angeles, 223 pages.

Ratté, J.C., 1981, Geologic map of the Mogollon quadrangle, Catron County, New Mexico: U.S. Geological Survey Geologic Quadrangle Map GQ-1557, scale 1:24 000, 1 sheet.

Ratté, J.C., Marvin, R.F., and Naeser, C.W., 1984, Calderas and ash flow tuffs of the Mogollon Mountains, southwestern New Mexico: Journal of Geophysical Research, v. 89, no. B10,
p. 8713-8732, doi: 10.1029/JB089iB10p08713.

Ratté, J.C., Gaskill, D.L., Eaton, G.P., Peterson, D.L., Stotelmeyer, R.B., and Meeves, H.C., 1979, Mineral Resources of the Gila Primitive Area and Gila Wilderness, New Mexico: Geological Survey Bulletin 1451, 229 p.

Ratté, J.C., McIntosh, W.C., and Bove, D., 1994, Geologic map of the Milligan Mountain quadrangle, Catron County, New Mexico: U.S. Geological Survey, scale 1: 24,000.

Rentz S., 2017, Geochronology of calc-alkaline ash flow tuff units in the Mogollon-Datil volcanic field, southern New Mexico, U-Pb in zircon. Thesis, Missouri State University

Rentz, S., Michelfelder, G.S., and Salings, E., 2016, The Cooney Tuff: ash fall in a calk-alkaline subduction related volcanic field, southern New Mexico: Geological Society of America, Abstracts with Programs, v. 48, no. 7, doi: 10.1130/abs/2016AM-281935.

Rosi, M., Vezzoli, L., Castelmenzano, A., Grieco, G., 1999, Plinian pumice fall deposit of the Campanian Ignimbrite eruption (Phlegraean Fields, Italy): Journal of Volcanology and Geothermal Research, v. 91, p. 179-198.

Rudnick, R.L. and Fountain, D.M., 1995, Nature and composition of the continental crust: a lower crustal perspective: Reviews in Geophysics, v. 33, p. 267-309.

Salisbury, M.J., Bohrson, W.A., Clynne, M.A., Ramos, F.C., and Hoskin, P., 2008, Multiple plagioclase crystal populations identified by crystal size distribution and in situ chemical data: Implications for timescales of magma chamber processes associated with the 1915 eruption of Lassen Peak, CA: Journal of Petrology, v. 49, p. 1755–1780, doi: 10.1093/petrology/egn045.

Seager, W. R., 2004, Laramide (Late Cretaceous–Eocene) tectonics of southwestern New Mexico, *in* Mack, G.H., and Giles, K.A., eds., The Geology of New Mexico: A Geologic History: New Mexico Geologic Society Special Publication, v. 11, p. 183-202.

Schleicher, J.M., Bergantz, G.W., Breidenthal, R.E., and Burgisser, A., 2016, Time scales of crystal mixing in magma mushes: Geophysical Research Letters, v. 43, p. 1543–1550, doi: 10.1002/2015GL067372.

Schnetzler, C.C. and Philpotts, J.A., 1970, Partition coefficients of rare-earth elements between igneous matrix material and rock-forming mineral phenocrysts; II: Geochimica et Cosmochimica Acta, v. 34, no. 3, p. 331-340, doi: 10.1016/0016-7037(70)90110-9.

Shea, T., Larsen, J.F., Gurioli, L., Hammer, J.E., Houghton, B.F., and Cioni, R., 2009, Leucite crystals: Surviving witnesses of magmatic processes preceding the 79AD eruption at Vesuvius, Italy: Earth and Planetary Science Letters, v. 281, p. 88–98, doi: 10.1016/j.epsl.2009.02.014.

Smith, R.L., 1979, Ash-flow magmatism: GSA Special Papers, v. 180, p. 5-28, doi: 10.1130/SPE180-p5.

Taylor, S.R. and McLennan, S.M., 1985, The continental crust: its composition and evolution: Oxford: Blackwell.

Újvári, G., Varga, A., Ramos, F.C., Kovács, J., Németh, T., and Stevens, T., 2012, Evaluating the use of clay mineralogy, Sr-Nd isotopes and zircon U-Pb ages in

tracking dust provenance: An example from loess of the Carpathian Basin: Chemical Geology, v. 304-305, p. 83-96.

Wasson, J.T., 1985, Meteorites: their record of early solar-system history: W.H. Freeman and Co., New York, NY.

Wedepohl, K.H., 1995, The composition of the continental crust: Geochimica et Cosmochimica Acta, v. 59, p. 1217-1232.

Willcock, M.A.W., Bargossi, G.M., Weinberg, R.F., Gasparotto, G., Cas, R.A.F., Giordano, G., and Marocchi, M., 2015, A complex magma reservoir system for a large volume intra- to extra-caldera ignimbrite: Mineralogical and chemical architecture of the VEI8, Permian Ora ignimbrite (Italy): Journal of Volcanology and Geothermal Research, v. 306, p. 17-40, doi: http://dx.doi.org/10.1016/j.jvolgeores.2015.09.015.

Wolff, J.A., Wörner, G., and Blake, S., 1990, Gradients in physical parameters in zoned felsic magma bodies: implications for evolution and eruptive withdrawal: Journal of Volcanology and Geothermal Research, v. 43, no. 1-4, p. 37-55.

Wolff, J.A., Brunstad, K.A., Gardner, J.N., 2011. Reconstruction of the most recent volcanic eruptions from the Valles caldera, New Mexico: Journal of Volcanology and Geothermal Research, v. 199, p. 53–68.

Wolff, J.A., and Ramos, F.C., 2014, Processes in caldera-forming high-silica rhyolite magma: Rb-Sr and pb isotope systematics of the otowi member of the bandeliertuff,valles caldera, new Mexico, USA: Journal of Petrology, v. 55, p. 345–375, doi: 10.1093/petrology/egt070.

Wolff, J., Ellis, B., Ramos, F.C., Starkel, W.A., Boroughs, S., Olin, P.H., Bachmann, O., 2015, Remelting of cumulates as a process for producing chemical zoning in silicic tuffs: A comparison of cool, wet and hot, dry rhyolitic magma systems: Lithos, v. 236-237, p. 275-286.

Wotzlaw, J.-F., Schaltegger, U., Frick, D.A., Dungan, M.A., Gerdes, A.G., and Gunther, D., 2013, Tracking the evolution of large-volume silicic magma reservoirs from assembly to supereruption: Geology, v. 41, p. 867–870, doi: 10.1130/G34366.1.

Yund, R., 1984, Alkali Feldspar exsolution: Kinetics and dependence on alkali interdiffusion, in Brown, W. L., editor, Feldspars and feldspathoids: Structure, Properties, and Occurrences: Dordrecht, D. Reidel Publishing Company, NATO Advanced Science Institute Series C, v. 137, p. 281–315.

Zimmerer, M.J. and McIntosh, W.C., 2013, Geochronologic evidence of upper-crustal in situ differentiation: silicic magmatism at the Organ caldera complex, New Mexico: Geosphere, v. 9, no. 1, p. 155-169, doi: 10.1130/GES00841.1.

APPENDICES: SUPPLEMENTARY DATA FOR MINERAL CHEMISTRY

Appendix A

Mineral data from 12RE5b and 12RE5a feldspars.

No.	Al_2O_3	SiO_2	Na_2O	SrO	CaO	PbO	FeO	BaO	K_2O	TiO_2	Total	Comment
1	16.931	65.72	0.965	0.251	-0.006	0.045	1.837	0.069	14.448	0.009	100.269	Astimex Or 1
2	16.591	64.732	1.031	0.2	0.011	-0.006	1.74	0.095	15.545	0.018	99.957	Astimex Or 2
3	16.69	65.213	0.97	0.23	0.008	-0.021	1.735	0.052	15.526	0.022	100.425	Astimex Or 3
4	16.644	64.135	0.969	0.219	-0.019	-0.025	1.692	0.116	15.661	-0.007	99.385	Astimex Or 4
5	16.829	62.568	8.644	0.193	0.273	0.005	0.303	-0.037	3.627	0.032	92.437	12RE5b 1-2
6	18.851	67.534	5.733	0.211	0.184	0.047	0.22	-0.017	8.591	0.002	101.356	12RE5b 1-1
7	18.873	67.665	5.763	0.181	0.174	-0.029	0.25	0.017	8.488	0.025	101.407	12RE5b 1-3
8	19.451	66.166	7.428	0.239	0.609	-0.038	0.265	0.05	6.207	0.013	100.39	12RE5b 2 Line 001
9	19.4	65.376	6.607	0.203	0.697	-0.016	0.255	0.069	6.955	0.021	99.567	12RE5b 2 Line 002
10	19.926	66.533	8.574	0.211	1.034	-0.047	0.255	0.067	3.988	0.023	100.564	12RE5b 2 Line 003
11	19.008	66.553	5.294	0.222	0.261	0.021	0.265	0.037	9.259	0.019	100.939	12RE5b 2 Line 004
12	18.866	66.279	5.582	0.225	0.265	-0.062	0.231	0.041	8.96	0.01	100.397	12RE5b 2 Line 005
13	18.852	66.951	6.014	0.203	0.218	0.007	0.252	-0.072	8.209	-0.005	100.629	12RE5b 3-1
14	18.74	66.634	5.833	0.173	0.229	-0.048	0.216	0.007	8.597	0.008	100.389	12RE5b 3-2
15	18.895	66.658	5.99	0.218	0.255	0	0.23	0.028	8.312	0.027	100.613	12RE5b 3-3
16	19.014	66.531	6.863	0.217	0.355	-0.079	0.196	-0.002	6.619	0.002	99.716	12RE5b 4 Line 001
17	19.671	66.861	8.189	0.215	0.792	-0.027	0.258	0.006	4.505	0.023	100.493	12RE5b 4 Line 002
18	6.058	21.102	1.971	0.108	0.865	-0.004	0.149	-0.043	0.464	0.051	30.721	12RE5b 4 Line 003

Appendix A continued

No.	Al_2O_3	SiO_2	Na_2O	SrO	CaO	PbO	FeO	BaO	K_2O	TiO_2	Total	Comment
19	19.36	66.19	6.938	0.199	0.681	0.008	0.228	0.032	6.536	0.037	100.209	12RE5b 4 Line 004
20	19.167	65.369	6.01	0.243	0.535	-0.016	0.255	0.087	7.734	0.018	99.402	12RE5b 4 Line 005
21	19.059	66.067	6.399	0.234	0.498	0.02	0.242	0.091	7.407	0.008	100.025	12RE5b 4 Line 006
22	18.342	63.252	6.115	0.216	0.474	0.009	0.199	0.063	6.631	0.006	95.307	12RE5b 4 Line 007
23	19.237	66.46	6.939	0.213	0.478	-0.007	0.258	0.022	6.906	0.014	100.52	12RE5b 4 Line 008
24	27.474	55.756	6.234	0.389	8.873	0.006	0.318	0.095	0.368	0	99.513	12RE5b 5-1
25	19.882	66.064	8.415	0.227	1.008	0.014	0.275	0.035	4.373	0.025	100.318	12RE5b 5-2
26	19.198	65.272	6.512	0.218	0.466	0.065	0.205	0.044	7.207	0.009	99.196	12RE5b 5-3
27	0.065	96.634	-0.005	0.275	0.011	-0.013	0.052	0.084	0.005	0.045	97.153	12RE5b 5.2-2
28	19.356	65.956	7.105	0.215	0.57	-0.001	0.242	0.037	6.28	0.02	99.78	12RE5b 5.2-1
29	19.074	66.039	6.337	0.235	0.521	0.029	0.297	0.052	7.572	0.014	100.17	12RE5b 5.4
30	18.734	66.677	5.729	0.21	0.198	0.016	0.303	-0.059	8.565	0.013	100.386	12RE5b 5.3
31	19.171	66.396	6.937	0.215	0.487	-0.067	0.254	0.039	6.843	0.012	100.287	12RE5b 6.1
32	19.972	66.769	9.123	0.22	1.008	0.046	0.227	0.052	3.084	0.029	100.53	12RE5b 6.2
33	19.137	65.705	6.32	0.204	0.358	0.048	0.283	0.102	7.621	0.001	99.779	12RE5b 6.3
34	18.836	65.922	5.593	0.192	0.197	-0.03	0.209	-0.056	8.59	0.026	99.479	12RE5b 7
35	18.954	65.671	5.909	0.209	0.156	-0.056	0.228	-0.009	8.218	0.02	99.3	12RE5b 8
36	19.369	65.055	7.69	0.257	0.471	-0.018	0.219	0.118	5.762	0.04	98.963	12RE5b 9
37	18.956	64.521	6.125	0.219	0.271	-0.002	0.254	0.026	8.201	0.004	98.575	12RE5b 10.1
38	19.353	64.722	6.922	0.212	0.426	0.004	0.218	0.046	6.559	0.017	98.479	12RE5b 10.2
39	19.254	63.285	6.394	0.239	0.476	0.005	0.204	-0.006	7.467	0.023	97.341	12RE5b 11

Appendix A continued

No.	Al_2O_3	SiO_2	Na_2O	SrO	CaO	PbO	FeO	BaO	K_2O	TiO_2	Total	Comment
40	18.88	65.195	5.827	0.243	0.191	-0.005	0.26	-0.037	8.726	-0.006	99.274	12RE5b 12
41	19.836	63.988	7.283	0.216	0.944	-0.027	0.248	0.054	5.969	0.034	98.545	12RE5b 13
42	18.458	65.194	5.383	0.195	0.124	0.055	0.366	-0.048	8.883	0.007	98.617	12RE5b 14
43	18.315	65.551	5.232	0.205	0.078	0	0.337	-0.015	8.883	0.033	98.619	12RE5b 14.2
44	0.756	95.947	0.236	0.319	0.011	0.03	0.031	-0.061	0.103	0.077	97.449	12RE5b 14.3
45	0.302	94.347	0.134	0.285	0.049	0.023	0.021	-0.007	0.034	0.058	95.246	12RE5b 14.4
46	19.301	64.846	7.051	0.199	0.433	-0.002	0.219	0.076	6.746	0.005	98.874	12RE5b 15-1
47	18.887	65.121	5.861	0.176	0.24	0.022	0.271	0.03	8.457	-0.002	99.063	12RE5b 15-2
48	19.355	64.671	7.456	0.225	0.548	-0.07	0.287	0.092	5.942	0.003	98.509	12RE5b 16
49	18.904	64.861	5.883	0.213	0.215	-0.005	0.188	-0.002	8.322	0.004	98.583	12RE5b 17
50	19.133	64.649	6.168	0.202	0.259	0.02	0.249	-0.057	8.085	0.005	98.713	12RE5b 17-2
51	19.025	65.03	6.157	0.238	0.213	0.021	0.266	0.059	7.95	0.021	98.98	12RE5b 18
52	19.361	63.884	6.955	0.197	0.427	0.033	0.232	0.142	6.937	0.003	98.171	12RE5b 19 Line 001
53	19.474	64.232	7.475	0.244	0.617	0.013	0.224	0.102	5.926	0.014	98.321	12RE5b 19 Line 002
54	20.098	64.043	9.433	0.252	1.148	0.009	0.231	0.05	2.573	-0.001	97.836	12RE5b 19 Line 003
55	19.524	63.945	6.856	0.238	0.66	0.025	0.203	0.146	6.537	0.035	98.169	12RE5b 20
56	19.6	64.271	7.95	0.214	0.803	-0.008	0.233	0.058	5.81	0.005	98.936	12RE5b 20-2
57	19.181	63.483	6.502	0.209	0.415	0.009	0.267	0.074	7.356	0.024	97.52	12RE5b 21
58	18.874	64.818	5.742	0.21	0.22	-0.006	0.254	-0.035	8.768	0.013	98.858	12RE5b 22
59	18.954	64.158	5.872	0.228	0.25	-0.006	0.261	-0.07	8.286	0.008	97.941	12RE5b 23
60	18.902	63.28	5.842	0.179	0.166	-0.058	0.25	0.063	8.62	0.005	97.249	12RE5b 24

Appendix A continued

No.	Al_2O_3	SiO_2	Na_2O	SrO	CaO	PbO	FeO	BaO	K_2O	TiO_2	Total	Comment
61	-0.005	95.797	0.014	0.264	-0.007	0.006	0.012	0.026	0.013	0.035	96.155	12RE5a 2
62	18.91	66.646	6.239	0.2	0.205	-0.056	0.219	-0.002	8.026	0.003	100.39	12RE5a 1
63	18.832	66.656	6.066	0.215	0.191	-0.05	0.213	0.037	8.333	0.015	100.508	12RE5a 1-2
64	18.506	64.568	5.634	0.215	0.167	0.015	0.219	0.07	8.597	-0.014	97.977	12RE5a 3
65	18.748	63.711	5.364	0.203	0.179	-0.007	0.23	-0.004	8.718	0.009	97.151	12RE5a 3-2
66	18.854	64.907	6.068	0.199	0.201	0.039	0.241	0.039	8.303	0.004	98.855	12RE5a 4
67	18.291	65.458	5.733	0.216	0.141	-0.026	0.281	0.013	8.68	0.014	98.801	12RE5a 5-1
68	18.738	66.07	6.217	0.227	0.16	0.025	0.239	0.03	7.981	0.007	99.694	12RE5a 5-2
69	19.039	65.915	6.137	0.222	0.162	-0.035	0.221	-0.011	8.082	0.026	99.758	12RE5a 6
70	19.041	65.635	6.291	0.2	0.195	-0.016	0.251	0.007	7.759	0.012	99.375	12RE5a 7
71	18.934	66.043	6.348	0.227	0.21	0.002	0.225	0.006	7.548	0.004	99.547	12RE5a 8
72	18.874	65.761	6.064	0.213	0.194	-0.002	0.278	-0.039	7.891	0.025	99.259	12RE5a 9
73	19.091	64.979	5.703	0.211	0.188	0.029	0.231	0.018	8.686	0	99.136	12RE5a 10
74	18.866	67.243	5.729	0.203	0.188	0.012	0.243	0.074	8.654	0.014	101.226	12RE5a 11-1
75	18.836	66.459	5.563	0.218	0.204	0.035	0.201	-0.002	8.844	0.004	100.362	12RE5a 11-2
76	-0.044	97.899	-0.002	0.299	0.003	0.035	0.049	-0.046	0.017	0.015	98.225	12RE5a 12
77	18.885	65.581	5.747	0.185	0.188	0.038	0.234	0.009	8.242	0.021	99.13	12RE5a 13
78	18.85	66.062	6.063	0.198	0.177	0.027	0.171	0.054	8.247	0.007	99.856	12RE5a 13-2
79	18.782	64.119	5.777	0.196	0.175	0.04	0.228	0.02	8.598	0.019	97.954	12RE5a 14
80	18.781	64.903	5.875	0.212	0.179	0.035	0.263	0.02	8.288	0.004	98.56	12RE5a 15
81	18.955	63.888	6.157	0.216	0.233	-0.028	0.266	0.072	8.11	0.017	97.886	12RE5a 16 Line 01

Appendix A continued

No.	Al_2O_3	SiO_2	Na_2O	SrO	CaO	PbO	FeO	BaO	K_2O	TiO_2	Total	Comment
82	18.931	64.828	5.808	0.205	0.182	0.023	0.248	-0.022	8.472	0.02	98.695	12RE5a 16 Line 02
83	18.722	64.383	5.895	0.212	0.229	-0.022	0.18	0.002	8.459	-0.001	98.059	12RE5a 16 Line 03
84	18.644	64.532	6.111	0.189	0.195	0.008	0.256	-0.096	8.173	-0.002	98.01	12RE5a 16 Line 04
85	18.814	65.054	5.856	0.201	0.203	-0.022	0.243	0.037	8.393	0.004	98.783	12RE5a 16 Line 05
86	18.883	65.469	6.373	0.194	0.188	0.022	0.232	-0.074	7.778	0.022	99.087	12RE5a 16 Line 06
87	19.018	65.168	6.794	0.222	0.216	0.012	0.181	-0.068	6.957	0.011	98.511	12RE5a 16 Line 07
88	18.844	64.523	5.924	0.189	0.184	0.024	0.243	-0.028	8.364	0.017	98.284	12RE5a 16 Line 08
89	19.064	65.743	5.773	0.208	0.196	0.02	0.259	-0.004	8.476	0.015	99.75	12RE5a 17
90	18.806	64.653	6.138	0.227	0.171	-0.017	0.224	0.009	8.015	0.018	98.244	12RE5a 18
91	18.896	63.954	6.135	0.176	0.176	0.058	0.19	-0.018	8.206	0.02	97.793	12RE5a 19
92	18.808	65.336	5.976	0.217	0.176	0.051	0.258	-0.007	8.482	0.013	99.31	12RE5a 20
93	19.019	67.018	7.119	0.226	0.29	0.021	0.21	0.029	6.462	-0.021	100.373	12RE5a 21
94	18.741	66.487	6.375	0.203	0.185	0.038	0.219	-0.013	7.9	-0.004	100.131	12RE5a 22
95	18.975	66.152	6.356	0.205	0.226	-0.035	0.242	-0.011	8.043	0.025	100.178	12RE5a 23
96	19.167	66.225	6.24	0.216	0.214	0.016	0.252	0.042	7.93	0.004	100.306	12RE5a 24 Line 001
97	18.924	65.705	5.832	0.238	0.194	-0.012	0.238	-0.037	8.086	0.001	99.169	12RE5a 24 Line 002
98	18.787	65.655	5.976	0.194	0.184	-0.014	0.283	-0.013	8.114	0.01	99.176	12RE5a 24 Line 003
99	18.961	65.709	6.697	0.217	0.2	0.001	0.292	0.077	7.387	0.011	99.552	12RE5a 24 Line 004
100	18.834	65.56	6.693	0.197	0.166	0.044	0.234	0.002	7.285	0.018	99.033	12RE5a 24 Line 005
101	16.463	64.08	0.933	0.192	-0.003	-0.023	1.686	0	15.661	0.023	99.012	Astimex Or 3

Appendix A continued

No.	Al_2O_3	SiO_2	Na_2O	SrO	CaO	PbO	FeO	BaO	K_2O	TiO_2	Total	Comment
102	16.61	64.174	0.998	0.194	-0.021	-0.033	1.68	0.043	15.726	-0.025	99.346	Astimex Or 4
Minimum	-0.044	21.102	-0.005	0.108	-0.021	-0.079	0.012	-0.096	0.005	-0.025	30.721	
Maximum	27.474	97.899	9.433	0.389	8.873	0.065	1.837	0.146	15.726	0.077	101.407	
Average	17.902	66.326	5.728	0.217	0.389	0.001	0.319	0.022	7.498	0.014	98.416	
Sigma	4.371	8.206	2.022	0.031	0.884	0.031	0.359	0.05	3.014	0.015	6.902	
No. of data	102											

Appendix B

Mineral data from 180-SP-2 and MO-09 feldspars.

No.	Al_2O_3	SiO_2	Na_2O	SrO	CaO	PbO	FeO	BaO	K_2O	TiO_2	Total	Comment
1	16.183	64.061	0.966	0.196	0.006	0.027	1.707	0.09	15.793	0.003	99.032	Astimex Or 1
2	16.19	63.858	0.963	0.201	-0.011	0.021	1.709	0.101	15.6	0	98.632	Astimex Or 2
3	15.997	63.962	0.979	0.196	-0.009	-0.023	1.67	-0.002	15.619	0.016	98.405	Astimex Or 3
5	18.725	66.516	5.649	0.229	0.166	-0.008	0.201	0.015	8.779	0.001	100.273	180-SP-2 1
6	18.839	64.894	5.581	0.232	0.204	-0.04	0.177	-0.011	8.872	0.028	98.776	180-SP-2 2
7	18.776	65.714	5.491	0.184	0.169	-0.034	0.229	0.045	8.967	0.013	99.554	180-SP-2 3
8	18.791	66.693	5.574	0.221	0.158	-0.028	0.255	0.043	8.894	0.011	100.612	180-SP-2 4
9	18.749	66.529	5.425	0.173	0.183	-0.049	0.225	-0.043	9.057	0.008	100.257	180-SP-2 4-2
10	18.779	64.975	5.631	0.2	0.175	0.028	0.192	0.045	8.834	0.011	98.87	180-SP-2 5 Line 001
11	18.765	65.388	5.563	0.207	0.217	-0.014	0.202	-0.019	8.895	0.007	99.211	180-SP-2 5 Line 002
12	18.805	65.682	5.642	0.192	0.21	-0.056	0.238	0.009	8.862	0.038	99.622	180-SP-2 5 Line 003
13	18.772	65.449	5.567	0.224	0.195	-0.014	0.216	-0.004	8.809	-0.004	99.21	180-SP-2 5 Line 004
14	18.729	66.601	5.647	0.189	0.15	0.052	0.2	0.098	8.642	0.015	100.323	180-SP-2 5 Line 005
15	18.876	65.837	5.693	0.208	0.194	-0.019	0.237	0	8.526	0.008	99.56	180-SP-2 6
16	18.303	65.082	4.145	0.169	0.057	-0.032	0.173	0.058	10.882	-0.006	98.831	180-SP-2 7 Line 001
17	18.884	66.347	6.498	0.199	0.153	-0.033	0.263	0.032	7.869	0.01	100.222	180-SP-2 7 Line 002
18	18.716	65.845	5.738	0.205	0.152	0.009	0.225	0.009	8.834	0.031	99.764	180-SP-2 7 Line 003
19	18.671	66.032	5.451	0.209	0.134	0.005	0.188	-0.007	8.876	-0.003	99.556	180-SP-2 7 Line 004
20	0.445	94.943	0.165	0.31	0.015	-0.02	0.025	-0.013	0.14	0.012	96.022	180-SP-2 7 Line 005
21	18.805	63.476	5.607	0.2	0.169	-0.028	0.202	-0.013	8.87	0	97.288	180-SP-2 8

Appendix B continued

No.	Al_2O_3	SiO_2	Na_2O	SrO	CaO	PbO	FeO	BaO	K_2O	TiO_2	Total	Comment
22	18.879	66.759	5.462	0.221	0.202	0.045	0.248	0.052	8.928	0.016	100.812	180-SP-2 9
23	18.755	66.197	5.692	0.211	0.203	-0.006	0.218	0.017	8.843	-0.009	100.121	180-SP-2 10
24	18.912	66.755	6.083	0.187	0.176	-0.078	0.201	0.067	8.508	0.023	100.834	180-SP-2 10-2
25	18.651	66.389	5.52	0.219	0.179	0.024	0.252	0.015	9.003	0	100.252	180-SP-2 10-3
26	18.911	65.661	5.709	0.213	0.218	-0.026	0.217	-0.043	8.777	0.012	99.649	180-SP-2 11
27	18.692	62.31	5.697	0.196	0.189	0.018	0.256	0.036	8.81	0.004	96.208	180-SP-2 12
28	18.295	60.077	5.293	0.204	0.209	0.034	0.272	-0.062	8.796	-0.006	93.112	180-SP-2 13
29	18.58	66.403	5.671	0.22	0.169	0.006	0.212	0.007	8.786	0.022	100.076	180-SP-2 14
30	18.236	65.459	5.394	0.196	0.207	0.009	0.237	-0.017	8.708	0.007	98.436	180-SP-2 15
31	13.009	71.117	3.794	0.259	0.517	0.031	0.413	0.144	5.494	0.251	95.029	180-SP-2 16
32	18.768	66.095	5.557	0.195	0.177	-0.018	0.216	-0.08	8.856	0.007	99.773	180-SP-2 15-2
33	17.493	66.962	4.905	0.193	0.14	-0.007	0.533	0.056	8.679	0.022	98.976	180-SP-2 17 Line 01
34	18.339	66.012	5.376	0.215	0.18	-0.002	0.235	-0.069	9.037	0.01	99.333	180-SP-2 17 Line 02
35	18.493	66.381	5.826	0.226	0.186	0.04	0.25	0.05	8.525	0.028	100.005	180-SP-2 17 Line 03
36	15.82	56.645	4.587	0.205	0.178	-0.028	0.154	-0.004	7.717	0.007	85.281	180-SP-2 17 Line 04
37	18.531	66.027	5.701	0.219	0.151	-0.011	0.233	0.086	8.575	0.012	99.524	180-SP-2 17 Line 05
38	18.939	66.129	5.618	0.211	0.143	-0.009	0.23	-0.013	8.999	0.015	100.262	180-SP-2 18
39	18.243	62.312	11.259	0.366	0.464	0.021	0.051	-0.009	1.212	0	93.919	MO-09 A1
40	19.785	68.85	11.416	0.37	0.139	0.034	0.02	-0.035	0.087	-0.008	100.658	MO-09 1
41	19.848	68.079	11.781	0.384	0.204	-0.02	0.016	0.002	0.042	-0.012	100.324	MO-09 a2
42	28.488	49.589	1.155	0.147	0.419	-0.03	1.104	0.065	7.57	0.053	88.56	MO-09 a2-1

Appendix B continued

No.	Al_2O_3	SiO_2	Na_2O	SrO	CaO	PbO	FeO	BaO	K_2O	TiO_2	Total	Comment
43	19.864	69.077	11.559	0.257	0.276	-0.005	0.022	0.004	0.242	0.005	101.301	MO-09 a3
44	19.807	68.289	11.72	0.394	0.209	0.007	0.006	-0.024	0.083	-0.006	100.485	MO-09 a4
45	19.433	69.6	11.837	0.193	0.094	-0.016	-0.011	0.009	0.086	-0.004	101.221	MO-09 a5
46	19.506	67.956	11.883	0.371	0.208	-0.044	-0.019	-0.004	0.058	0.002	99.917	MO-09 a6
47	19.586	67.603	12.432	0.375	0.207	-0.014	0.061	0.063	0.171	-0.017	100.467	MO-09 a7
48	19.31	70.066	11.896	0.255	0.068	-0.02	0.009	-0.041	0.05	0.023	101.616	MO-09 a8
49	19.766	69.525	11.974	0.273	0.11	-0.032	-0.01	0.022	0.087	-0.01	101.705	MO-09 a9
50	20.053	68.185	11.391	0.384	0.405	-0.036	0.011	0.02	0.087	0.002	100.502	MO-09 a9.1
51	19.843	68.132	12.054	0.227	0.163	0.036	0.014	0.037	0.037	-0.002	100.541	MO-09 a10
52	19.821	71.452	8.683	0.213	0.371	-0.006	0.011	0.024	0.035	-0.007	100.597	MO-09 a11
53	19.835	69.596	11.805	0.399	0.197	0.011	0.04	0.048	0.075	-0.004	102.002	MO-09 a12
54	16.512	64.271	0.978	0.195	-0.004	-0.044	1.637	0.075	15.626	0.013	99.259	Astimex Or 1
55	16.486	64.058	0.951	0.195	0.005	-0.002	1.737	0.043	15.663	0.025	99.161	Astimex Or 2
Minimum	0.445	49.589	0.165	0.147	-0.011	-0.078	-0.019	-0.08	0.035	-0.017	85.281	
Maximum	28.488	94.943	12.432	0.399	0.517	0.052	1.737	0.144	15.793	0.251	102.002	
Average	18.376	66.406	6.456	0.236	0.179	-0.007	0.326	0.018	6.961	0.012	98.962	
Sigma	3.104	5.205	3.45	0.066	0.107	0.028	0.472	0.045	4.741	0.036	2.978	

Appendix C

Mineral data from 12RE5a and 12RE5b hornblendes.

No.	SiO_2	Al_2O_3	Na_2O	MgO	CaO	Cr_2O_3	FeO	MnO	K_2O	TiO_2	Total	Comment
1	40.021	14.741	2.663	13.085	10.297	0.034	10.057	0.095	2.043	4.784	97.82	UI #1 KHbl 1
2	40.09	14.977	2.82	13.235	10.13	0.008	10.353	0.091	2.057	4.712	98.473	UI #1 KHbl 2
4	41.941	15.107	2.223	14.937	11.798	0	10.966	0.116	0.188	1.439	98.715	UI #1 AHbl 1
5	41.728	14.91	2.279	15.15	11.7	0	11.211	0.136	0.192	1.433	98.739	UI #1 AHbl 2
7	28.133	1.354	0.109	0.125	24.431	0	3.116	0.426	0.007	32.768	90.469	12RE5a H4
8	26.18	6.727	2.228	0.142	0.999	0.001	0.186	0.04	3.978	0.072	40.553	12RE5a H1-1
9	15.234	1.636	1.207	0.063	0.857	0	0.13	0	3.265	0.01	22.402	12RE5a H1-2
10	28.081	1.477	0.062	0.194	24.345	0	3.82	0.482	0.002	31.106	89.569	12RE5a H2
11	43.284	11.106	0.676	21.884	0.07	0.006	3.678	2.103	9.218	1.75	93.775	12RE5a H3
12	49.988	5.083	2.259	16.895	10.561	0	10.751	1.208	0.647	1.164	98.556	12RE5b H1
13	32.493	0.268	0.068	0.515	0.164	0	27.291	5.69	0.002	34.286	100.777	12RE5b H3
14	38.505	11.378	0.525	19.048	0.04	0	14.351	1.146	8.806	2.401	96.2	12RE5b H2
15	43.755	7.481	3.451	15.142	10.746	0.012	13.097	1.383	0.813	1.567	97.447	12RE5b H4
Minimum	15.234	0.268	0.062	0.063	0.04	0	0.13	0	0.002	0.01	22.402	
Maximum	49.988	15.107	3.451	21.884	24.431	0.034	27.291	5.69	9.218	34.286	100.777	
Average	36.11	8.173	1.582	10.032	8.934	0.005	9.154	0.994	2.401	9.038	86.423	
Sigma	9.489	5.848	1.184	8.404	8.493	0.01	7.306	1.558	3.209	13.592	24.885	
No. of data	13											

Appendix D

Mineral data from 180-SP-2 and MO-09 hornblendes.

No.	SiO_2	Al_2O_3	Na_2O	MgO	CaO	Cr_2O_3	FeO	MnO	K_2O	TiO_2	Total	Comment
1	40.931	14.897	2.65	13.13	10.45	0.011	10.696	0.108	2.046	4.751	99.67	UI #1 KHbl 1
2	40.487	15.004	2.763	13.06	10.446	0	10.592	0.058	2.071	4.794	99.275	UI #1 KHbl 2
3	40.49	14.848	2.66	13.119	10.515	0	10.449	0.112	2.046	4.705	98.944	UI #1 KHbl 3
4	40.941	14.94	2.171	14.663	11.469	0.007	10.476	0.142	0.195	1.299	96.303	UI #1 AHbl 1
5	40.821	14.665	2.16	14.713	11.388	0.004	10.286	0.154	0.189	1.33	95.71	UI #1 AHbl 2
6	41.058	14.744	2.339	14.808	11.383	0.042	10.47	0.119	0.186	1.34	96.489	UI #1 AHbl 3
7	42.166	13.398	2.63	14.881	11.3	0.001	11.003	0.125	0.541	2.245	98.29	180-SP-2 H1
8	40.354	11.637	0.555	18.204	0.021	0	12.287	0.889	9.326	2.319	95.592	180-SP-2 H2
9	50.602	3.893	0.404	15.595	20.721	0.06	8.008	0.212	0.008	0.722	100.225	180-SP-2 H3
10	42.186	13.613	2.663	15.299	11.661	0.016	10.351	0.1	0.492	2.074	98.455	180-SP-2 H4
11	42.214	12.13	2.734	14.788	11.593	0.021	10.901	0.17	0.651	3.501	98.703	180-SP-2 H5
12	40.087	11.334	0.736	18.152	0.034	0.012	11.319	0.848	9.149	2.188	93.859	180-SP-2 H6
13	30.478	10.774	0.544	12.617	0.039	0	11.352	0.477	7.363	4.2	77.844	MO-09 h1
14	36.176	14.281	0.778	15.789	0	0.014	13.157	0.271	8.506	4.6	93.572	MO-09 h2
15	37.573	13.26	0.71	15.752	0.013	0	13.704	0.563	8.972	4.82	95.367	MO-09 h3
16	37.891	13.52	0.619	16.047	0.004	0	14.028	0.594	8.813	4.782	96.298	MO-09 h4
17	43.168	21.057	0.347	8.288	0.122	0	7.783	0.236	9.02	2.113	92.134	MO-09 h5
18	36.941	13.462	0.723	15.499	0.044	0.011	13.538	0.568	8.768	4.776	94.33	MO-09 h6
19	37.523	13.57	0.689	15.827	0.002	0	13.883	0.47	9.051	4.981	95.996	MO-09 h7
20	41.043	14.848	2.749	13.141	10.323	0	10.777	0.081	2.081	4.8	99.843	UI #1 KHbl 1

Appendix D continued

No.	SiO_2	Al_2O_3	Na_2O	MgO	CaO	Cr_2O_3	FeO	MnO	K_2O	TiO_2	Total	Comment
21	40.473	14.588	2.705	12.975	10.488	0	10.669	0.073	1.979	4.757	98.707	UI #1 KHbl 2
22	40.665	14.726	2.689	13.065	10.448	0.02	10.528	0.084	2.041	4.706	98.972	UI #1 KHbl 3
23	40.832	14.722	2.14	14.54	11.58	0.021	10.419	0.142	0.192	1.349	95.937	UI #1 AHbl 1
24	41.198	14.945	2.204	14.6	11.405	0.008	10.646	0.113	0.192	1.354	96.665	UI #1 AHbl 2
25	41.074	14.849	2.211	14.661	11.453	0.009	10.718	0.127	0.187	1.337	96.626	UI #1 AHbl 3
Minimum	30.478	3.893	0.347	8.288	0	0	7.783	0.058	0.008	0.722	77.844	
Maximum	50.602	21.057	2.763	18.204	20.721	0.06	14.028	0.889	9.326	4.981	100.225	
Average	40.295	13.748	1.743	14.529	7.476	0.01	11.122	0.273	3.763	3.194	96.152	
Sigma	3.385	2.791	0.968	1.957	6.024	0.015	1.577	0.247	3.915	1.587	4.375	
No. of data	25											